II Advanced Materials R&D

II.1 Next Generation Lithium-Ion Batteries: Advanced Anodes R&D

II.1.B Silicon Electrolyte Interface Stabilization (SEISta) (NREL, ANL, ORNL, LBNL, SNL)

Anthony Burrell
National Renewable Energy Laboratory
15013 Denver West Parkway
Golden, CO, 80401
E-mail: anthony.burrell@nrel.gov

Brian Cunningham, Battery R&D Technology Manager
U.S. Department of Energy
E-mail: brian.cunningham@ee.doe.gov

Table of Contents

Project Introduction

This report documents the Silicon Electrolyte Interface Stabilization (SEISta) team's approach in (1) characterizing the early-stage silicon solid-electrolyte interphase (SEI), including progress on identifying the specific reaction pathways present in the formation of the SEI layer, and (2) establishing a procedure for measuring SEI growth rate at fixed potentials and different cycling regimes.

Silicon is a viable alternative to graphitic carbon as an electrode in lithium-ion cells and can theoretically store >3,500 mAh/g. However, lifetime problems have been observed that severely limit its use in practical systems. The major issues appear to involve the stability of the electrolyte and the uncertainty associated with the formation of a stable SEI at the electrode. Recently, calendar-life studies have indicated that the SEI may not be stable even under conditions where the cell is supposedly static. Clearly, a more foundational understanding of the nature of the silicon/electrolyte interface is required if we are to solve these complex stability issues. A new multi-lab consortium has been formed to address a critical barrier in implementing a new class of materials used in lithium-ion batteries that will allow for smaller, cheaper, and better-performing batteries for electric-drive vehicles. This consortium, named the Silicon Electrolyte Interface Stabilization (SEISta) project, was formed to focus on overcoming the barrier to using such anode materials. Five National Laboratories are involved: the National Renewable Energy Laboratory (NREL), Argonne National Laboratory (ANL), Lawrence Berkeley National Laboratory (LBNL), Oak Ridge National Laboratory (ORNL), and Sandia National Laboratories (SNL).

The SEISta project was specifically developed to tackle the foundational understanding of the formation and evolution of the solid-electrolyte interphase on silicon. This project will have as its primary goal an understanding of the reactivity of the silicon and lithiated silicon interface with the electrolyte in lithium-ion systems. It consists of researchers from NREL, ANL, LBNL, ORNL, and SNL working toward clear, unified goals. The Silicon Deep-Dive team, which focuses on the science and technology barriers in functional electrodes, is a critical partner in this work. Many of the researchers are shared between both teams, and we hold joint meetings to ensure effective communication between the teams.

The current goals of SEISta are:

1. Demonstrate ability to make model electrodes of Mg-Si Zintl compounds and compare SEI chemistry to silicon using X-ray photoelectron spectroscopy (XPS), scanning transmission electron microscopy–energy-dispersive X-ray spectroscopy (STEM-EDS), and Fourier-transform infrared spectroscopy (FTIR)/Raman. **Q1 (100% Complete)**

2. Establish experiments and protocols for understanding the factors that affect safety in silicon anodes, with a specific focus on highly exothermic reactions that occur at silicon electrodes. **Q1 (100% Complete)**

3. Determine the effect that CO_2 has on the stability of SEI formation on model electrodes, but examine the changes in the nature of the SEI (XPS, FTIR/Raman, and quantitative electrochemical measurement) as a function of CO_2 concentration. **Q2 (100% Complete)**

4. Determine Zintl phase formation mechanism and its effect on SEI with model systems including Si nanoparticles, Si wafer, amorphous silicon (a-Si) thin film using XPS, atomic force microscopy/scanning spreading resistance microscopy (AFM/SSRM), STEM-EDS, and FTIR/Raman. **Q2 (100% Complete)**

5. Go/No-Go on production of tin-silicon alloys to be determined by the ability of the alloys to be prepared in 1-gram quantities and a demonstration that the alloys exhibit greater cyclic life than the pure metals alone. **Q2 (100% Complete, Decision = GO)**

6. Determine the chemistry and interfacial properties (e.g., nature of the chemical bonding at the surface of Si and the organic material) of lithium polyacrylate (LiPAA)/Si interfaces as a function of charge (open circuit voltage [OCV], 0.8 V, 0.4 V, 0.15 V, 0.05 V) and drying temperature (100°C, 125°C, 150°C, 175°C, 200°C). **Q3 (100% Complete)**

7. Determine how binder changes the stress/strain on silicon electrodes as a function of state of charge by varying Si nanoparticle size and surface functionally using both 2D and 3D model systems. **Q3 (100% Complete)**

8. Implement protocols that enable comparisons of safety responses in silicon anodes as a metric for improving safety in silicon cells. **Q3 (100% Complete)**

9. Publish a document that will enable other research and development groups to analyze stability of the SEI on a silicon-based anode, thus enabling developers or researchers to continually improve silicon cell stability (joint milestone with the Silicon Deep-Dive team). **Q4 (100% Complete)**

10. Understand how the nature and amount of formed/soluble SEI species varies with electrolyte, binder, and Si anode (with surface functionalization) using gas chromatography–mass spectrometry, (in situ) FTIR/Raman, and XPS. **Q4 (100% Complete)**

Approach

The SEISta team works to ensure that protocols for sample preparation, experimental design, and implementation as well as data reporting are consistent across the whole team. Each laboratory is working

toward the same set of quarterly milestones using its own specific talents and capabilities in a concerted effort with the other team members. This joint focus results in multiple researchers interacting to produce and analyze data to ensure that individual experimental variations will not lead to erroneous results. Critical to the success of this effort is the use of standard samples that can be shared by all parties. In addition to weekly whole-team video presentations, we have held on-site face-to-face meetings each quarter for all team members and other interested parties to brainstorm and sort out issues with existing experiments and jointly develop new experimental plans.

Objectives

The critical issues that SEISta is attempting to address are:

- What are the properties of the lithiated silicon/electrolyte interface?
- What is the silicon SEI actually made of and what reactions are contributing to it?
- How fast does the silicon SEI grow?
- Does it stop growing?
- Is it soluble?
- Can it be stabilized?

For fiscal year (FY) 2020, the team continues to focus on three broad tasks:

Materials Standardization—This task is critical to developing and deploying standardized samples and experimental procedures across the team. We will continue to provide full characterization to any new sample that is to be used for SEI studies to ensure reproducibility and full understanding of the material.

Model Materials Development and Characterization—The nature of the electrode-electrolyte interaction in silicon electrodes is at the heart of the formation and stability of the SEI. The synthesis of well-defined silicon nanoparticles and the different chemical markups of lithiated silicon surfaces is being probed by preparing model compounds and thin films that may/can exist in silicon anodes. Lithium silicides, silicates, and other inorganic material (LiF, Li_2O) are being prepared, and their reactivity with electrolytes is being determined. These materials also act as standard spectroscopy samples for the researchers who are looking at the formation of the SEI on different silicon materials.

SEI Characterization—The overall objective for SEISta is to understand the nature and evolution of the SEI on silicon anodes. The materials standardization and model compounds will enable the researchers to systematically investigate the formation of the solid-electrode interphase using a wide variety of spectroscopy techniques—from different optical, microscopy, and electrochemistry techniques—to determine how the SEI forms based on the nature of the silicon surface and how it evolves over time. This section of work will continue to grow in scope as we move beyond the sample-characterization phase of the project and toward understanding the nature and evolution of the SEI.

Science of Safety: Evaluating Temperature-Dependent Degradation Mechanisms of Silicon-Graphite Electrodes

Contributors: Yeyoung Ha, Donal Finegan, Bertrand Tremolet de Villers, Andrew Colclasure, Matthew Keyser (NREL)

Background

Silicon (Si) is a promising next-generation anode material as its alloying chemistry allows high specific capacity (~3,500 mAh/g_{Si} vs. 372 mAh/$g_{graphite}$) and its abundance satisfies the cost-effectiveness. However, the large volume change of Si during its lithiation and delithiation as well as the reactive nature of lithiated Si (Li_xSi) results in mechanical failure and continuous evolution of the solid–electrolyte interphase (SEI) at the anode. In addition, the high reactivity of Si-based anodes possesses intrinsic safety concerns. Thus, understanding the thermal behavior of Si-based electrodes and evaluating the degradation mechanisms at elevated temperatures is critical to develop successful, safe, long-lasting Si-based electrodes. Although differential scanning calorimetry (DSC) and accelerated rate calorimetry (ARC) are widely used to examine the thermal stability of electrode and electrolyte materials [1,2], electrochemical testing of Si-based electrodes at elevated temperatures needs to be further established. Here, we report the electrochemical protocols developed to test the thermal behavior of Si-graphite (Gr) electrodes. The performance of baseline electrolyte (Gen2, 1.2 M lithium hexafluorophosphate [$LiPF_6$] in ethylene carbonate [EC]/ethyl methyl carbonate [EMC] [3:7, w/w]) as well as the effect of fluoroethylene carbonate (FEC) additive, which is known to enhance the thermal stability of Si-based electrodes [1], are tested. This work is contribution to the Q3 (delayed to Q4) Milestone: "Implement protocols that enable comparisons of safety responses in silicon anodes as a metric for improving safety in silicon cells."

Results

The Si-Gr electrode was provided by the Cell Analysis, Modeling, and Prototyping (CAMP) Facility at Argonne National Laboratory. A mixture of 15 wt % Si, 73 wt % Gr, 2 wt % conductive carbon, and 10 wt % lithium polyacrylate binder (LiPAA) was coated on a 10-µm copper (Cu) foil current collector with a coating loading of 3.0 mg/cm^2. The thickness of calendered electrode was 27 µm, excluding the Cu foil thickness, and the porosity was 45.6%. 2032-type coin cells were assembled to test the electrochemical performance of Si-Gr/Li half-cells and Si-Gr/Si-Gr symmetric cells at 25°C, 45°C, and 70°C. All cells were cycled at C/20 for the initial 3 cycles, followed by 100 cycles at C/3, and finally at C/20 for 3 cycles. The current corresponding to 1C was 3.68 mA. Half-cells and symmetric cells were cycled between 0.05–1.5 V vs. Li/Li$^+$ and −0.5–0.5 V, respectively.

Half-cells. Figure II.1.B.1a shows the cycle performance of Si-Gr/Li cells in Gen2 and Gen2 + 10 wt % FEC electrolytes. Discharge capacity per gram of active material (Si+Gr) and coulombic efficiency (CE) are plotted as a function of cycle number. In the absence of FEC in the electrolyte, the first cycle lithiation capacity is greater at higher temperatures. However, the CE shows the opposite trend (i.e., lower first cycle CE at higher temperatures) and the capacity fades significantly faster in the following cycles at elevated temperatures. When FEC is present as an additive in the electrolyte, the first cycle lithiation capacity is relatively temperature-independent, although the CE is still lower at higher temperatures. Upon cycling at C/3 rate, greater discharge capacity is observed at higher temperatures and the cell cycled at 70°C shows best capacity retention after 100 cycles, albeit lower initial CE. As the cells are cycled at C/20 again after the C/3 cycles, less capacity is recovered at higher temperatures in both Gen2 and Gen2+FEC electrolytes. The capacity loss and temperature dependence are much greater in the Gen2 electrolyte.

To deconvolute the effect of Li metal on the performance of half-cells, Li/Li symmetric cells were tested using same electrolyte compositions (Gen2 and Gen2+FEC) and temperature conditions (25°C, 45°C, and 70°C) as in the Si-Gr/Li cells. A 0.7-mA/cm^2 constant current was applied for 2-h half-cycle to match the areal capacity observed at C/3 rate in half cells (~1.5 mAh/cm^2). The voltage evolution as a function of time is presented in

Figure II.1.B.1b. In the Gen2 electrolyte, the overpotential increases considerably faster at higher temperatures, whereas in the Gen2+FEC electrolyte, the Li/Li cell cycled at 70°C shows markedly stable performance. Enhanced Li metal performance at elevated temperature in the presence of FEC in the $LiPF_6$/carbonate-based electrolyte has been previously reported by Wang et al. [3]. The Li/Li cell performance closely resembles the temperature-dependent cycle performance of the Si-Gr/Li cells in Gen2 and Gen2+FEC electrolytes, indicating half-cells cannot be used to study the thermal behavior of Si-based electrodes.

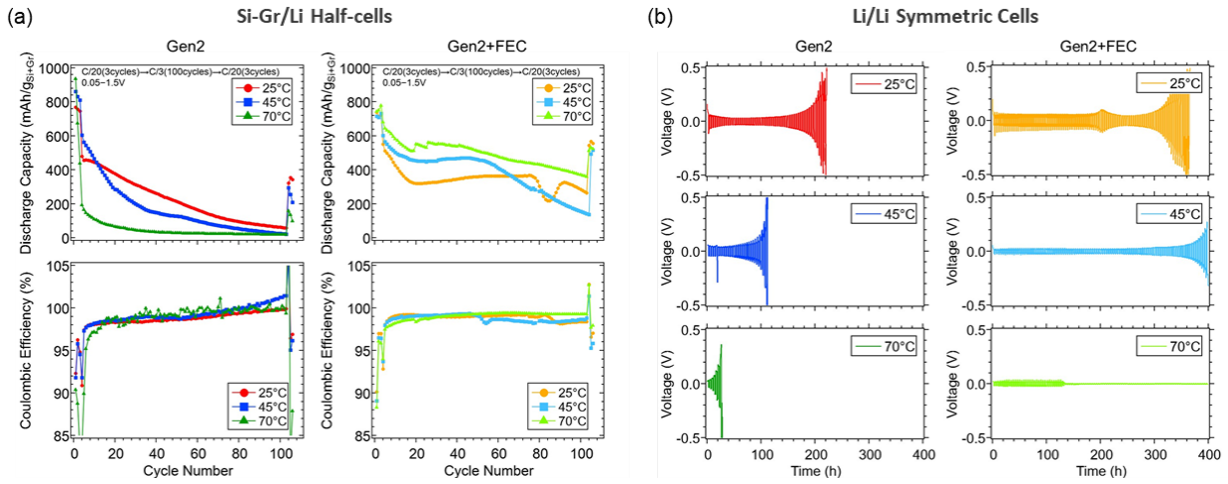

Figure II.1.B.1. (a) Discharge capacity per gram of active material (Si+Gr) (top) and coulombic efficiency (bottom) of Si-Gr/Li cells tested at 25 °C, 45 °C, and 70 °C in Gen2 (left) and Gen2+FEC (right) electrolytes plotted as a function of cycle number. (b) Voltage evolution of Li/Li cells upon plating and stripping in Gen2 (left) and Gen2+FEC (right) electrolytes at 25 °C, 45 °C, and 70 °C plotted as a function of time.

Symmetric cells. To exclude the effect of Li metal, a different cell configuration needs to be utilized to test the thermal behavior of Si-based electrodes. Whereas full cells reflect the cell environment closer to the commercial batteries, cathodes may introduce artifacts, such as transition metal dissolution and excess electrolyte decomposition at the cathodes, resulting in cross talks. By using symmetric cells, which consist of a pair of lithiated and delithiated anodes, the performance of Si-Gr electrodes can be studied without getting interference from foreign materials. Symmetric cells are fabricated by following the two-step process described in Figure II.1.B.2a. First, Si-Gr electrode is lithiated in a half-cell configuration by applying constant current (C/20) followed by voltage hold at 0.05 V with C/100 limit. Then, the half-cell is carefully disassembled and the lithiated electrode is retrieved. The lithiated electrode is paired with a delithiated Si-Gr electrode to make a symmetric cell. The comparison between the half-cell and symmetric cell configurations is summarized in Figure II.1.B.2b. Although the capacity fade due to the loss of active material will be detected in both half-cells and symmetric cells, the loss of Li inventory will be visible only in the symmetric cell configuration as half-cells have semi-infinite Li source. In addition, whereas the cell resistance will have contributions from both Si-Gr and Li electrodes in half-cells, the symmetric cell resistance can be correlated with the Si-Gr electrode performance.

The cycle performance of Si-Gr/Si-Gr cells at 25°C, 45°C, and 70°C in Gen2 and Gen2+FEC electrolytes are presented in Figure II.1.B.2c. In the Gen2 electrolyte, the cell cycled at 70°C shows best capacity retention and highest CE, whereas in the Gen2+FEC electrolyte, the cell cycled at 70°C shows worst performance. This observation is opposite from the half-cell results, manifesting once again the effect of Li metal on the half-cell performance. The enhanced performance of Si-Gr electrode in Gen2 electrolyte at 70°C is surprising, considering the low thermal stability of $LiPF_6$ and high reactivity of Li_xSi. Such observation can be correlated with a previous DSC study by Profatilova et al. [1] in which the presence of PF_6^- anion enhanced the thermal stability of Li_xSi as it created LiF upon decomposition, which has an excellent thermal stability. In the Gen2+FEC electrolyte, the capacity retention is enhanced compared to the Gen2 electrolyte and the 25°C cell

shows best performance. Although the presence of FEC is known to enhance the thermal stability of Si-based electrodes from the DSC studies [1], the main exothermic peak appears at temperatures well above 100°C, and hence at 70°C its positive effect may not be clearly observed. Instead, greater parasitic reactions at 70°C, which was observed as the lower CE in half-cells with the Gen2+FEC electrolyte, may lead to faster Li inventory consumption and corresponding capacity fade when the symmetric cells are cycled.

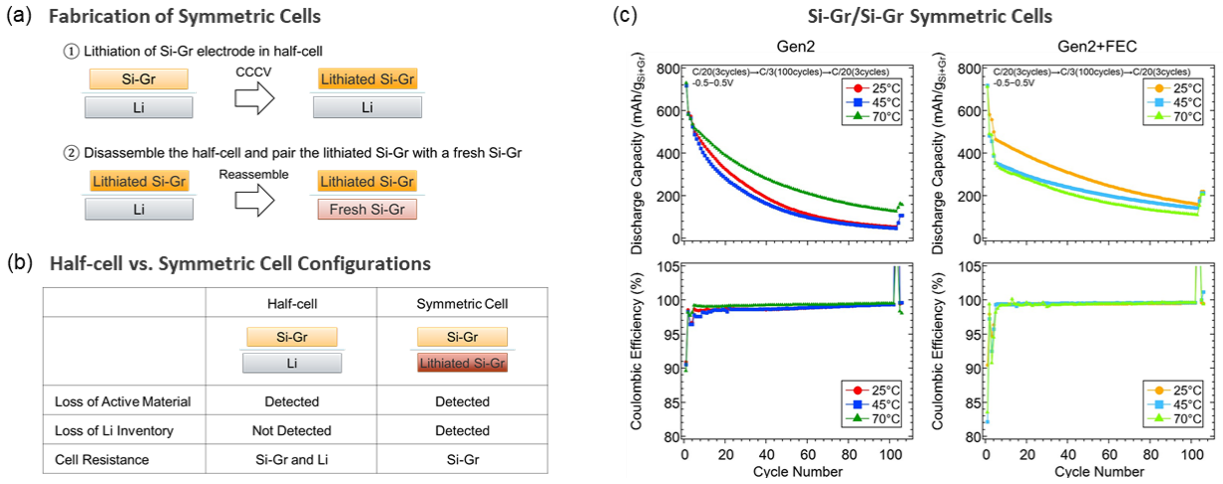

Figure 1. (a) Schematic diagram of symmetric cell fabrication process. (b) Comparison of half-cell and symmetric cell configurations. (c) Discharge capacity per gram of active material (Si+Gr) (top) and coulombic efficiency (bottom) of Si-Gr/Si-Gr cells tested at 25 °C, 45 °C, and 70 °C in Gen2 (left) and Gen2+FEC (right) electrolytes plotted as a function of cycle number.

Deconvoluting the Degradation Mechanisms. While Si-Gr/Si-Gr symmetric cells can exclude the effect of Li metal, their degradation results from a combination of two different loss mechanisms—loss of active material and loss of Li inventory. To further deconvolute the degradation mechanisms at each temperature, symmetric cell and half-cell configurations were combined. The experimental design is presented in Figure II.1.B.3a. Steps 1 and 2 describe the fabrication and cycling of symmetric cells. At the end of the symmetric cell cycling, a half-cycle is added to delithiate the initially lithiated electrode (color coded as yellow). Then, in Step 3, the cycled symmetric cell is disassembled and the delithiated electrode is reassembled into a half-cell, where it is lithiated again. By comparing the lithiation voltage profiles during Steps 1 and 3 (i.e., before and after the symmetric cell cycling), information on the loss of active material during the symmetric cell cycling can be obtained.

Figure II.1.B.3b shows the capacity loss (%) in half-cells, symmetric cells, and reassembled cells. For the half-cells and symmetric cells, lithiation capacity of the 2nd and the 104th cycles (i.e., C/20 cycles before and after the C/3 aging cycles) are compared. For the reassembled cells, lithiation capacity during Steps 1 and 3 are compared as described previously. In half-cells, both Gen2 and Gen2+FEC electrolytes show increasing capacity loss at higher temperature, with much less degree in the presence of FEC in the electrolyte. If Li metal were behaving like an ideal electrode, the capacity loss would be close to half of that of the symmetric cells, which have two Si-Gr electrodes. However, in the Gen2 electrolyte, the capacity loss in half-cells is more than half of that in symmetric cells due to the adverse effect of Li metal—at 70°C, the capacity loss is even larger in half-cells. In symmetric cells, smallest capacity loss is observed at 70°C in the Gen2 electrolyte and at 45°C in the Gen2+FEC electrolyte. At all temperatures, the capacity loss is smaller in the Gen2+FEC electrolyte, demonstrating the enhanced performance of the Si-Gr electrode in the presence of FEC. In the reassembled cells, less capacity loss is observed at higher temperatures in both Gen2 and Gen2+FEC electrolytes, indicating less active material loss at elevated temperatures. One possible explanation of such behavior is the soluble nature of the SEI, which is facilitated at higher temperatures [4], allowing the Li^+ ion transport network within the electrode to be maintained. The SEI composition at elevated temperatures may also play a role. By

comparing the capacity loss in symmetric cells and reassembled cells, capacity loss due to the loss of Li inventory can be obtained. The difference between the capacity loss in symmetric cells and reassembled cells increase at higher temperatures, indicating that the loss of Li inventory is the major degradation mode contributing at elevated temperatures, rather than the loss of active material.

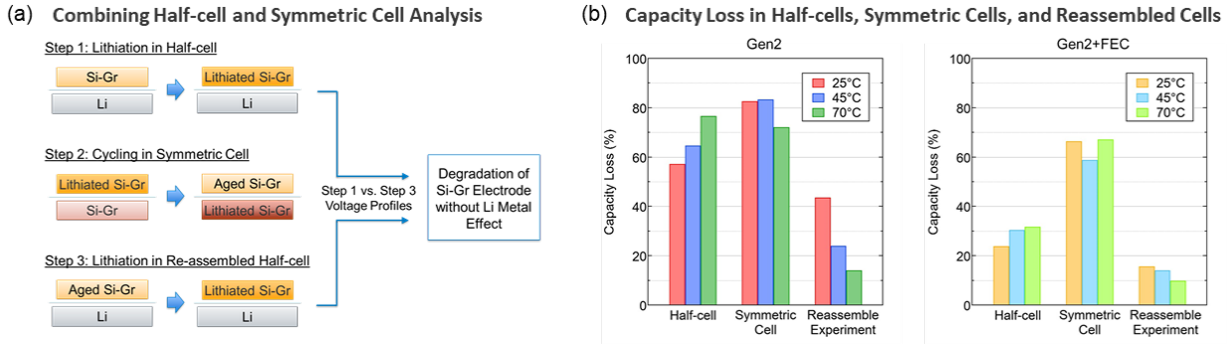

Figure 2. (a) Schematic diagram of experimental design combining half-cell and symmetric cell configurations to deconvolute the degradation mechanisms of Si-Gr electrodes at different temperatures. (b) Capacity loss in half-cells, symmetric cells, and symmetric cell cycled electrodes reassembled into half-cells. Capacity of the C/20 cycle before (2nd) and after (104th) the C/3 cycles are compared.

Conclusions

Thermal behavior of the Si-Gr electrode was electrochemically tested using different cell configurations. The Si-Gr/Li half-cell results combined with the Li/Li symmetric cell results demonstrate that the Li metal effect obscures the Si-Gr electrode performance and hence half-cells are not ideal for testing thermal behavior of Si-based electrodes. By utilizing Si-Gr/Si-Gr symmetric cells, the true Si-Gr performance can be studied. However, the capacity fade in symmetric cells is a combination of the loss of active material and the loss of Li inventory. By reassembling the symmetric cell cycled electrodes into half-cells and comparing the lithiation voltage profiles before and after the symmetric cell cycling, the information on loss of active material can be obtained. The results demonstrate that the major degradation mode at elevated temperature is the loss of Li inventory, rather than the loss of active material. To further understand the temperature dependent degradation mechanisms, chemical and morphological evolution of the electrodes will need to be evaluated via spectroscopic and microscopic analyses on the cycled electrodes.

Moving forward, the thermal stability of the SEI at elevated temperatures and how it relates to the reactivity of the cell as it enters thermal runaway will be studied by utilizing DSC and ARC measurements in combination with the electrochemical testing. The intrinsic reactivity of Si and Li_xSi as well as the high surface area of nanometer-sized Si particles in the electrode possess greater challenges compared to the Gr anodes. In addition, the electrolyte components, such as carbonate solvents and $LiPF_6$ salt, readily react with Si, further complicating the system. The thermal stability of different electrode formulations and electrolyte chemistries will be examined to gain insight into the factors affecting the safety of Si-based batteries.

Zintl Phase Formation Mechanism and its Effect on SEI

Contributors: Andrew Norman, Andriy Zakutayev, Anthony K. Burrell, Baris Key, Binghong Han, Bertrand J. Tremolet de Villers, Caleb Stetson, Chun-Sheng Jiang, Fulya Dogan, Glenn Teeter, Jack Vaughey, Max Schulze, Mowafak Al-Jassim, Nathan Neale, Niya Sa, Ritesh Uppuluri, Saida Cora, Sang-Don Han, Steve Trask, Xiang Li, Yeyoung Ha, Yunya Zhang, Zhifei Li, Zoey Huey

Interfacial Zintl Phase Formation Background

In 2018–2019 a significant advance in silicon surface stability was reported in the SEISta program. The advance was based on the addition of a Mg-ion source to the electrolyte and its eventual incorporation into the silicon surface on cycling. Spectroscopically, the Mg ion was found to be incorporated into the lattice to form a ternary Li-Mg-Si phase of an approximate refined composition $Li_{14}Mg_{g}Si_4$, a lithium-ion conductor with a stable electron configuration. Model compounds of this and related stoichiometries (same phase diagram tie-line) showed dramatically lower reactivity with electrode components and active materials, notably the electrolyte. In FY 2020, work was initiated to better understand this phenomenon and differences with other electrolytes and better characterize the phases formed and their lifetimes in the cell environment. As part of the SEISta effort, the formation mechanism of ternary Zintl phase formation on Si thin film electrodes were characterized in their as-prepared pristine state, after first lithiation, after first delithiation half cycles, and after 500 full cycles. The different possible formation pathways for the ternary Zintl phase were investigated through lithiation/delithiation of Si thin film in program electrolytes with $Mg(TFSI)_2$ salt in mixed carbonate Gen2 (or Gen2F) electrolytes. For comparison, direct deposition of Mg vapor on Si thin films was used to create a fully surface magnesiated (lithium-free) Mg_2Si coating on the film as a model compound to evaluate lithium diffusion, and a series of silicon wafers were used to evaluate the additives on a larger scale for spectroscopic studies. The electrodes and electrode surfaces were characterized by STEM-EDS and SSRM was employed to investigate the electrode structures. Samples and electrodes based on nanocrystalline silicon were investigated by magnetic-angle spinning nuclear magnetic resonance (MAS-NMR) and X-ray diffraction.

Characterization Results

Silicon Thin Films: Amorphous silicon (a-Si) thin films were prepared via magnetron sputtering. In these cases, 50-nm a-Si was deposited on a Cu foil substrate, in addition to a second series of electrodes with an additional deposition layer of 20-nm elemental Mg (Figure II.1.B.4). For the Mg/Si samples, transmission electron microscopy (TEM) cross sections were prepared of both the pristine and cycled samples using focused ion beam (FIB) milling and were then transferred in an air-free environment to the STEM system. STEM-EDS studies were used to investigate the chemistry and morphology of the initial surface Zintl phase formation as well as after 500 cycles in GenF electrolyte. STEM-EDS was used to create elemental maps of the pristine electrode (Fig. II.1.B.5) and it indicated an approximately 60-nm-thick, 2D structure with Mg covering the Si thin film. Some intermingling of the Mg and Si was observed, indicating probable diffusion of some Mg into the Si structures prior to cycling. This use of Mg/Si layered thin films helps better define the amount of Mg at the electrochemical interface. Preliminary work reported last year indicated that the probable mechanism of ternary phase formation was Mg^{+2} ion exchange with $Li_{13}Si_4$ at low voltage. These studies explored the stability of the phases formed, investigating if, mechanistically, Li^+ ions exchanged with fully reduced Mg_2Si or Li-Mg alloys should be considered intermediaries in the process. On initial cycling, these Mg/Si film model anodes did demonstrate formation of a ternary Li-Mg-Si Zintl phase by lithiation of the binary Mg/Si film.

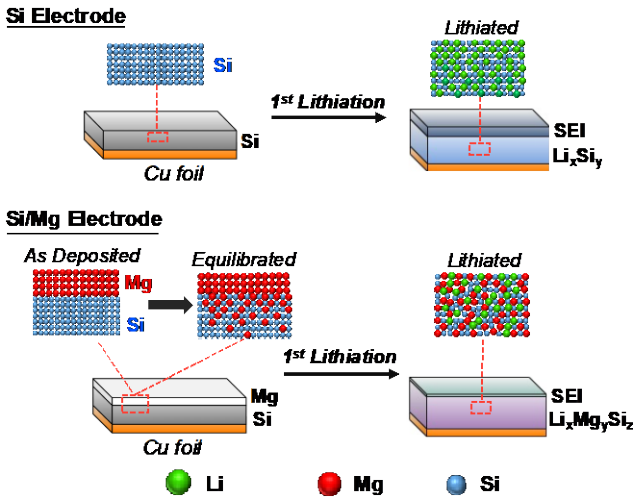

Figure II.1.B.4. Conceptual diagram illustrating pristine and lithiated amorphous Si and Si/Mg thin film electrodes.

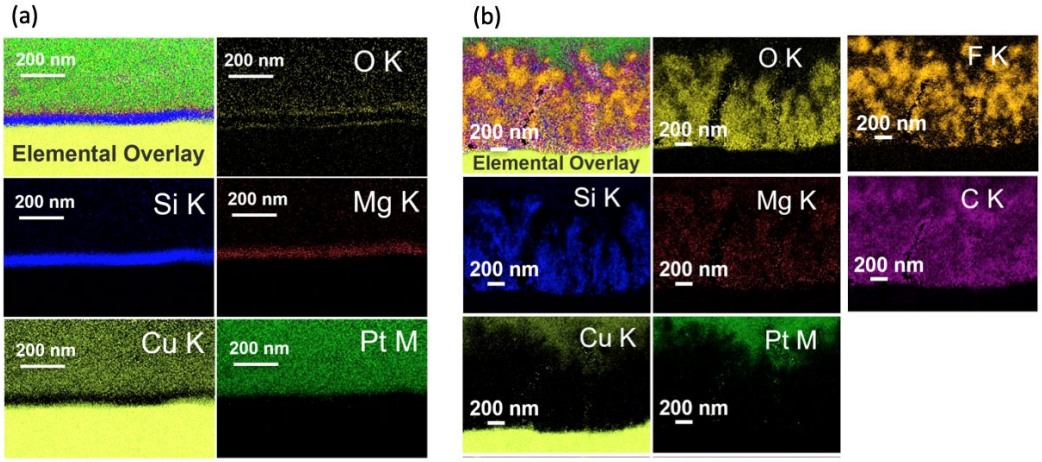

Figure II.1.B.5. STEM-EDS elemental maps of: (a) a pristine thin film electrode prepared by deposition of 20-nm Mg on 50 nm of a-Si and (b) after 500 cycles in Gen2F.

To better understand the buried interfaces, SSRM resistivity vs. depth experimental profiles were carried out on the three model systems: (1) a-Si in GenF electrolyte (Mg-free reference), (2) a-Si in GenFM electrolyte (Mg added via $Mg(TFSI)_2$ salt as an electrolyte additive), and (3) a 20-nm Mg deposited on a-Si in GenF electrolyte (metallic Mg added to the surface of the Si electrode). These three systems were each investigated (1) in their pristine condition, (2) after the first lithiation half cycle, and (3) after the first full electrochemical cycle (Fig. II.1.B.6).

In comparison to the pristine Mg-free Si, the 20-nm Mg on Si pristine electrode shows a superficial resistive oxide (MgO) coating on top of a very conductive layer of metallic Mg. This is consistent with other measurements performed on these systems and the high oxophilicity of magnesium metal. The Si in this sample exhibits a lower resistivity compared to Si in the Mg-free system, suggesting that some diffusion of Mg into Si occurs during the Mg deposition process, resulting in an enhancement in the conductivity of Si. This evidence of diffusion prior to cycling is consistent with the STEM-EDS results. After the first lithiation, a resistive SEI forms on all samples. In the Si in GenF (Mg-free) system, the SEI layer is thin (~8 nm), and the resistivity of Si is halved due to lithiation of Si. In the Si in GenFM system, the SEI layer was found to be thicker (~18 nm), whereas the structure beneath the layer was measured to be very conductive (100 Ω·cm vs. 103 Ω·cm for the pristine Si), suggesting localized or heterogenous Mg reduction at the site of the resistivity

vs. depth profile measurement. Lastly, the 20-nm Mg on Si sample shows a highly resistive SEI film, a disappearance of the metallic Mg, and a similar resistivity decrease for Si as that observed in the Mg-free sample due to lithiation of the Si. After a full electrochemical cycle (lithiation then delithiation), all electrodes showed similar resistivity-depth profiles; high resistivity due to an SEI layer was not detected and a 2–3 order of magnitude increase in resistivity compared to the pristine electrodes was measured in all electrodes. Results are summarized in Figure II.1.B.6, with observed trends summarized in Table 1. Based on these data, analysis indicates that the SEI is likely unstable and changes as a function of state of charge, decomposing during the delithiation half cycle with the Si thin film electrode becoming porous and more resistive after Li and Mg migration back into the electrolyte.

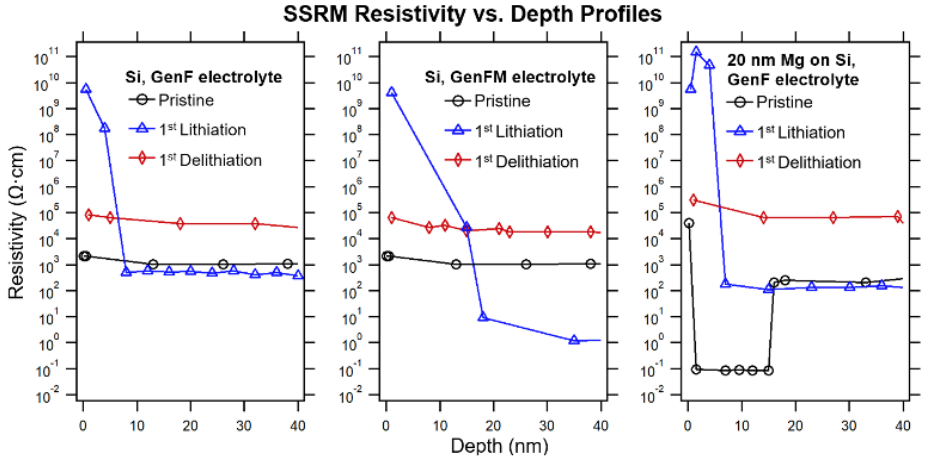

Figure II.1.B.6. SSRM resistivity vs. depth profiles of pristine, lithiated, and delithiated electrodes for Si in Gen2F electrolyte, Si in Gen2FM, and Mg/Si Gen2F.

The phases lost have provided some insights on the electrochemical activity and instability of the interface and also have the action of enriching the interface in inorganic phases (i.e., LiF) that cannot be easily solubilized and transported in the electrolyte, as noted in Figure II.1.B.5b.

The diffusion of Mg into bulk Si layer was also examined via STEM-EDS elemental maps of an FIB-prepared cross-sectional sample of the Si/Mg electrode (Figure II.1.B.5). STEM-EDS results include high-angle annular dark-field (HAADF) imaging and EDS maps for Si, Mg, Cu, and Pt. As observed in these results, there is a layered structure of Mg on Si, with some elemental overlap between the two species at their interface. This suggests that after Mg deposition, although the surface Mg layer remains, a nontrivial amount of the deposited Mg diffuses into the bulk Si layer. This elemental mapping shows agreement with the reduction of resistivity of the bulk Si in the Si/Mg electrode measured with SSRM resistivity vs. depth profiling (Figure II.1.B.8).

Table-1: Summary of Initial Zintl Phase Formation on Si Thin Film

	Si, GenF electrolyte (Mg-free reference)	Si, GenFM electrolyte (Mg as electrolyte salt)	Mg on Si, GenF electrolyte (Mg as metal)
Pristine Electrode	a-Si: ~10^3 Ω·cm	a-Si: ~10^3 Ω·cm	Superficial MgO, metallic Mg (10^{-1} Ω·cm), a-Si: ~3 × 10^2 Ω·cm (decrease in resistivity likely due to Mg diffusion into Si)

1st Lithiation: SEI	Thin, resistive SEI (~8 nm)	Resistive SEI, thicker than Si in GenF (~18 nm)	Thin, highly resistive SEI (~7 nm
1st Lithiation: Si	Resistivity halved from pristine electrode (due to conductivity enhancement of Li_xSi_y compared to a-Si)	Resistivity decreased by three orders of magnitude, likely due to heterogenous reduction of Mg from electrolyte	Resistivity halved from pristine electrode (due to conductivity enhancement of Li_xSi_y compared to a-Si), no metallic Mg detected
1st Delithiation: SEI	Little to no SEI detected	Little to no SEI detected	Little to no SEI detected
1st Delithiation: Si	~2 orders of magnitude increase in resistivity from pristine electrode	~2 orders of magnitude increase in resistivity from pristine electrode, Mg likely migrates to electrolyte	~3 orders of magnitude increase in resistivity from pristine electrode, Mg likely migrates to electrolyte

Literature reports indicate that the interface between the Si and Mg layers consists of a thin layer of Mg_2Si (~1 nm), where the only stoichiometric Mg silicide reported may form [5]. In these reports, the lithium reactivity of Mg_2Si has been investigated with formation of a ternary Zintl phase noted using powder X-ray diffraction. Due to the high magnesium content, poor cycling performance in part due to phase separation and expulsion of Mg during cycling was reported [6]. In this evaluation, we prepared Mg_2Si film as a reference by depositing Si and then Mg film on copper foil through annealing of the deposited films. The formation of Mg_2Si was validated by X-ray diffraction (XRD) (Figure II.1.B.8). These materials allowed us to have a reference for the fully reduced and magnesiated endmember. Samples were investigated with Raman spectroscopy (see Figure II.1.B.8d) and two sharp peaks were observed at 256 and 344 cm^{-1}, which are assigned to the F_{2g} and F_{1u} phonon bands of Mg_2Si, respectively [7]. The pure Si film shows only a broad band centered around 469 cm^{-1}, assigned to a-Si [8]. In the case of the Si/Mg electrode, two minor peaks are observed at 254 and 344 cm^{-1}, along with a broad peak at 469 cm^{-1}, indicating the presence of both Mg_2Si and Si in the Si/Mg electrode. The experimental evidence posed by the SSRM, EDS, and Raman spectroscopy analysis suggests that some of the metallic Mg coating diffuses into the Si layer, coincident with a minor amount of Mg_2Si formed at the interface of the Mg and Si films. Cyclic voltammetry (CV) studies of the Si and Mg/Si electrodes were used to gain insights about the Mg coating on Si during the lithiation/delithiation processes. In the first CV cycle, the pure Si electrode shows two large cathodic peaks and two corresponding anodic peaks in the low potential region, representing the Li-Si lithiation, respectively (Figure II.1.B.7). In contrast, the Si/Mg electrode showed only one broad cathodic peak and one anodic peak associated with Li-Si reactivity, with a larger overpotential when compared to the pure Si electrode. This may reflect the lithiation of magnesium (Li-Mg) as an energy barrier to reacting with the underlying silicon, the difficulty in lithiating the Mg_2Si interface, or the broad redox peaks of the Si/Mg electrode, possibly resulting from the large polarization of surface MgO with slower lithiation kinetics. The Si/Mg electrode also displays an additional anodic peak at 0.18 V, which is attributed to the Li-Mg de-alloying process.

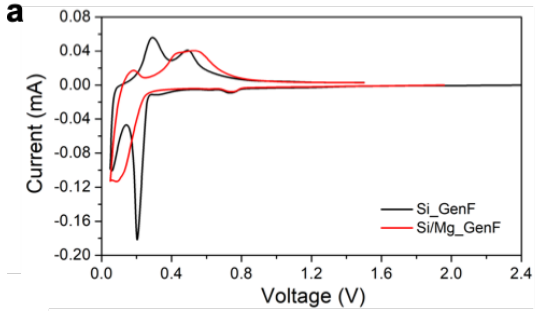

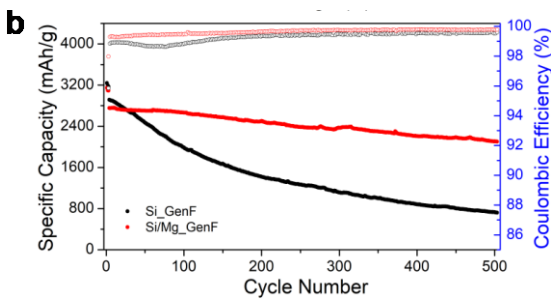

Figure II.1.B.7. Electrochemical performance evaluation of the Si and Si/Mg electrodes with GenF electrolyte in the potential range of 0.05–1.5 V. (a) The first CV cycle under scan rate of 0.1 mV/s. (b) The extended cycling performance with the first three cycles under a current density of 0.1 C and the subsequent cycles carried out at 1 C.

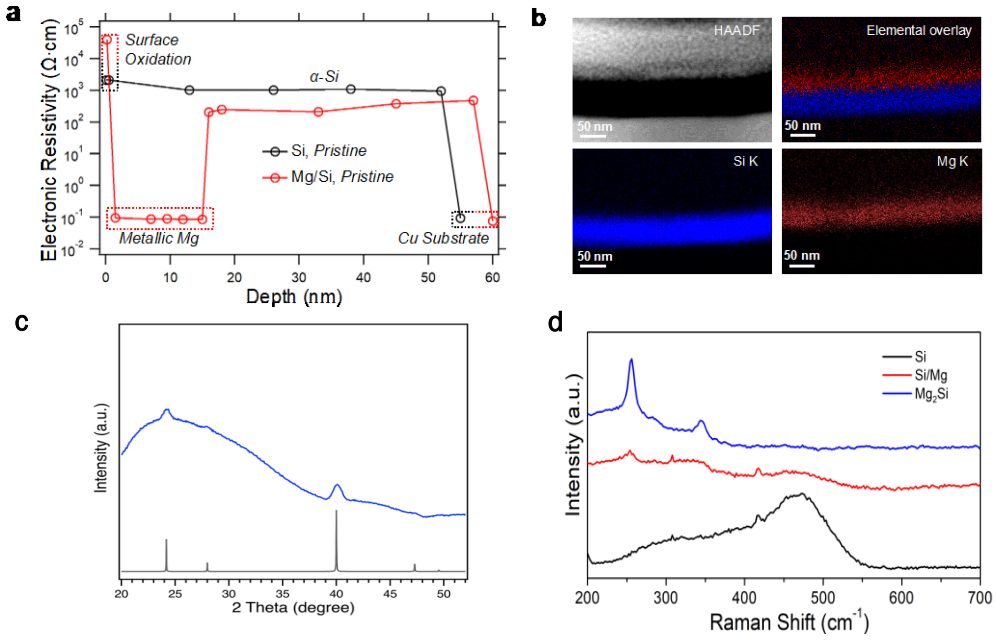

Figure II.1.B.8. (a) SSRM resistivity vs. depth profile of pristine Si and Si/Mg electrodes. (b) STEM cross-sectional HAADF image and EDS elemental maps of Si K, Mg K, and elemental overlay of Si and Mg maps of the pristine Si/Mg electrode. (c) Raman spectra of pristine Si, Mg_2Si, and Si/Mg electrodes. (d) XRD pattern (blue trace) is of Mg_2Si deposited on glass substrate and the gray pattern is from the Mg_2Si standard.

The impact of the Mg coating on the cycling stability of the Si electrode was also evaluated by galvanostatic long-term cycling tests. The electrochemical cycling performance of Si and Si/Mg electrodes was tested at 0.1 C (3.9 μA/cm^2) for three formation cycles and then at 1 C for remaining cycles. The capacity retention of the Si electrode was measured to be 25% after 500 cycles at 1 C, in sharp contrast to the 76% capacity retention of the Si/Mg electrode (Figure II.1.B.6b). Moreover, the CE of the Si/Mg electrode was higher than that of the Si electrode during the entire cycling process, indicating less parasitic side reactions and a more stable SEI.

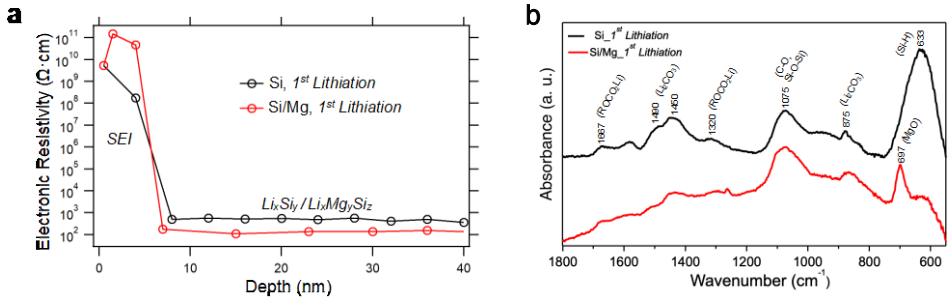

Figure II.1.B.9. Characterization of the electrodes after the first lithiation at 0.1 C in GenF. (a) SSRM resistivity vs. depth profiles of Si and Si/Mg electrodes. (b) ATR-FTIR spectra of Si and Si/Mg electrodes.

STEM-EDS of a similar electrode after 500 cycles in GenF (Fig. II.1.B.7b) revealed a 3D intermixed layer of active material and SEI with an approximate thickness of >1 μm that was found to contain significant amounts of C, O, and F in addition to the Si and Mg active materials. STEM-electron energy loss spectroscopy (EELS) and transmission electron diffraction (not shown) revealed significant amounts of crystalline LiF present in the SEI region. This result illustrates the large expansion of Si active material and significant ingress of SEI into the active material by the cycling.

To understand the interfacial origins of the enhanced cycling stability observed for the Si/Mg electrode, ex situ SSRM resistivity depth profiles for Si/Mg and Si electrodes after the first lithiation were performed. Compared with their pristine electrodes (Figure II.1.B.8a), the electronic resistivity of the surface layer of the lithiated electrodes sharply increased for both Si and Mg coated Si electrodes due to the formation of SEI (Figure II.1.B.9a). The resistivity drops dramatically after approximately 8 nm, which corresponds to the thickness of the SEI layer. The surface resistivity of the SEI formed on the Si/Mg electrode is greater than that formed on the Si electrode, suggesting that the Mg coating may promote an SEI with different surface composition that is more electronically resistive, and therefore more effective in the suppression of further electrolyte decomposition. In addition, the SEI formed on the Si electrode may be slightly thicker than that of Si/Mg, as indicated in SSRM vs. depth profiles (Figure II.1.B.9).

In addition, the attenuated total reflection (ATR)-FTIR spectra of the lithiated Si and Si/Mg electrodes also reveal differences between the SEI of these two electrodes (Figure II.1.B.9b). The FTIR spectra of the lithiated Si and Si/Mg electrodes exhibit similar features in general, but close examination of the spectra reveals differences. The large peak at approximately 633 cm^{-1}, which is assigned to Si-H bond, is observed only from the lithiated Si electrode [9]. This peak is suppressed in Si/Mg, indicating that there is little free Si on the surface of lithiated Si/Mg electrode as the pristine Si/Mg electrode was covered with Mg. The lithiated Si/Mg electrode has a large peak around 700 cm^{-1} that we attribute to MgO, which can be readily formed from magnesium on the surface reacting with residual oxygen in the glovebox [10]. Furthermore, the Si sample exhibits several peaks associated with the formation of surface lithium carbonate (Li_2CO_3)—1490, 1450, and 875 cm^{-1}—and lithium alkyl carbonate ($ROCO_2Li$)—1667 and 1320 cm^{-1} [13]. Most of these peaks are significantly diminished in the Si/Mg sample, corroborating the idea that Mg coating reduces the reactivity of the anode with the electrolyte and leads to thinner SEI with fewer decomposition products on the surface.

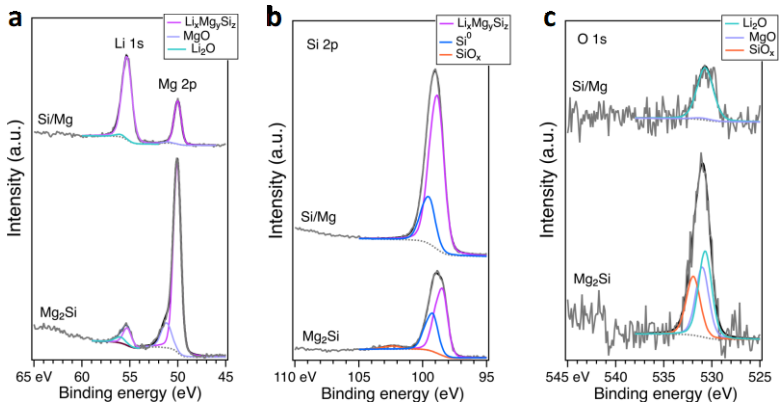

Figure II.1.B.10. High-resolution XPS spectra of the Si and Si/Mg electrode after the first lithiation in GenF electrolyte obtained from depth profiling after 14 sputtering cycles with Ar ion. (a) Li 1s and Mg 2p, (b) Si 2p, and (c) O 1s.

The Li 1s, Mg 2p, and Si 2p spectra from the bulk layer after 14 sputtering cycles were further analyzed to study the possible formation of Zintl phase (Figure II.1.B.10). In both Si/Mg and Mg_2Si electrode, most of the Li 1s is associated with ternary Zintl phase with some minor contribution from Li_2O. It is worth noting that after the same sputtering cycles, the Si/Mg contains more Li than the Mg_2Si electrode, which should be due to the slow lithiation (and magnesium displacement) kinetics of Mg_2Si. For Mg 2p, both of the electrodes display sharp Mg 2p peak, where the main component is associated with Zintl phase with minor contribution from MgO. The Si 2p peaks for both electrodes consist of Si metal and Si from Zintl phase. The existence of Si metal suggests that the electrode have not been fully lithiated after the first lithiation. As the O 1s peak of Mg_2Si is much higher than that of Si/Mg, there is more oxygen at this depth for Mg_2Si, which is related to Li_2O, MgO, and SiO_x. Overall, both the Mg 2p and Si 2p results suggest the formation of Li-Mg-Si ternary Zintl phase of the Si/Mg anode upon lithiation, even though its composition is different from that of the Mg_2Si anode. Therefore, the XPS depth profiling with the reference Mg_2Si electrode clearly demonstrates that the introduction of Mg coating on the surface of Si anode could lead to the formation of Li-Mg-Si ternary Zintl phase upon lithiation, which alters the surface SEI and improves the cycling stability of the Si anode.

Silicon Wafers: Commercially sourced silicon wafers were used to evaluate the surface reactions of the multivalent electrolyte additives, as they present a relatively flat and homogenous surface for spectroscopic studies. In these studies, XPS experiments were performed on Si wafer model electrodes that were lithiated (cycled) in either GenF or GenFM electrolytes. Depth analysis of the data demonstrated that a thinner SEI layer was formed in the GenFM electrolyte compared to the system without the additive. The results are consistent with a Mg-containing modified surface passivation formed in the presence of $Mg(TFSI)_2$. To establish the role of surface oxide contamination, we hydrofluoric acid (HF) etched the surface oxides and electrochemically treated the wafer samples to change the electrode surface to a hydrogen-terminated Si wafer. Samples were characterized using XPS depth profiling and the results were compared with the spectra for the native oxide Si wafer electrodes. In both H-terminated and baseline native oxide Si wafer electrodes lithiated using GenFM, no clear spectroscopic evidence for a Li-Mg-Si ternary Zintl phase formation was seen, although the low surface area of the silicon wafer and limited contact time may have resulted in very thin film due to a limited electrolyte penetration depth. Consistent with the oxophilicity of solubilized Mg ions, MgO was detected in the SEI layer, which may block active sites at the electrochemical interface. Analysis of the Li-Mg-Si system indicates that although the wafer model is useful for several different spectroscopic studies, its low surface area and relatively defect-free interface probably limits the penetration depth of the solubilized Mg ions, and thus significant formation of any binary (Li-Si) or ternary (Li-Mg-Si) reduced phases. Reduction of the wafer surface oxide thickness by HF etching was found to have limited effect on the experimental observations.

Nanocrystalline Powders: Although thin films and wafer have advantages, their low surface area and low defect concentration can make them difficult substrates for mechanisms that rely on surface diffusion at the interface. Powders, due to processing, synthesis, and history, have a more heterogeneous surface, which should lend itself to these electrolyte-mediated surface reactions. In fact, the samples that magnesiated most uniformly were those with the least organized and organized silica coating. Whereas traditional diffraction techniques are especially sensitive to heavy atoms and work best with materials with long-range order, the Li-related structures associated with amorphous Si phases after cycling require a local probe. NMR is a powerful tool to determine the local structural environments of nuclei such as ^{7}Li, ^{31}P, and ^{19}F. In FY 2020, we studied the electrochemical lithiation of a baseline Paraclete Energy Si anode at multiple charge states to gain insights into Zintl phase formation mechanisms.

In the first-cycle electrochemical profiles, high-resolution ^{7}Li NMR spectra and the corresponding spectral simulation from unwashed pouch cells are shown in Figure II.1.B.11. Four main Li resonances are observed and analyzed: the black peak around 0 ppm is from the residual diamagnetic Li salts in electrolyte, as well as electrolyte decomposition products; the relatively sharp and narrow component at −1 ppm is assigned to Li^+ in

surface Si-O layer; Li^+ in isolated Si is at 8 ppm; and Li^+ in Si clusters resonates over 13 ppm. These peak assignments are consistent with our previous ex situ ^7Li NMR studies on coin cells. The electrochemical profiles are very similar for both Gen-2 + FEC (GF) and Gen-2 + FEC + Mg (GFM) electrolytes when the cells are only discharged to 100 mV, while GF shows slightly higher (~30 mAh/g) specific capacity. As a result, most Li ions are inserted into isolated Si (and/or extended silicon clusters) with 97.1% in GFM and 97.8% in GF. When completely discharged to 10 mV, as seen in Figure II.1.B.13a, although GF and GFM share the similar discharging profile, the GF cell holds more Li ions (~140 mAh/g) than GF. At this stage, Li insertion into Si clusters, as well as possible migration from isolated Si, eventually forms over-lithiated Si phases. Upon charge, Li extraction preferentially take place in over-lithiated Si phases, then Si clusters and finally isolated Si, which correlates well with the coin cell data. When charged to 400 mV, GF and GFM series represent Li removal hysteresis to different extents. There is still 24.7% Li in Si clusters and 57.7% Li in isolated Si in GFM cell, compared with almost all Li in isolated Si in the GF cell. At the fully charged state, spectra shift toward lower frequency, indicating reversible Li dynamics.

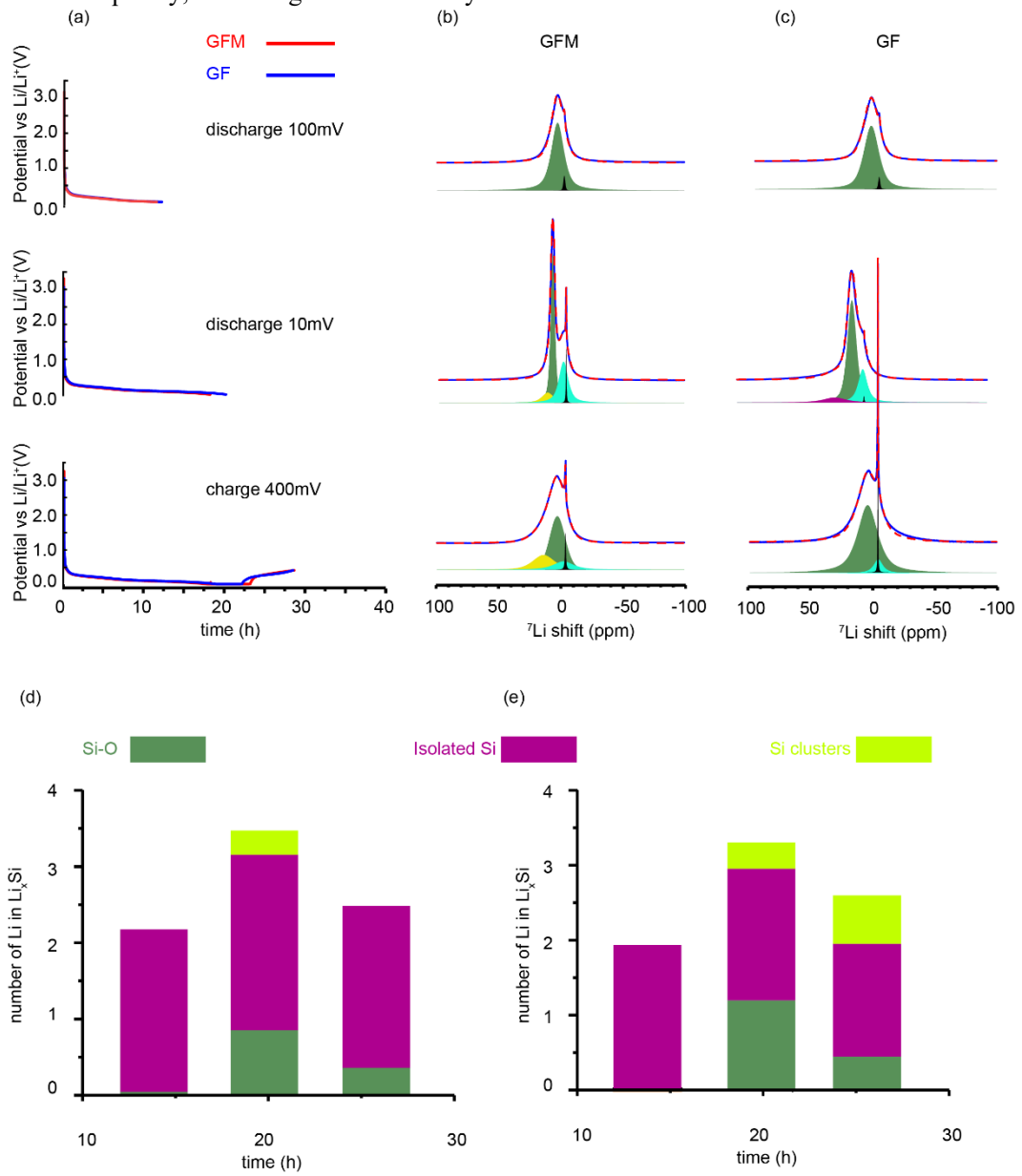

Figure II.1.B.11. Electrochemical performance of GF and GFM at 100 mV, 10 mV, and 400mV. (a) Experimental data (solid line) and simulation (dash line) of GFM (b) and GF (c), Li quantification with GF (d), and GFM (e) electrolytes.

^{7}Li NMR spectra comparison between pouch cells and half cells is shown in Figure II.1.B.12. At the early state (above 100 mV), there is no significant difference except broader line shape for pouch cells, which is due to the relatively lower MAS rate (20 kHz) of the NMR experiment when compared with that of coin cells (60 kHz). However, at the fully discharged state, both GF and GFM spectra show significant differences compared to the results for the coin cells. More Li content was found to be in the SEI and Si-O layer in pouch cells, which is likely due to the fact that pouch cells have significantly more electrolyte and larger surface areas, leading to more side reactions on the surface and SEI formation. As shown in **Figure** II.1.B.11b, Figure II.1.B.12, and Figure II.1.B.13, 52.9% Li in isolated Si and 10.8% Li in Si clusters indicate that ternary phase formation may require more Li insertion into Si clusters as well as over-lithiated Si. In contrast, with additional 140-mAh/g discharge capacity, GF pouch cell spectrum shifts to lower field and shows over-lithiated Si at 22 ppm. Longer voltage hold at 10 mV may be accelerating co-insertion of Mg^{2+} and Li-Mg-Si ternary formation in GFM cells.

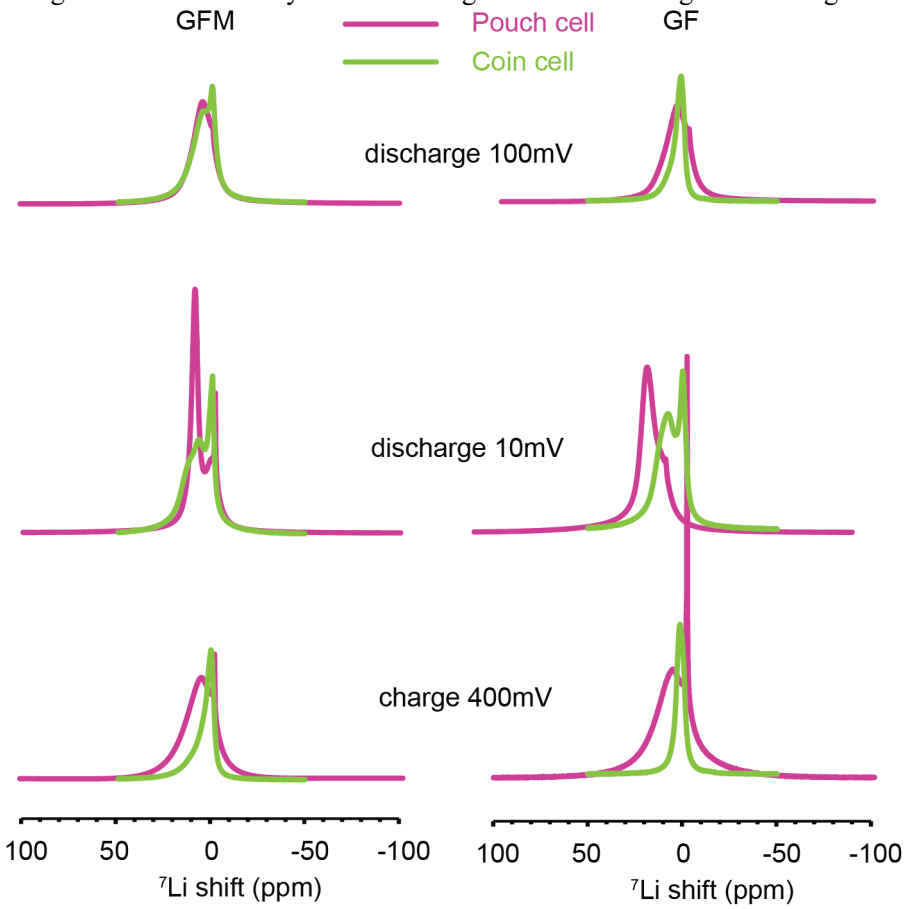

Figure II.1.B.12. ^{7}Li NMR spectra comparison between pouch cells (purple) and coin cells (green) for GFM and GF.

In Figure II.1.B.13, the discharge electrochemistry of baseline Paraclete Si is characterized by two distinct voltage plateaus at 230 mv and 100 mV, which correspond to a two-phase reaction: an irreversible dissociation of amorphous Si and a crystalline phase formation of $Li_{15}Si_4$. Voltage hold at 10 mV before delithiation is designed to break up all crystalline $Li_{15}Si_4$ and form amorphous Li_xSi upon charge, representing a broad voltage peak at 280 mV. Note that although GF and GFM share similar voltage profiles, subtle shift towards lower voltage at 100 mV is most likely a sign of Mg co-insertion. During deeper discharging process below 100 mV, Mg^{2+} could participate in lithiation to form Li-Mg-Si ternary by two possible mechanisms:

(1) $Li_{3.75}Si + 0.1Mg^{2+} => Li_{3.55}Mg_{0.1}Si + 0.2Li^{+}$

Li ions continue coordinating with Si and form crystalline $Li_{3.75}Si$ first; ion exchange between Li^{+} and Mg^{2+} is driven by low potential.

(2) $Li_{3.55}Si + 0.1Mg^{+2} \Rightarrow Li_{3.5}Mg_{0.1}Si$, which is more likely from electrochemical perspective due to slighly lower overall lithiation capacities observed during the discharge for GFM.

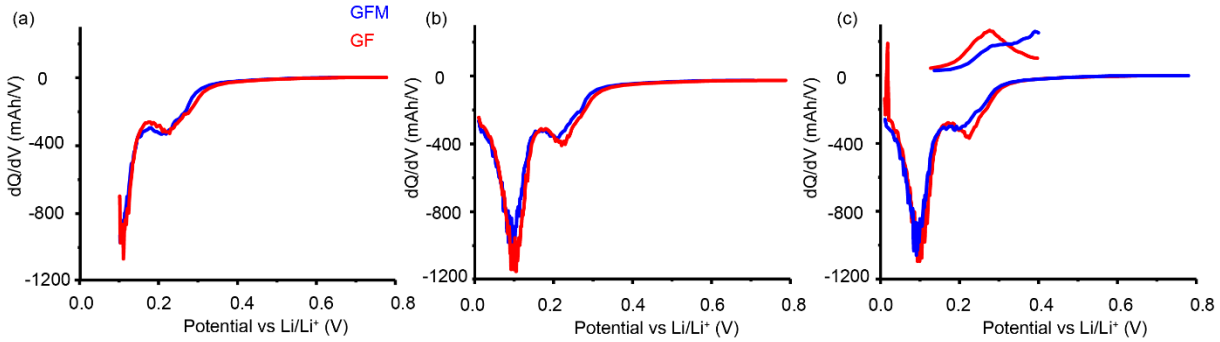

Figure II.1.B.13. Differential capacity vs. voltage plots of GF and GFM at (a) 100 mV, (b) 10 mV upon discharge, and (c) 400 mV upon charge.

The evolution of Li and Si local environments for pure Si anode in two different electrolytes were investigated using electrochemical quartz crystal microbalance (EQCM), ex situ ^{7}Li, and ^{29}Si MAS NMR. Li-Mg-Si ternary phase formation requires large amounts of Li insertion into Si clusters; it could be accumulated by holding the voltage at sufficiently low voltage, such as 10 mV. A more even Li distribution and lower electrochemical hysteresis were promoted by Li-Mg-Si ternary phase formation at the interface. Electrochemistry performance from scale-up pouch cells are consistent with lab-scale coin cells. We propose that upon discharge, Li-Mg-Si ternaries form uniformly, preferably by competition between Li and Mg only at deeply lithiated stages (below 100 mV). Upon charge, Mg remains in the bulk, possibly at a metastable Mg solubility limit in amorphous silicon, forming Li-poor or completely lithium-deficient $Li_xMg_{0.1}Si$ phases and contribute to stable ternary phases in subsequent cycles. The promising potential for scale-up applications examined by pouch cell testing offers more stable passivation at high states of charge in full cells, which should yield to longer calendar life for optimized electrodes.

Conclusions

Thin film, wafer, and nanocrystalline model Zintl phase systems were characterized with STEM, NMR, FTIR, Raman, and SSRM spectroscopies and compared to a Mg-free reference system. For thin films, the role of magnesium was investigated, and it was shown that magnesium (as a coating or in the lattice) formed a binary Mg_2Si interface with the silicon. This material was found to be kinetically slow in lithiating to form a ternary Zintl phase (Li-Mg-Si), although it was detected in the studies. The controlled deposition gave a more uniform distribution and was found to correlate with better electrochemical performance. For the SEI, the samples that had Mg inserted at the interface were found to have much thinner SEI layers that were more resistive. Delithiated electrodes for the two Mg-containing thin film systems as well as the Mg-free system are relatively similar to one another, indicating that Mg returns to electrolyte in both systems. This is consistent with the model that utilizes Mg_2Si in that the mechanism is most likely a kinetically slow ion exchange between Mg and solution lithium cation to gradually form $(Mg_{2-x}Li_{2x})Si$. Measured differences in capacity retention between the two systems suggest that the initial Zintl phase formation mechanism is deterministic for subsequent electrochemical efficiency. Further results on the 500 cycled anode illustrated a large expansion of the Si active material and significant ingress of SEI causing the material fouling. The wafer studies highlighted the role of surface oxide species and the need for defects. In these studies, the intrusion of Mg into the bulk was minimized as the electrochemical activity was found to be low as MgO was observed on the surface of the wafers. In contrast to the near-defect-free SiO_2 rich wafers, the nanocrystalline Si powders showed the highest activity and NMR data were used to identify that the surface of the silicon did not magnesiate until low voltage. In conjunction with the other data shown and previous studies, the mechanism of ternary Zintl phase

formation was identified as an ion exchange reaction between a $Li_{15}Si_4$ charged silicon anode phase and electrolyte-derived Mg cations. The species $Li_{14}MgSi_4$, noted earlier in our TEM and XRD studies, was found to be formed at the surface by an ion exchange reaction. On discharge, the lithium and some of the magnesium are removed, leaving a metastable Mg-containing, Si-rich endmember phase.

Silicon Consortium Project Calendar Aging Electrochemical Screening Protocol

Contributors: Max Schulze (National Renewable Energy Laboratory), Marco Tulio Fonseca Rodrigues (Argonne National Laboratory), Josey McBrayer (Sandia National Laboratory), Ira Bloom (Argonne National Laboratory), Andrew Colclasure (National Renewable Energy Laboratory), Gabriel Veith (Oak Ridge National Laboratory), Daniel Abraham (Argonne National Laboratory), Nathan Neale (National Renewable Energy Laboratory), Anthony Burrell (National Renewable Energy Laboratory), Jack Vaughey (Argonne National Laboratory) and Christopher Johnson (Argonne National Laboratory)

Executive Summary

The purpose of this document is to provide a framework for the development of silicon (Si) electrodes for high-capacity lithium-ion batteries by providing test protocols that researchers and early-stage developers can use to assess the progress of silicon modifications, cell designs, electrolytes, or additives. Overall, whereas full-cell cycling for silicon anodes has progressed significantly over the past several years, similar progress in the area of calendar life remains a major challenge. The procedures detailed in the following sections have been developed out of a major scientific effort, funded by the Vehicle Technologies Office, to understand the formation and evolution of the silicon solid-electrolyte interphase. This first generation of procedures is designed to enable a reasonably well-equipped research laboratory to assess early research progress toward improving calendar aging issues in silicon cells in a reasonable timeframe. These generation-one procedures will be updated, modified, and expanded as the research team obtains feedback from stakeholders and as our understanding of the SEI evolves.

Overview

Traditional approaches to investigate calendar aging often involve experiments that take as long as the period they investigate; the aging inflicted by months of storage is evaluated by exposing the charged cell to controlled conditions for that same number of months. More specifically, such tests age the cells under open-circuit conditions (no current or load applied), with periodic reference performance tests (RPTs) that measure the cell degradation as a function of aging time. The RPTs directly measure the metrics of interest, such as reversible capacity and energy/power retention. Although providing extremely useful information, such approaches are clearly time-consuming and are likely to slow down the development of Si-based cells with robust SEI layers [14].

The testing protocol described in this document is designed to provide semi-quantitative insights on the quality of the SEI in under ~2 weeks. Rather than tracking cell capacity losses over very long times, the protocol presented relies on measuring, in real time, the currents associated with reactions at the SEI as the anode is held at a constant state of charge (SOC). The evolution of these currents over time provides a basis to understand how the state of passivation of the anode evolves over longer time scales. We note that calendar aging is a complex process that involves not only loss of Li^+ inventory, but also active material loss, electrolyte degradation, and power fade. Although the testing protocol being developed by our team will *not* predict all these aspects of calendar aging, it will nonetheless provide information about the rates of Li^+ inventory losses to the SEI, which is a main factor limiting the calendar life of silicon-based anodes.

The testing protocol described herein departs from traditional calendar aging tests in that *it does not provide absolute calendar lifetime predictions*. Instead, the results should be compared against those of standard electrodes like graphite with calendar lifetimes well characterized by other methods. Future versions of this

protocol may provide the ability to quantitatively predict calendar lifetime as the analysis methods are further developed and the lifetime predictions are validated by independent tests. Until such capabilities are available, this protocol can be used to quickly and easily screen electrolyte compositions and silicon electrodes. After this initial investigation, the most promising systems can be studied under more resource-intensive experiments, such as traditional calendar life tests that use long rests with intermittent RPTs.

Calendar Life Screening Protocol

The procedure to test the calendar life of Si anode materials is extremely sensitive to the test cell setup, especially the geometric size and areal capacities of both the test electrode and the counter electrode. Therefore, for reliable comparisons between tests, the testing procedures should adhere to the following requirements:

Cell Design

Table 2: Requirements of Test and Counter Electrodes

Test Anode	Si material	<1.3 mAh/cm^2	15 mm (14 mm vs. Li)
Preferable cathode	Lithium iron phosphate (LFP)	>2.5 mAh/cm^2	14 mm
Acceptable counter electrode	Lithium metal	>2.5 mAh/cm^2	15 mm

Size 2032 stainless steel coin cells are used as the electrochemical test vehicle. The electrodes consist of the Si anode material (the test electrode) against a thick high-capacity lithium iron phosphate (LFP) cathode. When an LFP electrode of sufficiently high areal capacity is not available, a Li counter electrode can be used instead; we warn that the chemical reactivity of lithium can alter the electrolyte composition and can affect the generality of observations obtained for some systems. The diameters are 14 mm for the cathode (LFP) when it is paired with the 15-mm-diameter Si-containing test anode. When the Si-containing electrode is paired with a Li counter electrode, the Si electrode has a 14-mm diameter with a 15-mm-diameter Li foil (less than 1-mm thick).

The areal capacities of the electrodes are chosen to ensure that there is enough Li^+ inventory to supply the Si-containing test electrode with capacity during the aging protocol. The LFP electrode is greater than or equal to 2.5 mAh/cm^2, whereas the Si-containing test electrode is less than or equal to 1.3 mAh/cm^2 at the SOC at which aging will be assessed. This additional Li^+ inventory is meant to guarantee that the cathode would still retain excess capacity even after the large irreversibility that is typical of Si electrodes in the first few cycles. If electrodes with loadings other than those designated are used, it is imperative that the total utilized capacity of the Si electrode (reversible capacity + accumulated irreversible capacity) not exceed the capacity of the counter electrode during the test. This design ensures that the counter electrode can effectively supply the Li^+ needed to (re)form the SEI at the Si test electrode.

Cell Assembly

The 2032 stainless steel coin cell is built following an assembly process that has been well established at Argonne National Laboratory [5]:

1. Electrodes should be dried under dynamic vacuum for at least 14 h at 120°C for polyvinylidene fluoride (PVDF) binder (LFP cathode) containing electrodes, and 150°C for polyacrylic acid (PAA) or LiPAA

binder-containing electrodes. Other binders that are used should be dried appropriately so as not to affect the cell chemistry.

2.

a. Note that thick single-sided LFP electrodes can curl when wet with the electrolyte. Thus, we recommend assembling LFP-containing cells from the anode side up in the following order: cell cap with attached polypropylene gasket, 0.5-mm-thick stainless steel spacer, 15-mm Si test electrode, 20-µL electrolyte, 19-mm diameter layer of 2325 Celgard separator or equivalent, 20-µL electrolyte, 14-mm LFP counter electrode, 0.5-mm-thick stainless steel spacer, stainless steel wave spring, and cell case.

b. Li half-cells should be assembled in the following order: cell case, 14-mm Si test electrode, 20-µL electrolyte, 19-mm diameter separator layer, polypropylene gasket (oriented to properly mate with cell cap), 20-µL electrolyte, 15-mm-diameter Li metal foil (<1 mm thick), 0.5-mm-thick stainless steel spacer, stainless steel wave spring, and cell cap.

3. The assembled cell stack should then be crimped together with a hydraulic crimper, preferably an automatic crimper for consistency.

Electrochemical Protocol

C-rate determination: The C-rate is defined as the current necessary to drive the Si test electrode from one voltage cutoff to the other in 1 hour (a C/10 rate takes 10 hours to drive the electrode from one voltage cutoff to the other). This value should be determined using half-cell data of the second cycle of the Si test electrode. Because the LFP electrode delithiates at ~3.45 V vs. Li/Li^+ and relithiates at ~3.40 V vs. Li/Li^+, the cutoff potentials correlate as follows:

2.7 V vs. LFP (discharge) = 0.7 V vs. Li/Li^+

3.35 V vs. LFP (charge) = 0.1 V vs. Li/Li^+

LFP full-cell:

1. Rest cell at OCV for 4 hours to allow electrolyte wetting
2. At a C/10 rate, charge to 3.35 V, discharge to 2.7 V, repeat 3 times, data acquisition should be $\Delta V = 5$ mV
3. Hold cell at 2.7 V until $i < C/100$ to fully lithiate test electrode, data acquisition should be $\Delta t = 1$ min, $\Delta i = 10$ µA./10 rate, data acquisition should be $\Delta V = 5$ mV
4. Hold potential at 3.35 V for 180 hours, data acquisition should be $\Delta t = 1$ min, $\Delta i = 10$ µA
5. Discharge to 2.7 V at a C/10 rate, data acquisition should be $\Delta V = 5$ mV
6. Hold cell at 2.7 V until $i < C/100$ to fully lithiate test electrode, data acquisition should be $\Delta t = 1$ min, $\Delta i = 10$ µA
7. At a C/10 rate, charge to 3.35 V, discharge to 2.7 V, repeat 2 times, data acquisition should be $\Delta V = 5$ mV.

Li half-cell (same procedure as LFP full-cell with potential cutoffs substituted as follows):

- 0.1 V instead of 3.35 V

- 0.7 V instead of 2.7 V.

The preliminary efforts described in this report are limited to studying SEI passivation at the SOC achieved by the anode at ~0.1 V vs. Li/Li$^+$; for a graphite electrode, this would correspond to ~55% of lithiation. Most Si-based electrodes can remain mechanically stable when cycled to this potential, and thus permanent losses of active material are less likely to occur during the tests discussed here. Our team recognizes that SOC is an important variable when investigating calendar aging and modeling SEI growth [16], and future studies will expand the scope of this report.

Data Collection and Presentation

Verifying the current response of the cell during the voltage hold is critical to guarantee that the data analysis will be meaningful. Figure II.1.B.14 shows the current measured during the hold, normalized to the capacity (lithiation capacity measured during the charge immediately before the voltage hold) of a test silicon electrode and a graphite baseline electrode. The expected behavior for the current measured in both systems are shown in Figure II.1.B.14a, where the continuous decay exhibited by the traces indicates that the counter electrode is supplying sufficient Li$^+$ inventory. This plot also qualitatively demonstrates that the currents that arise from parasitic reactions on the graphite electrode, seen long after the initial decay, are roughly an order of magnitude smaller than those observed for the silicon, demonstrating its better passivating behavior and longer calendar lifetimes, as expected. The results displayed in this type of plot should serve as a gate to determine if further analysis should be performed using the testing protocols described in this document. *If the residual current (i) does not approach that of a baseline electrode such as graphite (necessarily within an order of magnitude), then further analysis is not warranted, as the SEI is clearly not sufficiently stable*. It is recommended that the data acquisition parameters discussed in the previous section are used in the voltage hold test to ensure enough resolution.

A major pitfall of this experimental protocol occurs when the Li$^+$ inventory of a test cell is exhausted (counter electrode is completely delithiated). The sudden decline of the current responses to diminishingly small and indistinguishable values as seen in Figure II.1.B.14b (after ~40 h of voltage hold) indicates that the Li$^+$ inventory supplied by the counter electrodes has been exhausted during the voltage hold. Under these conditions, the external current no longer provides a direct measure of the rate of parasitic reactions, yielding inaccurate information about the electrode's calendar lifetime. This is another critical reason why the current response of the collected data needs to be evaluated before performing the analysis described in the next section. If the current response displays a similar behavior to that shown in Figure II.1.B.14b, the test cell should be remade with a higher-capacity counter electrode or a lower-capacity test electrode.

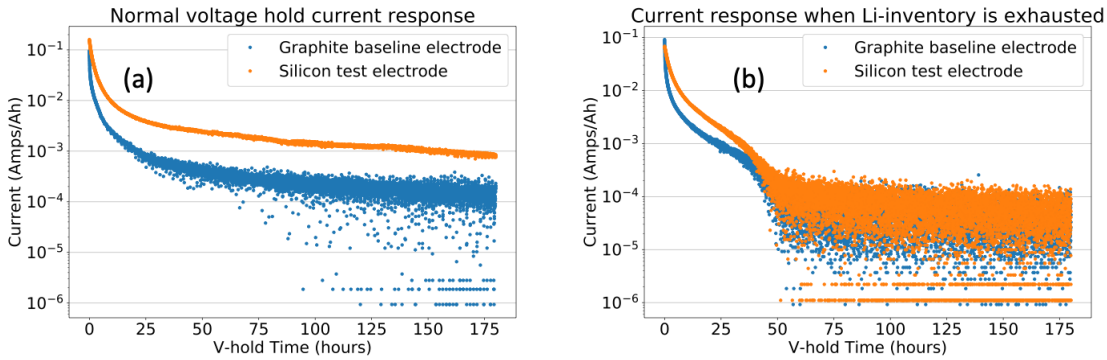

Figure II.1.B.14. Current decay versus time during voltage holds of (blue) graphite baseline anode and (orange) 80 wt % Si test anode. The current has been normalized to the capacity of the test electrode measured during the lithiation immediately before the voltage hold. Panel (a) shows the current response where there is an excess of Li$^+$ inventory supplied by a counter electrode with a flat voltage profile, as is the scenario marked (a) in Figure 3. Panel (b) shows how the current suddenly declines as the Li$^+$ inventory supplied by the counter electrode is exhausted, polarizing the electrodes

to high potentials. Under these conditions, the measured current underestimates the actual rate of parasitic reactions experienced by the test electrode.

Data Analysis and Result Reporting

Analysis of the data should first be done by qualitative visual inspection and comparison between the test electrodes and a baseline electrode. Figure II.1.B.15 shows the current decays of three different Si test electrodes and a graphite baseline electrode. The normalization of the current data to the reversible capacity of each electrode is important because the resulting units of amps/Ah indicate the rate at which each electrode is losing reversible capacity due to Li^+ consumption at the SEI. If the normalized current measured from a Si test electrode at the end of the 180-hour voltage hold is distinguishably higher than the baseline electrode, further analysis is not needed, as the electrode's SEI is clearly not sufficiently stable. This is the case for each of the Si test electrodes shown in Figure II.1.B.15, thus showing the effectiveness of this simple qualitative comparison for the initial screening of Si test electrodes.

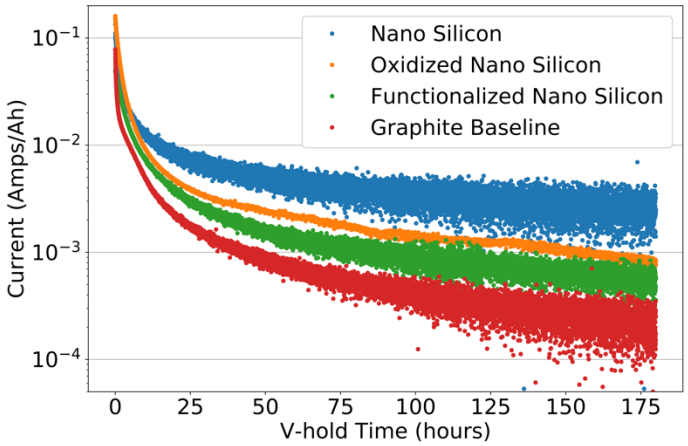

Figure II.1.B.15. Current decay versus time during voltage holds of several different Si test electrodes and a graphite baseline electrode. The rate of parasitic reactions of the Si test electrodes can be qualitatively distinguished by visual inspection, and all exhibit greater aging rates than the graphite baseline electrode.

The average current after 180 hours of voltage hold can be used as a metric to rank the rate of parasitic reactions at each electrode, reported in this section for the examples shown in Figure II.1.B.15. This information should be complemented by details about electrode composition, areal capacity, and electrolyte used in the tests. Additionally, because there can be variability between tests for a given electrode and electrolyte pair, we recommend that a sample size of at least three test cells for each test electrode type be reported.

Example reporting:

Graphite baseline electrode

1.17 mAh/cm^2

91.83 wt % Superior Graphite SLC1520P

2 wt % Timcal C45 carbon

6 wt % Kureha 9300 PVDF binder

0.17 wt % oxalic acid

Electrolyte: 1.2 M $LiPF_6$ in ethylene-carbonate:ethyl-methyl-carbonate 3:7 + 10 wt % FEC

Mean terminal current = 0.023 mA/Ah

Nano Silicon

0.3 mAh/cm^2

20 wt % 3.9-nm-diameter Si nanoparticles

65 wt % Timcal C65 carbon

15 wt % PAA binder

Electrolyte: 1.2 M $LiPF_6$ in ethylene-carbonate:ethyl-methyl-carbonate 3:7 + 10 wt % FEC

Mean terminal current = 0.262 mA/Ah

Oxidized Nano Silicon

1.24 mAh/cm^2

80 wt % surface-oxidized 150-nm-diameter Si nanoparticles

10 wt % Timcal C45 carbon

10 wt % LiPAA binder

Electrolyte: 1.2 M $LiPF_6$ in ethylene-carbonate:ethyl-methyl-carbonate 3:7 + 10 wt % FEC

Mean terminal current = 0.092 mA/Ah

Functionalized Nano Silicon

0.7 mAh/cm^2

40 wt % 4-phenylphenol surface-functionalized 30-nm-diameter Si nanoparticles

40 wt % Timcal C65 carbon

20 wt % PAA binder

Electrolyte: 1.2 M $LiPF_6$ in ethylene-carbonate:ethyl-methyl-carbonate 3:7 + 10 wt % FEC

Mean terminal current = 0.059 mA/Ah

These examples highlight the capabilities of the screening protocol described in the current version of this document. Because it is currently limited to qualitative analysis, it is especially important to use a baseline electrode with a calendar life well-characterized by other methods under the conditions of interest. Future versions of this report may include a semi-quantitative model to describe the rate of parasitic reactions in the electrodes of interest, which is currently under validation by long-term experiments; this model is outlined in general terms at the end of the discussion section.

Discussion

Our methodology is based on using voltage holds to measure the rate of Li^+ trapping at the SEI in Si-containing cells. This approach has the advantage of recording real-time rates of side reactions, providing information about the time dependence of such processes and potentially enabling extrapolation of behaviors observed in relatively short-duration experiments. Its working principle is based on the fact that parasitic reduction reactions (such as the ones involved in SEI formation) effectively consume electrons from the anode,

which decreases the anode SOC. The instantaneous voltage of a cell is the difference between the potentials of the positive and negative electrodes, so a change in the anode SOC yields a change in cell voltage. If the anode SOC is "pinned" by holding the cell voltage constant, electrons must flow from the cathode to the anode to replenish the charge consumed by side reactions in order to keep the anode SOC invariant (i.e., the current flowing through the cell and measured by an external circuit is equal to the rate of these parasitic processes). This ideal equivalence between the parasitic and measured currents is achieved when the anode has a sloped potential and is most sensitive to SOC and the cathode is insensitive to SOC (the voltage profile is "flat"). We can approximate these conditions by using $LiFePO_4$ (LFP) as a cathode (which can provide most of its capacity while at ~3.45 V vs. Li/Li^+), and by performing the voltage hold at potentials in which the anode cycling profiles are notably sloped to maximize sensitivity.

For these tests, it is important that the LFP counter-electrode has a capacity in excess of that used by the reversible and irreversible reactions occurring at the Si test electrode. The importance of this condition is demonstrated by the simulated voltage profiles shown in Figure II.1.B.16, where the LFP voltage profiles are shown in blue. Profiles for pristine (solid line) and aged (dashed line) Si anodes are displayed in black with the corresponding full-cell voltage profiles displayed in red. The intersecting lines marked (a) in Figure II.1.B.16 represent the pristine full-cell being held at 3.35 V, where the potential at the pristine Si anode would be roughly equivalent to ~100 mV vs. Li/Li^+. In this pristine cell at 3.35 V, the LFP voltage profile is insensitive to SOC (voltage profile is flat), and thus any changes of the Si SOC would require a change in cell voltage (i.e., the Si SOC is "pinned"). As electrons and Li-ions are consumed at the Si electrode during aging, they are replenished by the LFP cathode, as additional Li^+ extraction is possible at that same electrode potential. Nevertheless, if enough capacity is lost, the aged cell may no longer be able to keep the Si SOC constant. This Li^+ inventory exhaustion scenario is represented by the intersecting lines marked (b) in Figure II.1.B.16, where the aged cell is still held at 3.35 V. In the aged cell with an exhausted Li^+ inventory, the LFP voltage profile is polarized above its plateau potential and is sensitive to SOC (highly sloped), resulting in the Si electrode no longer being held at the desired potential of 100 mV vs. Li/Li^+. When that happens, additional Li^+ extraction from LFP to counter parasitic reactions at the anode would cause an increase in the potential of both electrodes; this would involve a net decrease in anode SOC, and thus the currents measured by an external circuit would underestimate the extent of side reactions in the cell.

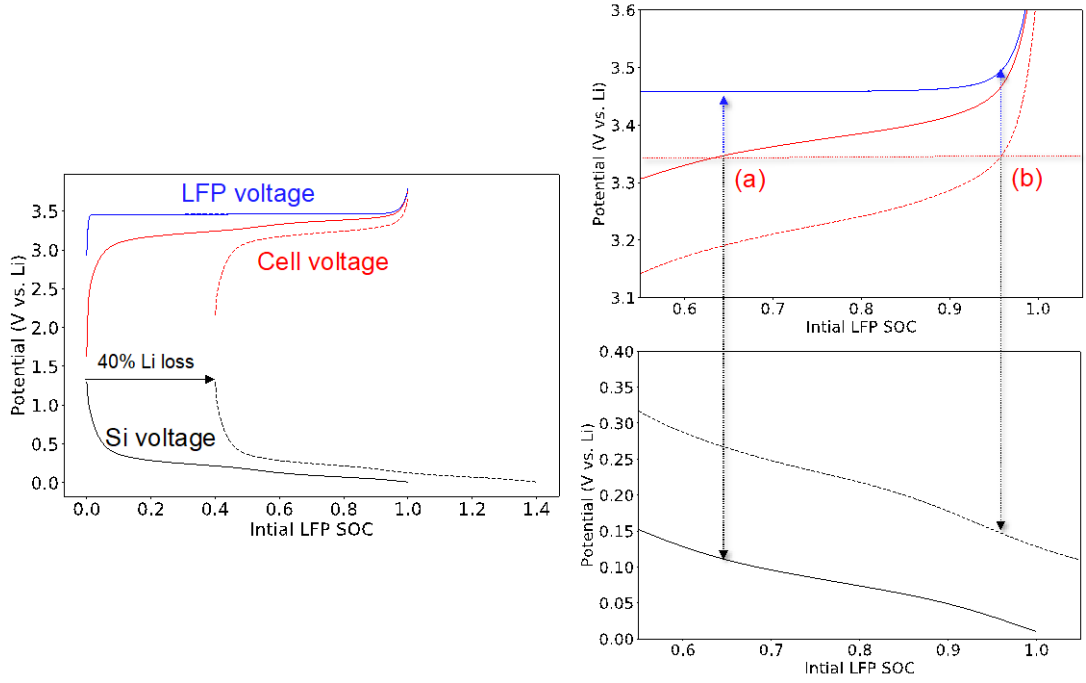

Figure II.1.B.16. (left) Simulated voltage profiles for an LFP cathode (blue), Si anode (black), and the two-electrode cell combining those two electrodes (red). The dashed black line represents Si electrode aging by the loss of Li^+ inventory, which effectively shifts the Si voltage profile relative to the LFP voltage profile and results in the aged cell having the dashed red voltage profile. (right) Zoomed-in portions of the voltage profiles where the dotted horizontal red line represents a voltage hold potential of 3.35 V for pristine (a) and aged (b) Si electrode-containing cells.

The use of LFP as a counter-electrode has additional advantages. One is that the cathode can be assumed to be an essentially inert electrode, because its low potentials will lead to little changes in electrolyte composition and are unlikely to generate oxidative currents that could affect the analysis. Additionally, the extremely flat voltage plateau of LFP over its entire capacity range allows it to be used as a reliable pseudo-reference electrode in a two-electrode coin cell. Thus, the absolute potential of the anode can be well controlled, facilitating studies on the effect of SOC on passivation. The test protocol specifics and an example voltage profile are shown in Figure II.1.B.17, where a 180-hour-long voltage hold is preceded by three formation cycles and followed by two additional diagnostic cycles. The total test time is ~290 hours (less than two weeks).

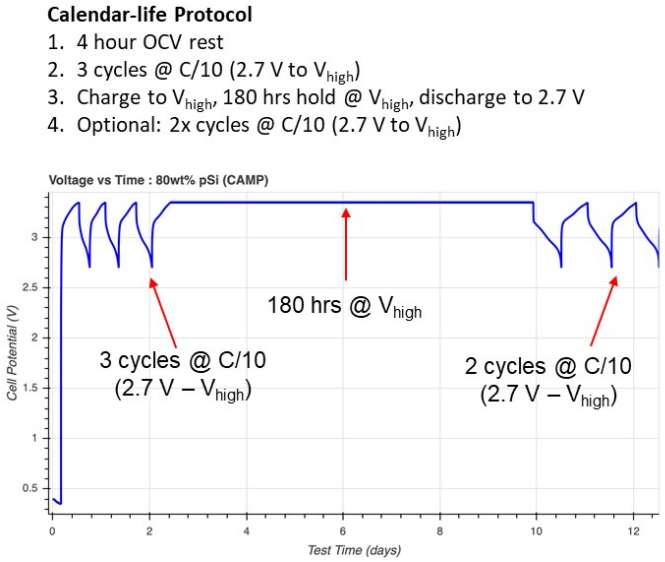

Figure II.1.B.17. The test protocol to estimate the rate of parasitic reactions of Si-based electrodes. The example voltage profile is from a cell coupling an 80% Si electrode vs. an LFP cathode.

Although this experimental approach is a logical pathway to derive information about electrode passivation from short-term tests, it also presents challenges. In practice, electrodes present a finite impedance, and lithiation processes are incomplete by the time the voltage hold initiates. Hence, the current measured during the early periods of voltage hold is a combination of reversible lithiation processes (lithiation of Si) and irreversible electrochemical reactions (SEI formation and concomitant Li^+ consumption). As the voltage is held for longer and longer times, the proportion of the current driving reversible reactions diminishes relative to the current driving the irreversible reactions, and the measured current becomes a more reliable descriptor of parasitic processes. For these component contributors, *the challenge exists to validate that the analyses can differentiate between both these contributions to the measured current*. The reversible capacity passed during the voltage hold can be experimentally quantified by inspecting cell discharge after the hold, and these values are used to help differentiate the time-dependent contributions from the reversible and irreversible processes.

The purpose of the 180-hour-long voltage hold is to determine the rate of Li^+ inventory consumption, as measured by the current, due to irreversible side reactions at the anode surface. Using this method, the current measured during the voltage hold is due to a combination of the reversible lithiation reactions and the

irreversible side reactions. Figure II.1.B.14a shows the typical current responses during the voltage hold of example electrodes. The current densities decrease more than an order of magnitude during the first ~20 hours of the voltage hold as the reversible lithiation reactions near completion. In contrast, toward the end of the voltage hold, the current densities stabilize at diminishingly small values that are primarily due to irreversible Li^+-consuming reactions. The lower current density of the graphite electrode at the end of the voltage hold compared to the Si electrode is good confirmation that the measurement is qualitatively capturing the expectedly better SEI stability (and lower Li^+ inventory consumption rate) of the graphite electrode. Figure II.1.B.14b shows the current response during the voltage hold where the Li^+ inventory of the cell becomes exhausted. This occurs when the cathode is unable to supply additional electrons and Li ions to keep the anode pinned at a fixed SOC, as outlined by marker (b) in Figure II.1.B.16. In this case, the full cell is maintained at a fixed voltage with a net decrease in anode SOC, resulting in the measured currents underestimating the parasitic reaction rates. This can be seen in Figure II.1.B.14b by the sudden decrease in current to vanishingly small values, and highlights the importance of performing these experiments in cells with excess counter-electrode capacity.

Integrating the measured current over time during the voltage hold and normalizing to the electrode's reversible capacity yields time-dependent capacity, $Q_{hold}(t)$. In order to deconvolute the irreversible and reversible contributions to the capacity, the following function can be fit to the normalized capacity data:

$$Q_{hold}(t) = Q_{irrev}(t) + Q_{rev}(t)$$

The numerical forms of these functions are still being determined using long-term voltage hold validation experiments. As the validation data become available, future versions of this report may include numerical models that can be used to semi-quantitatively describe the rate of SEI-related side reactions. Preliminary results suggest that $Q_{rev}(t)$ has an asymptotic time dependency as the reversible capacity approaches a maximum value at long times, whereas $Q_{irrev}(t)$ may be proportional to the square root of time. The square root of time dependency of $Q_{irrev}(t)$ is well supported by empirical observations in the literature, and is believed to capture the general behavior of SEI growth [16,17] This particular functional form arises from the hypothesis that the irreversible side reactions occurring at the electrode surface due to SEI formation are diffusion-limited, and thus their rates are inversely proportional to the square root of time.

Notwithstanding, the Si SEI stability will naturally fluctuate as a function of a plethora of internal and external factors. The present report is just the beginning of an exploration of the Si calendar life behavior embedded in a current response, the measurement probe of choice. In an electrochemical process, electrode kinetics and their reaction rates are tied to a current value. The parasitic reactions in Si electrodes are exceedingly complex and, as a first pass, it is affiliated with (1) the Li-ion conductivity in the SEI, (2) the mechanical stability of SEI, (3) chemical stability (solubility) of the SEI, and (4) the electronic conductivity within the SEI. What factors dominate thus begs the question: How can one slow down this degradation phenomena and create "immunity"?

Conclusions

A method to qualitatively compare the calendar aging rates of silicon anodes has been developed using full cells with an excess amount of electrolyte and of Li^+ supplied by an LFP counter electrode. After formation cycles, the voltage of a test cell is held for 180 h, and the current response measured during the voltage hold can be used to qualitatively compare the rates of Li^+ consumption at the SEI of silicon test electrodes to a baseline electrode. Long-term voltage hold aging experiments are underway to determine numerical models that can be used to derive aging parameters for silicon test electrodes. Once the numerical models developed by our team are fully validated, they can be used to support developments of cell, material, and interfacial designs that minimize calendar aging rates of Si electrodes.

Understanding Silicon Alloy Effects on the SEI

Contributors: Elisabetta Arca, Insun Yoon, Terri Lin, Kang Yao,Hetal Patel, Eric Sivonxay, Wei Tong, Kristin Persson, Robert Kostecki (LBNL), Greg Pach, Fernando Urias, Andrew Norman, Nathan Neale (NREL)

Background

Si has garnered tremendous interest as a replacement for graphite in lithium-ion battery technology due to its potential to enable lighter-weight and lower-cost battery packs for large-scale applications such as electric vehicles and grid-scale storage. Si is primarily attractive due to its large capacity (4,200 mAh/g, which is 10 times higher than graphite) and low market price. However, commercial devices with high Si content are limited by the following pitfalls: (1) Si undergoes significant structural reconstruction and volume change during charge/discharge. This results in substantial strain within the material and leads to the propagation of cracks and material loss, resulting in a rapid capacity fade. (2) The Si–electrolyte interface is unstable during electrochemical cycling. SEI that consists of various electrolyte decomposition products does not fully passivate the Si surface. Consequently, electrolyte and the lithium inventory are consumed continuously, and this results in poor calendar life. To date, only a limited fraction of Si (~15 wt %) has been incorporated in graphite anodes to increase the energy density without sacrificing the lifetime. Significant efforts must be made to achieve further improvements.

This project's objective is to overcome the Si anode issues, such as intrinsic non-passivating surface and low electrical conductivity. Our approach to achieving the goals is to develop Si-based metallic alloys with surface properties favorable to form a stable SEI, improved kinetic properties, and conductivity.

A combination of four experimental techniques and computational techniques are adopted to develop practical Si-based metallic alloys: (1) magnetron (co-)sputtering reliably produces thin-film-type amorphous Si-Sn electrodes; (2) nonthermal plasma-enhanced chemical vapor deposition (PECVD) provides a unique pathway for metastable material synthesis, such as Si-Sn alloys, in the form of nanoparticles (NPs); (3) splat quenching enables rapid quenching of a Si-based metal alloy molt to form amorphous metallic glasses by preventing long-range reorganization of the atoms; and (4) density functional theory and ab initio molecular dynamics simulations are well suited for predicting proper Si alloy compositions among numerous combinations, thus effectively guiding the time-intensive experimental efforts.

Incorporation of Sn in Si-based anode is expected to improve the electrode conductivity and may help the formation of a stable SEI layer while maintaining the high specific capacity. Furthermore, the group IV alloys can allow us to study more fundamental material properties such as the effect of NP strain caused by the larger size of Sn atoms relative to Si during lithiation and delithiation. Being free of binder and carbon additive, the Si-Sn thin-film electrodes formed by sputtering are devoted to investigating Si-Sn alloy's interfacial properties. The results reveal that Si-Sn shows stable long-term cycling and dramatically different morphology/composition compared to the pure Si counterpart. Si-Sn NPs synthesized by PECVD are constructed into composite electrodes to investigate the electrochemical characteristics and cycling performance. The effort is conducted toward these ends that achieved the Go/No-Go Q2 FY 2020 Milestone: "Production of tin-silicon alloys to be determined by the ability of the alloys to be prepared in 1-g quantities and a demonstration that the alloys exhibit greater cyclic life than the pure metals alone."

Silicon Metallic Glasses (Si-MG) is an attractive category of materials for lithium-ion batteries due to its homogeneously distributed Si content at an atomic level, which can eliminate the two-phase coexistence and materials pulverization during electrochemical cycling through solid-solution alloying. Thus, in comparison to polycrystalline intermetallic compounds, they present the advantage of lacking phase boundaries. Multicomponent Si-MGs can also provide a pathway to address the major issues associated with Si-based

electrodes by carefully selecting the elements to be introduced. First, a proper choice of Li-inert element can become a buffer or reduce the magnitude of volume change during Li alloying/dealloying, which is the source of electrode-scale mechanical instability. Second, the use of elements that favor the formation of stable SEI (e.g., Ni) may tune the SEI on Si-MG to achieve full passivation. We have successfully developed a Si-MG ($Al_{64}Si_{25}Mn_{11}$ at. %) using a splat quenching system. The investigation carried out to date shows that $Al_{64}Si_{25}Mn_{11}$ glass is electrochemically active and forms a stable SEI, unlike elemental Si. Insights from this study provide properties desired in an SEI interface and can guide future SEI design rules for Si-based anodes.

Although the experimental approaches are attempted on plausible Si-based alloy combinations, there are nearly infinite variations on elements and stoichiometry of the potential binary and ternary Si-based alloys. High-throughput computational studies are uniquely suited for such a combinatorial problem. As such, we use density functional theory and ab initio molecular dynamics to conduct a high-throughput study of the lithiation behavior of a large subset of these binary and ternary Si alloys, investigating the structural changes and lithiation potential of these alloys. The outcomes from the computational studies are expected to help selectively choose Si alloy composition and ratio with high practicality.

Investigation on Si-Sn Thin-Film Model Electrodes Prepared by Magnetron Sputtering

As previously reported, the Si_xSn_{1-x} composite thin films were directly deposited onto Cu foils by co-sputtering separated Si and Sn targets simultaneously, with the film composition tuned by controlling the deposition power level. All the as-deposited films were subsequently stored under vacuum to prevent air exposure. 2032-type coin cells were assembled using the as-produced films (1.6 cm^2) directly as the working electrodes, Li metal foil as the counter electrode, and 1.2 M $LiPF_6$ in ethylene carbonate-ethyl methyl carbonate (3:7 by weight) as the electrolyte (Gen2). For electrochemical cycling test, the cells were galvanostatically discharged and charged between 1.5 and 0.01 V at C/20 based on the experimental capacity. For scanning electron microscopy (SEM) and EDS, the cells were galvanostatically cycled between 0.01 and 1.5 V at C/20 at selected cycles. The cycled electrodes were harvested by opening the cells, rinsing with dimethyl carbonate, and natural drying inside an Ar-filled glovebox. The electrode samples were quickly transferred to the SEM chamber for morphological and compositional studies.

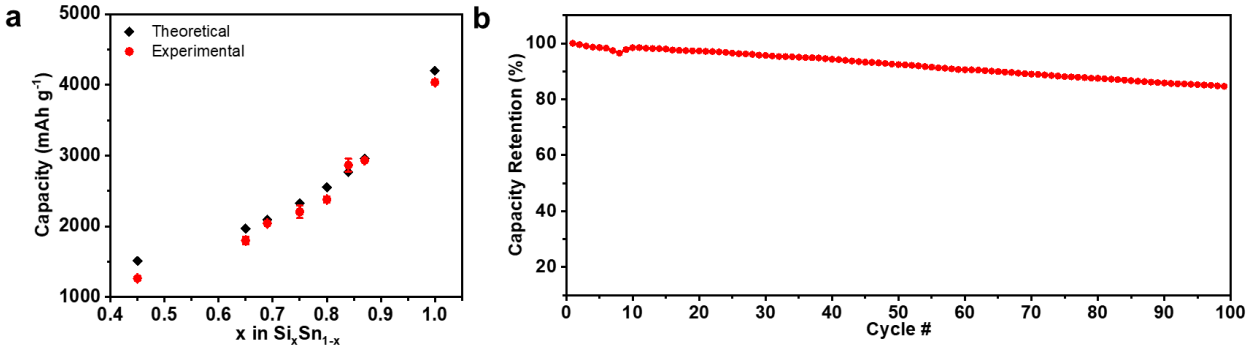

Figure II.1.B.18. (a) Theoretical and experimental capacities of Si_xSn_{1-x} ($0.45 \leq x \leq 1$) films during the first lithiation. (b) Long-term cycle performance of an optimal Si_xSn_{1-x} thin film (x = 0.8).

The specific capacities of Si_xSn_{1-x} ($0.45 \leq x \leq 1$) during initial lithiation are estimated based on the measured film thickness and theoretical densities of Si and Sn. The theoretical and estimated capacities during the first lithiation are plotted in Figure II.1.B.18a. It can be seen that the films with $x \geq 0.69$ all attain a high capacity of over 2,000 mAh g^{-1}. The largest gap between the theoretical and experimental values is found for the film of x = 0.45. This may be attributed to the inhomogeneous Li insertion occurring in the crystalline film (as previously revealed by X-ray diffraction), leading to the incomplete lithiation reaction. The capacities of the other X-ray amorphous films ($x \geq 0.65$) exhibit a capacity close to their theoretical values, independent of composition. It can be inferred that the amorphous nature is beneficial to more complete reactions (i.e., a higher utilization of the active material).

Although the cycling stability can be achieved by controlling the cyclable capacity of Si anode, we demonstrate that the Si-Sn composite film can cycle well in the long term at the optimal compositions, while

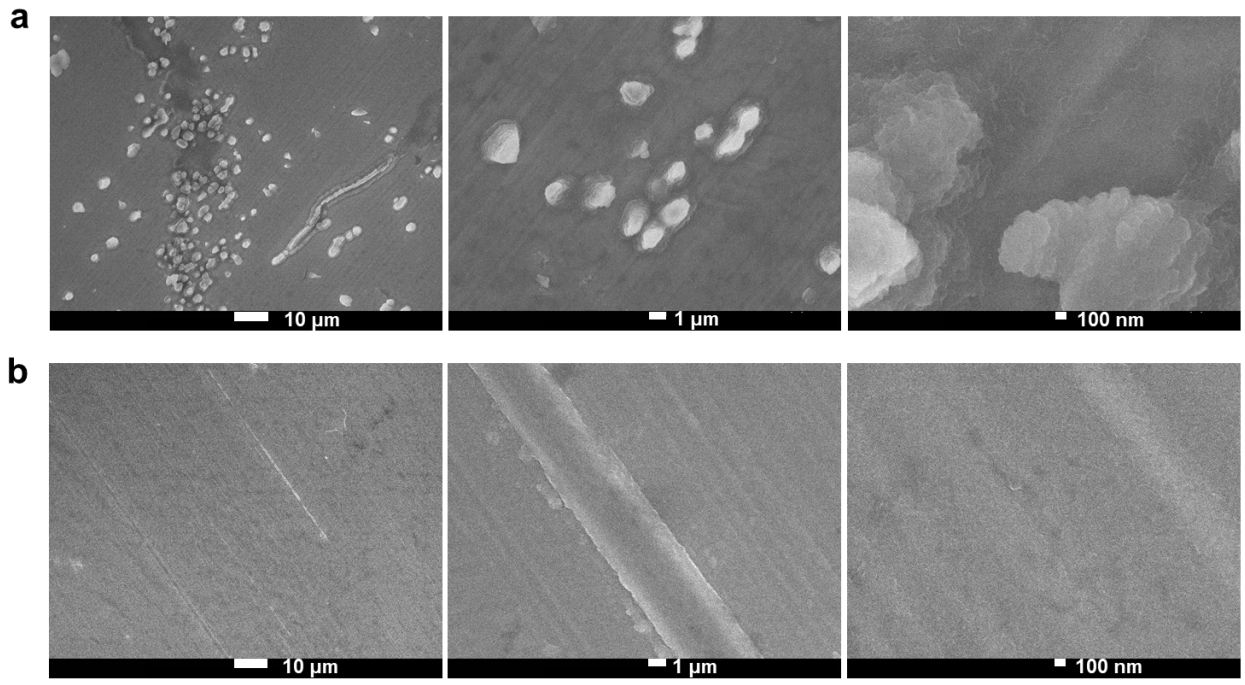

Figure II.1.B.19. Representative SEM images of (a) Si and (b) Si-Sn films after the first lithiation.

approaching nearly full lithiation. As shown in Figure II.1.B.18b, the Si-Sn film of x = 0.8 is capable of retaining 84% of its initial capacity after 100 cycles, corresponding to an average capacity loss of around 0.17% per cycle. It is worth noting that the excellent cycling of amorphous Si-Sn film is obtained without the use of any binder, carbon, or electrolyte additive.

Figure II.1.B.19 shows the SEM images of the Si and Si-Sn films after the first lithiation. As shown in Figure II.1.B.19a, after the initial lithiation of the Si film, scattered islands up to a few micrometers are clearly visible on the electrode surface, some of which are connected to form continuous structures. In stark contrast, the initially lithiated Si-Sn film displays a uniform morphology without the presence of such peculiar structures

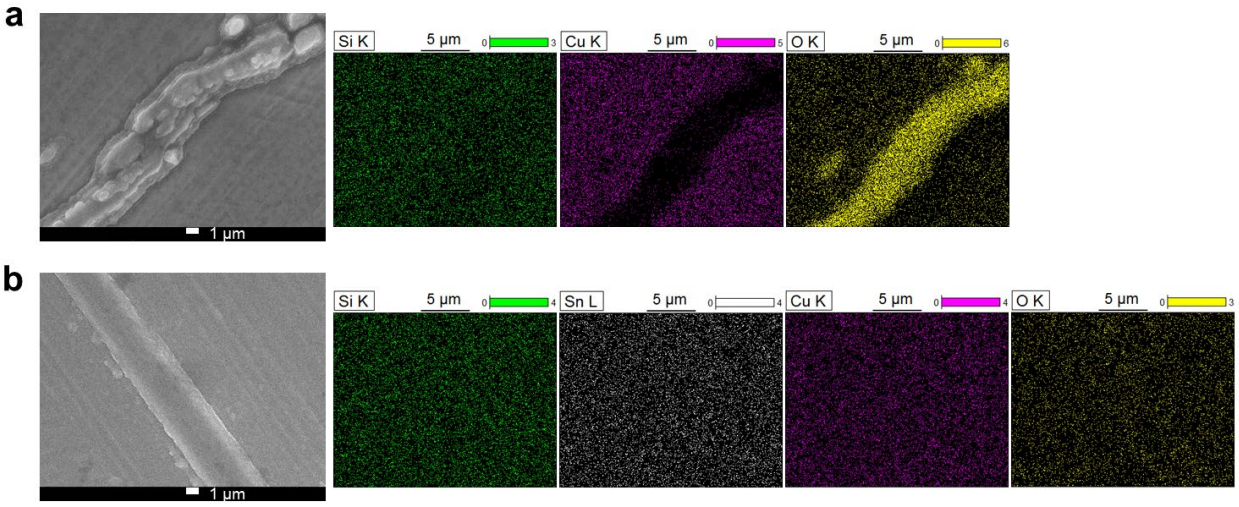

Figure 3. EDS mapping of (a) Si and (b) Si-Sn films after the first lithiation.

(Figure II.1.B.19b). Note the stripping feature in Figure 2b originates from the Cu substrate. The EDS mapping of the island morphologies on the lithiated Si (Figure II.1.B.20a) reveals they are rich in O, whereas the Si-Sn film (Figure II.1.B.20b) shows uniform elemental distribution without any sign of O-enriched heterogeneity. This suggests the dramatically different SEI surface layer on the lithiated Si and Si-Sn thin film electrodes. Note that no FEC was used throughout the study to investigate the intrinsic SEI properties of Si anode in Gen 2 carbonate electrolyte.

The elemental distribution on the Si and Si-Sn films at pristine state and after the first charge (lithiation) and first, second and fifth discharge (lithiation) are plotted in Figure II.1.B.21. For both samples, a drastic increase in O content is observed upon the first lithiation, likely due to the electrolyte decomposition and SEI formation. Moreover, the O content for the lithiated Si is almost double compared to that for the lithiated Si-Sn film. Upon the first delithiation, the O level decreases for both films, indicating the possible dissolution or decomposition of some SEI components (resulting in O loss) upon delithiation. The O content remains low for Si and Si-Sn electrodes after the second and fifth delithiation, but still higher than their pristine states (Table 3). Such phenomena regarding the change of the O content upon initial lithiation/delithiation and distinct morphologies between the Si and Si-Sn, along with their different electrochemical performance, deserve further in-depth investigation.

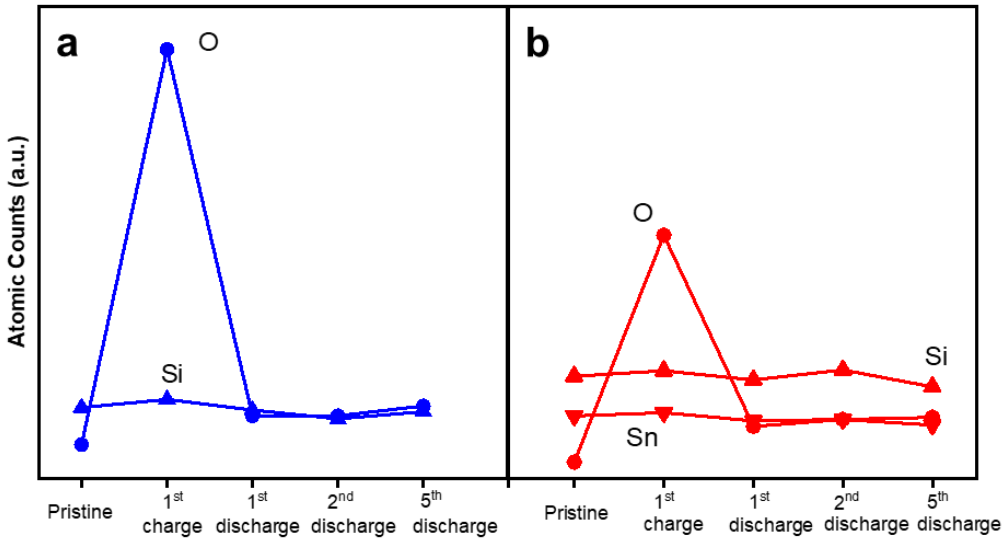

Figure 4. Elemental distribution on (a) Si and (b) Si-Sn films at pristine state and after the first charge (lithiation) and first, second, and fifth discharge (delithiation).

Table 3: Elemental Composition of Si and Si-Sn Films at Pristine State and After the 1st Lithiation and 1st, 2nd, and 5th Delithiation.[a]

State of Charge	Si film (V)		Si-Sn film (V)		
	Si	O	Si	Sn	O
Pristine	0.20	0.09	0.28	0.17	0.04
1st lithiation	0.22	1.18	0.30	0.18	0.67
1st delithiation	0.19	0.17	0.27	0.16	0.14
2nd delithiation	0.16	0.17	0.30	0.16	0.16

5th delithiation	0.18	0.20	0.25	0.15	0.17

[a]All elements normalized to Cu

Investigation on Si-Sn Nanoparticle Model Electrodes Prepared by PECVD

We have demonstrated the incorporation of small amounts <10 at. % of Sn into Si-Sn alloy NPs using the nonthermal PECVD approach. Tin incorporation is confirmed using a suite of chemical and structural characterization techniques, including diffuse reflectance infrared Fourier transform spectroscopy (DRIFTS), XRD, TEM, and EDS mapping. We have also incorporated these materials in composite lithium-ion battery anodes and studied their cycling performance in a half-cell architecture for >100 cycles.

The nonthermal plasma synthesis process for the production and characterization of Si-Sn alloy NPs is described in our Q2 FY 2020 report. Here, we reproduce Figure II.1.B.22 from our Q2 report, which shows the DRIFTS spectra and XRD patterns from three different NP samples: pure intrinsic Si, 5 at. % Sn ($Si_{0.95}Sn_{0.05}$), and 10 at. % Sn ($Si_{0.9}Sn_{0.1}$). The absorption feature at 1,790 cm^{-1} is attributed to *SnH_x stretching vibrations, where the * denotes a surface Sn atom, and is noticeably absent in the pure Si NP sample. Additionally, the *SiH_x stretching region (2,000–2,200 cm^{-1}) for the alloyed NPs becomes less well-defined with a broader peak that has a maximum intensity at higher energies and a lower energy tail extending below 2,000 cm^{-1}. The shift in peak maximum intensity toward higher wavenumbers suggests a higher proportion of the silicon trihydride group *SiH_3, and, combined with the lower energy tail, is characteristic of an amorphous, more highly strained surface resulting from Sn incorporation into these alloyed NPs. Figure II.1.B.22b shows the corresponding XRD patterns, with the well-defined peaks corresponding to the (111), (220), and (311) facets pointing to mostly crystalline NPs; however, the elongated aspect of the (220) peak is indicative of some amorphous

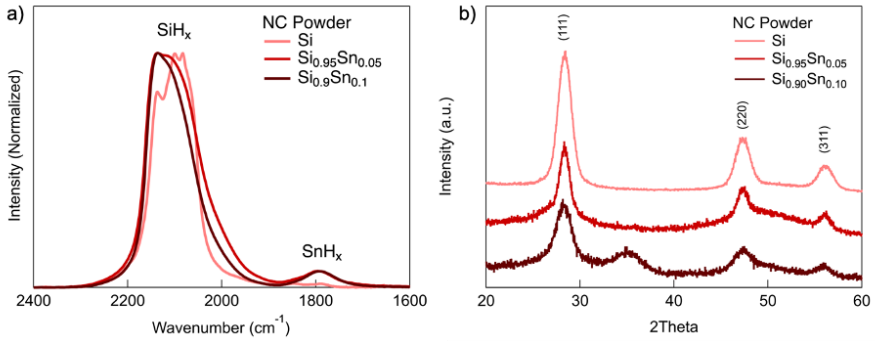

character.

Figure II.1.B.22. (a) DRIFTS spectra for pure Si, 5 atomic % Sn ($Si_{0.95}Sn_{0.05}$), and 10 atomic % Sn ($Si_{0.9}Sn_{0.1}$) NPs. Si-Sn alloys show a peak at 1,790 cm^{-1}, characteristic of SnH_x. (b) XRD patterns for Si, $Si_{0.95}Sn_{0.05}$, and $Si_{0.9}Sn_{0.1}$ NPs. The well-defined peaks point to the formation of a crystalline alloyed material.

As shown in the Q2 report, characterization on Si-Sn alloys was also done using TEM and EDS to examine the crystalline and elemental composition of the Si-Sn NPs. Figure II.1.B.23 shows a TEM image of a cluster of $Si_{0.9}Sn_{0.1}$ NPs in which the NPs appear highly monodisperse. The right-hand side of Figure II.1.B.23 displays EDS data. The bottom-left and bottom-right images map Si and Sn, respectively, within the NP sample. Importantly, the Sn signal is observed to track the Si signal, which provides evidence of alloy formation, whereas Sn hotspots would be indicative of phase segregation or pure-phase Sn particles. From the EDS, the Si:Sn ratio is calculated to be 85:15 at. %, which compares well with our Si:Sn 90:10 gaseous precursor ratio.

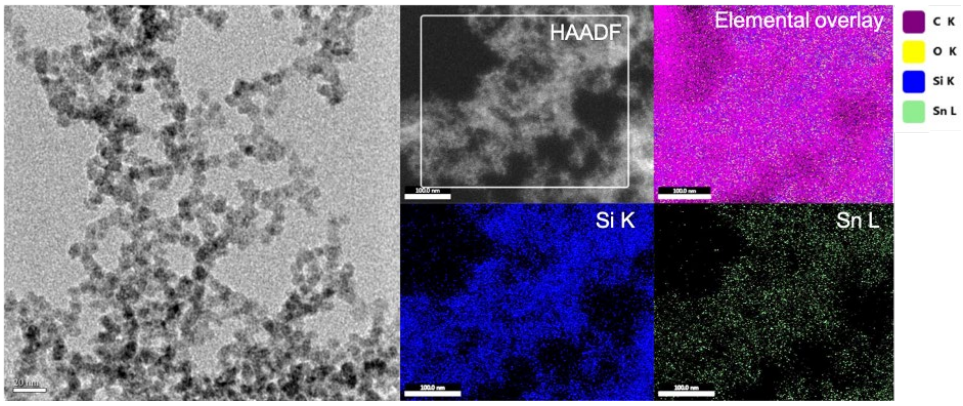

Figure II.1.B.23. Left: TEM image of a cluster of $Si_{0.9}Sn_{0.1}$ NPs. Scale bar is 20 nm. Right: EDS elemental analysis of the same NP sample shown on the left. Top left shows the HAADF image, whereas the bottom left and bottom right show Si and Sn mapping, respectively. The Si and Sn are seen to track each other, showing evidence of alloy formation. The top right shows the elemental map overlay including C, O, Si, and Sn.

These Si-Sn alloy NPs were constructed into composite anodes using our air-free methodology slurry and electrode fabrication processes described in other SEISta reports. In brief, two different compositions and sizes—7.4-nm $Si_{0.95}Sn_{0.05}$ and 5.1-nm $Si_{0.9}Sn_{0.1}$. Si-Sn NPs—were first blended into N-methylpyrrolidone (NMP) slurries with PAA binder and Timcal C65 conductive carbon. Si-Sn NPs and C65 conductive carbon were added at a 1:1 mass ratio, yielding anodes of ~33 wt % active material. Coin cells were then fabricated using a Li metal cathode and Gen2 electrolyte with 10 wt % FEC (Gen2F electrolyte). Cells were cycled at C/20 for three formation cycles and then C/5 for all additional cycles.

Figure II.1.B.24 displays plots of the electrochemical cycling data for the Si-Sn NP composite anodes and compares these directly to our intrinsic Si baseline electrodes. Specific capacity is quite reasonable for both alloy anodes, which retain greater than 90% of their original (fourth-cycle) capacity after 100 cycles. This value compares well with that of pure intrinsic Si@NMP NP-based anodes, as both alloys and pure-phase particle exhibit about the same capacity retention (Figure II.1.B.24c). Particularly noteworthy is the rapid stabilization of the CE in the first four cycles. Anodes made using $Si_{0.95}Sn_{0.05}$ NP anodes reach their maximum CE on the fifth cycle, whereas $Si_{0.95}Sn_{0.05}$ NP anodes are within 0.1% of their maximum CE by the fifth cycle (i.e., essentially stabilized by the fifth cycle). As part of our durability study, we have come up with a new metric for evaluating half-cell and full-cell data that can be used to quantify cycle life of anodes by plotting $CE_{cycle\ n}$ vs. cycle number (i.e., the cumulative CE over all cycles). For these Si-Sn alloy NP-based anodes, the cumulative CE over all cycles is just below 40% after 100 cycles, which is a vast improvement compared with that of intrinsic Si anodes with the same NMP surface coating (~15%, Figure II.1.B.24d).

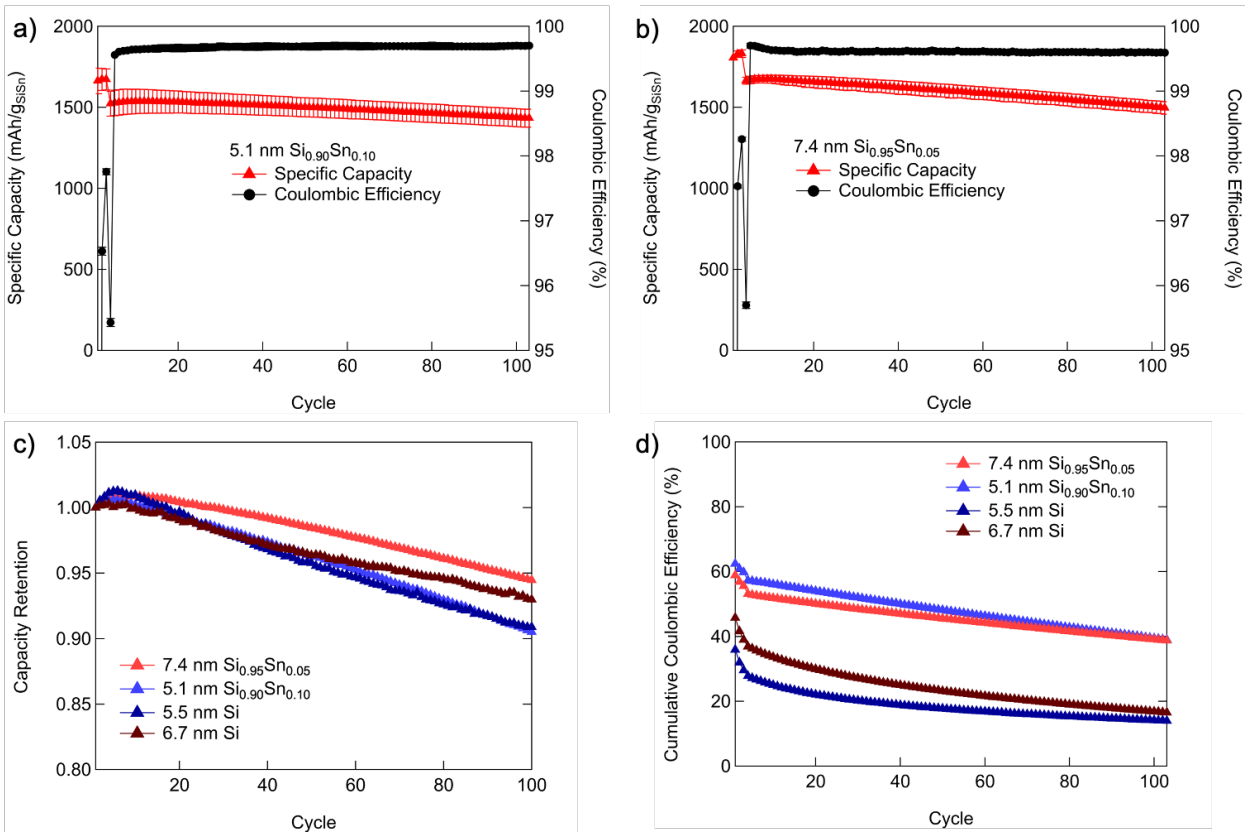

Figure II.1.B.24. Cycling performance for Si-Sn composite anodes. Specific capacity and coulombic efficiency over 103 cycles (3 forming cycles at C/20 and 100 cycles at C/5) are shown for (a) 5.1-nm $Si_{0.9}Sn_{0.1}$ and (b) 7.4-nm $Si_{0.95}Sn_{0.05}$-based NP anodes. Error bars are a one sigma deviation from a set of three anodes. (c) Capacity retention with respect to the fourth cycle and (d) cumulative coulombic efficiency over 103 cycles, including the forming cycles for the electrodes for both Si-Sn alloys and pure-phase Si NP-based anodes.

Finally, Figure II.1.B.25 shows differential capacity curves for the first three formation cycles at C/20 for Si-Sn NP composite anodes. Both plots show characteristic features during the first lithiation cycle at 1.2, 0.9, and 0.1 V vs. Li^+/Li that are attributed to SiH_x reduction, SEI formation, and crystalline Si lithiation, respectively. Subsequent lithiation cycles show features at 0.21 and 0.07 V vs. Li^+/Li that are indicative of amorphous Si lithiation, as expected for the second cycle and beyond. Interestingly, both the 5.1-nm $Si_{0.9}Sn_{0.1}$ and the 7.4-nm $Si_{0.95}Sn_{0.05}$ anodes exhibit a reduction feature at ~0.45 V vs. Li^+/Li during lithiation and a corresponding oxidative process as a shoulder on the delithiation peak centered at ~0.7 V vs. Li^+/Li. In previous SEISta reports, we have discussed this feature occurring with increasing intensity with decreasing Si NP size and believe it is related to surface strain at smaller NP sizes that may enhance Li-ion diffusion through the Si-SEI-electrolyte interface. Here, this feature appears to be about the same intensity for anodes made from both the 5.1-nm $Si_{0.9}Sn_{0.1}$ and the 7.4-nm $Si_{0.95}Sn_{0.05}$ NPs, and thus appears to be independent of size. We posit that the size independence of this feature for both 5.1- and 7.4-nm Si-Sn NP-based anodes is evidence of a strain-related effect due to Sn incorporation.

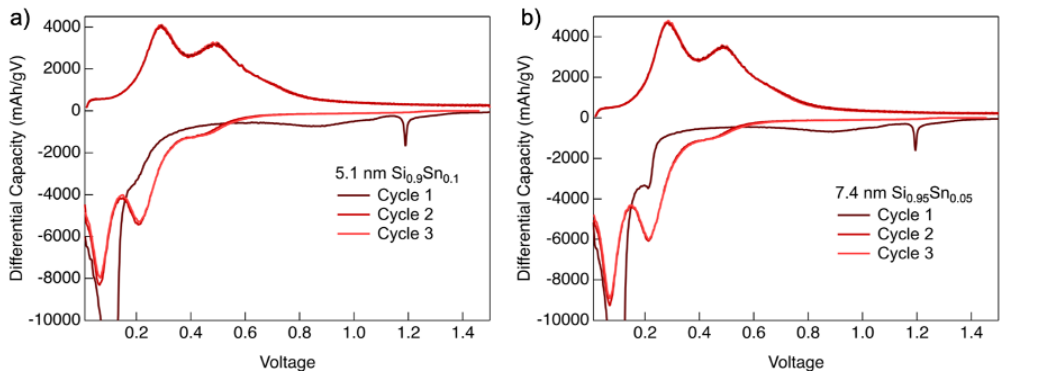

Figure II.1.B.25. Differential capacity plots for Si-Sn composite anodes. Differential capacity is shown for the first three cycles (C/20) for (a) 7.4-nm $Si_{0.95}Sn_{0.05}$ and (b) 5.1-nm $Si_{0.9}Sn_{0.1}$ anodes.

Investigation on Si-Based Metallic Glass Prepared by Splat Quenching

Materials synthesis and characterization

Metallic glasses are amorphous alloys produced from rapid cooling of a liquid melt to suppress the nucleation and growth of the crystalline phase. These rapid cooling rates can be achieved by several techniques, including sputtering, mechanical milling, melt spinning, and splat cooling [18]. Splat cooling is advantageous because practical sample sizes can be synthesized and high cooling rates can be achieved [19].

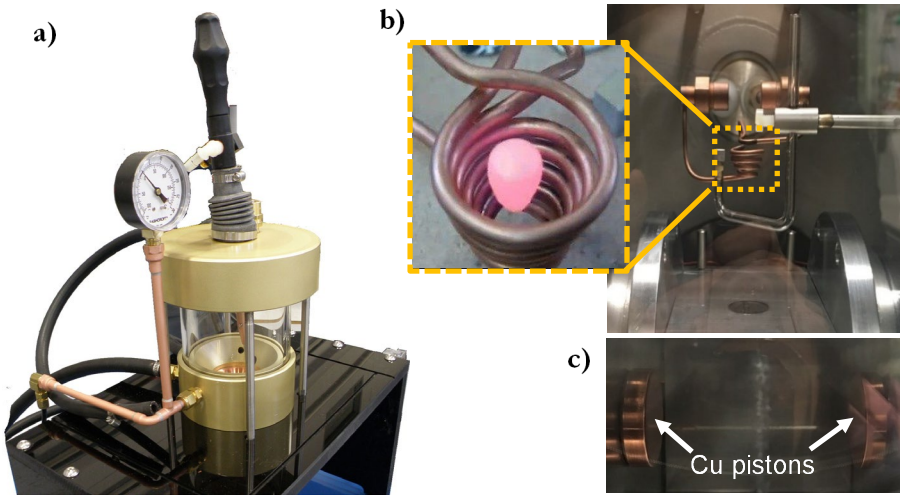

Figure II.1.B.26. Photographs of the arc-melter and the splat cooling system. (a) The parent $Al_{64}Si_{25}Mn_{11}$ alloy is fabricated by arc-melting Al, Si, and Mn powders. (b) The parent alloy is liquified by the induction levitation technique. (c) The two copper pistons splat cools the melt at a rate of ~10^5–10^6 K/s.

A splat cooling system heats an alloy inductively through the levitation melting technique. In the levitation melting technique, an alternating high current is applied through a levitation copper coil. The alternating current generates a high-frequency electromagnetic field, which produces the eddy current in the alloy. The eddy current plays two important roles: (1) melting the alloy by induction heating (typically above 1,000ºC) and (2) generation of electromagnetic body force, which makes the molten droplet levitate by balancing the gravimetric force. After a sufficient melting and homogenizing of an alloy, the levitation force is removed by stopping the alternating current. Subsequently, the molten metal is dropped at free fall, which is captured by a

laser detection module. The laser detection activates the high-speed motion of two copper pistons to "splat" the molten droplet. This process quickly quenches molten metals using cold metal surfaces at the cooling rate ranging from 10^5 to 10^8 Ks^{-1}. The entire synthesis is conducted in a high-purity Ar-filled environment, which allows minimal contamination of the alloy. However, the technique enforces at least one of the alloy components to have a ferromagnetic property for the electromagnetic levitation.

Among all Si-MGs, Al-Si-X (Cr, Ni, Fe, Mn) alloys are of particular interest because they have good glass-forming ability and large composition ranges can be fabricated through economical techniques [20]. Manganese is chosen as the third element due to its lower melting point and low cost. $Al_{64}Si_{25}Mn_{11}$ glass is prepared by rapidly cooling a liquid metal melt of a parent alloy using a splat cooling system. The parent alloy, which has the same composition as the glass ($Al_{64}Si_{25}Mn_{11}$), was prepared by melting stoichiometric amounts of Al, Si, and Mn powder in an arc melter under Ar (Figure II.1.B.26a). The parent alloy was then melted at ~1,100ºC in the splat cooling system through an induction levitation technique (Figure II.1.B.26b) and cooled by copper pistons at the rate of 10^5–10^8 K/s (Figure II.1.B.26c). The crystallinities of the parent alloy and the resulted rapid-cooled glass are measured by XRD (Figure II.1.B.27a). The parent alloy consists of three phases: crystalline Si (Fd-3m, JCPD No. 00-003-0549), Al (Fm-3m, JCPD No. 00-001-1179), and intermetallic $Al_{4.01}MnSi_{0.74}$ (Pm-3, 01-087-0528). After splat cooling, all crystalline peaks resolved into two broad bands at 20º and 42º, which suggests that the resulting material has an amorphous structure.

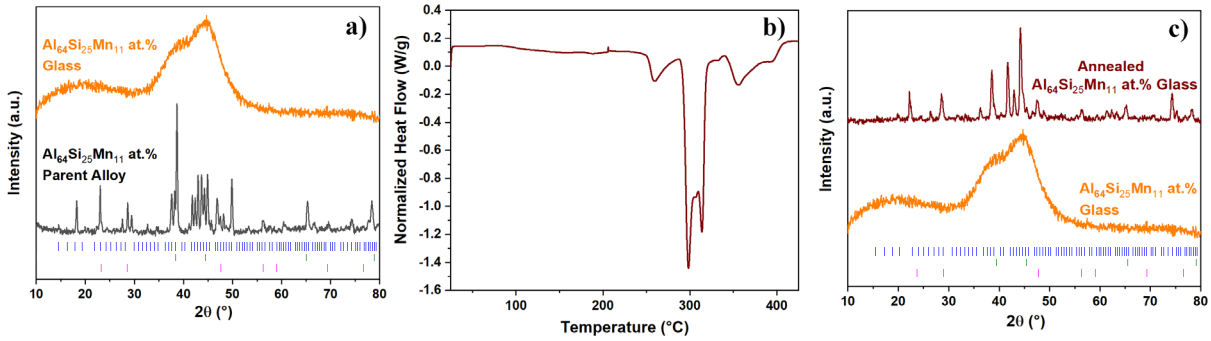

Figure II.1.B.27. (a) Powder XRD of the parent $Al_{64}Si_{25}Mn_{11}$ parent alloy (gray) and the amorphous analogue after rapid quenching (orange). (b) DSC curve of $Al_{64}Si_{25}Mn_{11}$ glass. (c) XRD of $Al_{64}Si_{25}Mn_{11}$ glass after DSC (red) in comparison to the pristine amorphous $Al_{64}Si_{25}Mn_{11}$ alloy (orange).

The amorphicity of the glass is further confirmed by DSC. The DSC curve (Figure II.1.B.27b) shows clear exothermic peaks, related to the crystallization process that the amorphous splat-quenched materials undergo at around 300ºC. Thus, these peaks correspond to the crystallization temperature, Tc, of the metallic glass. This crystallization is confirmed by XRD (Figure II.1.B.27c); the amorphous XRD pattern (the two broad humps) turn into sharp peaks, indicating the glass becomes a crystalline material after the DSC test.

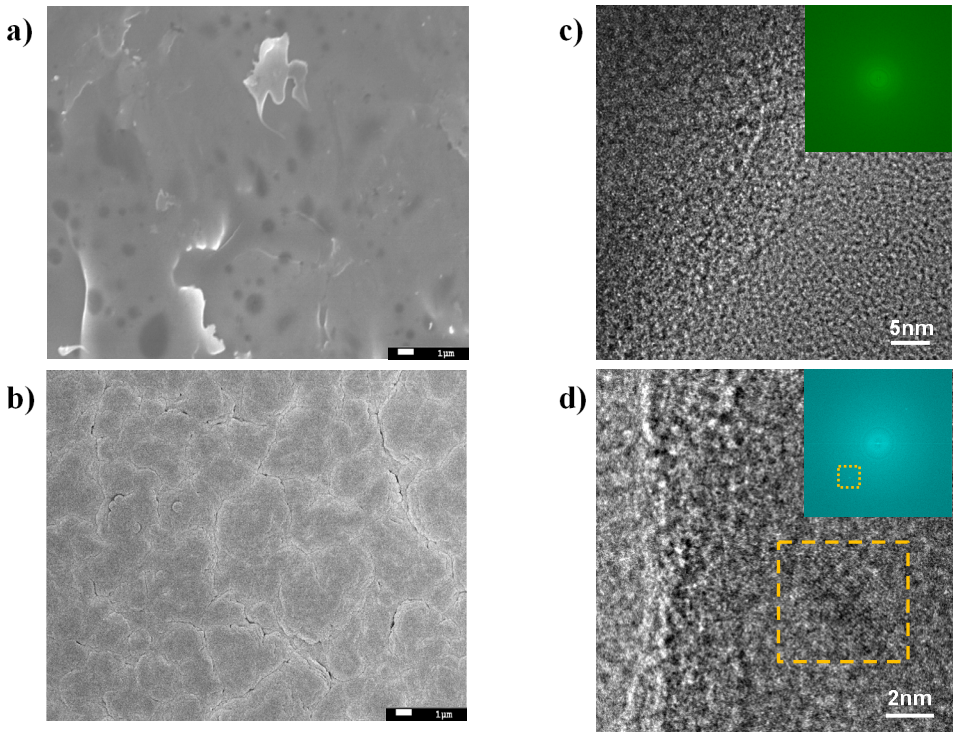

Figure II.1.B.28. (a) An SEM image of $Al_{64}Si_{25}Mn_{11}$ glass. (b) An SEM image of Si thin-film model electrode. (c) High-resolution TEM image of $Al_{64}Si_{25}Mn_{11}$ glass showing amorphous structure. (d) High-resolution TEM image of $Al_{64}Si_{25}Mn_{11}$ glass showing a nanocrystal grain with the size of ~4 nm (highlighted by a yellow box). The insets in (c) and (d) show the corresponding selected area electron diffraction (SAED).

The as-synthesized metallic glass is also analyzed using SEM and TEM. The SEM image of the metallic glass (Figure II.1.B.28a) shows dense and smooth surface topography in comparison to the Si thin-film model electrode counterpart prepared by sputter deposition (Figure II.1.B.28b). The TEM images and the corresponding SAED patterns show that the metallic glass predominantly has an amorphous phase (Figure II.1.B.28c). We conducted extensive TEM imaging and discovered that the only region of non-amorphicity are rare and isolated spots, with a maximum diameter of about 4 nm (yellow square in Figure II.1.B.28d).

Electrochemical characterization

The electrochemical characteristics of the metallic glass ($Al_{58}Mn_{12}Si_{30}$) is examined using various electrochemical methods: CV, galvanostatic cycling (GC), and electrochemical impedance spectroscopy (EIS). The metallic glasses are cycled using the standard three-electrode Swagelok cells against lithium in the Gen 2 electrolyte (1.2 M $LiPF_6$ EC:EMC (3:7 wt %)).

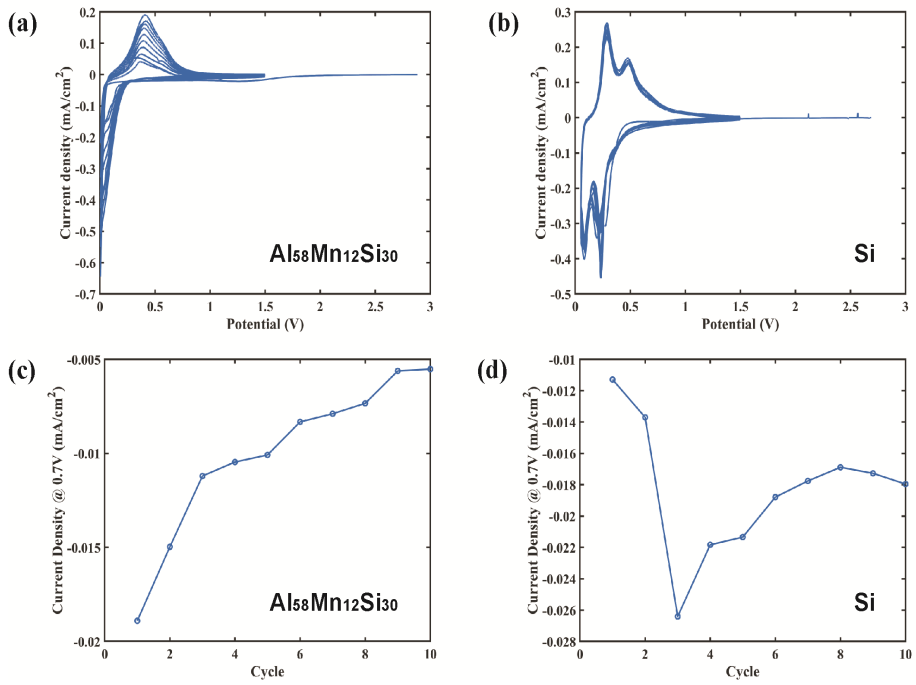

Figure II.1.B.29. Cyclic voltammograms of (a) $Al_{58}Mn_{12}Si_{30}$ and (b) Si at 0.1 mV/s for 10 cycles. The evolution of current density at the potential value of 0.7 V for (c) $Al_{58}Mn_{12}Si_{30}$ and (d) Si.

First, $Al_{58}Mn_{12}Si_{30}$ glass and the 500-nm Si model electrode are subjected to 10 CV cycles at the voltage sweep rate of 0.1 mV/s (Figure II.1.B.29a,b). The voltage sweep ranges are set to be 5 mV to 1.5 V and 50 mV to 1.5 V for the metallic glass and the Si model electrode, respectively. The cyclic voltammogram of $Al_{58}Mn_{12}Si_{30}$ shows a sharp cathodic peak during the first lithiation, which may be attributed to the slow diffusion of Li in the metallic glass. The lithiation peak broadens, and the magnitude of the anodic peak increases as the cycling number increases, indicating gradual activation of the metallic glass (Figure II.1.B.29a). Figure II.1.B.29c,d presents the current density values at 0.7 V during the lithiation process extracted from the cyclic voltammogram. The reasoning for choosing 0.7 V is because it is lower than the EC reduction potential and higher than the lithiation potential. Thus, the current density at 0.7 V can serve as a representation of interfacial instability. The metallic glass shows the current density of ~19 $\mu A/cm^2$ in the first cycle, which progressively decreases to 5 $\mu A/cm^2$ in the tenth cycle (Figure II.1.B.29c). The Si thin-film counterpart shows the current density of ~11 $\mu A/cm^2$ in the first cycle, which fluctuates in the range of 15–27 $\mu A/cm^2$ in the subsequent cycles (Figure II.1.B.29d). The overall magnitude of the current density of Si at 0.7 V is three- to fourfold higher than that of $Al_{58}Mn_{12}Si_{30}$.

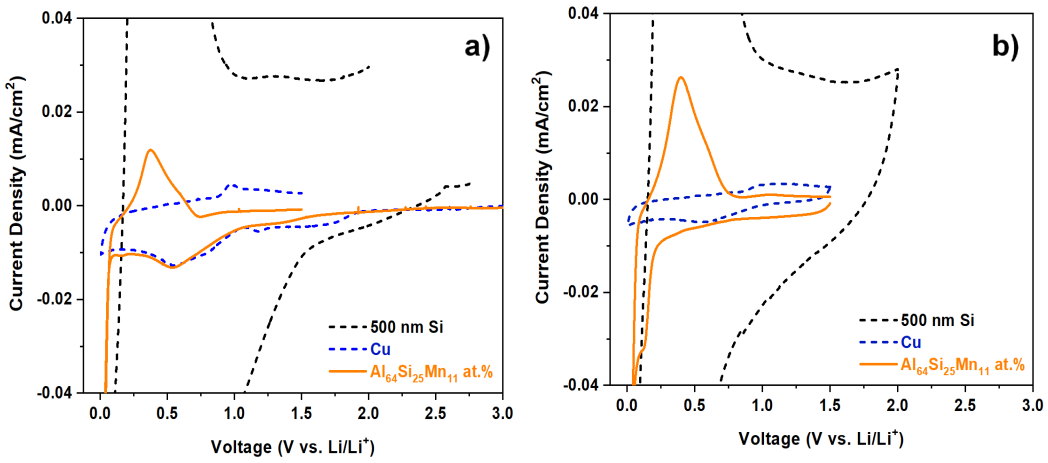

Figure II.1.B.30. Cyclic voltammogram of 500-nm Si model electrodes (dash/black), Cu foil (dash/blue), and $Al_{64}Si_{25}Mn_{11}$ glass (orange) during the (a) first and (b) second cycle.

Figure II.1.B.30 presents the CV curves of a 500-nm Si model electrode, $Al_{58}Mn_{12}Si_{30}$ glass, and a Cu foil obtained from a separate set of CV experiments. The CV curve of the $Al_{58}Mn_{12}Si_{30}$ shows the substantially lower current density at around the SEI formation potential (~0.6 V) compared to the Si model electrode; the current density in the potential region is comparable to that of Cu, which is known to form a stable passivation layer. This set of CV investigations suggests the stable formation of SEI on the $Al_{58}Mn_{12}Si_{30}$ surface.

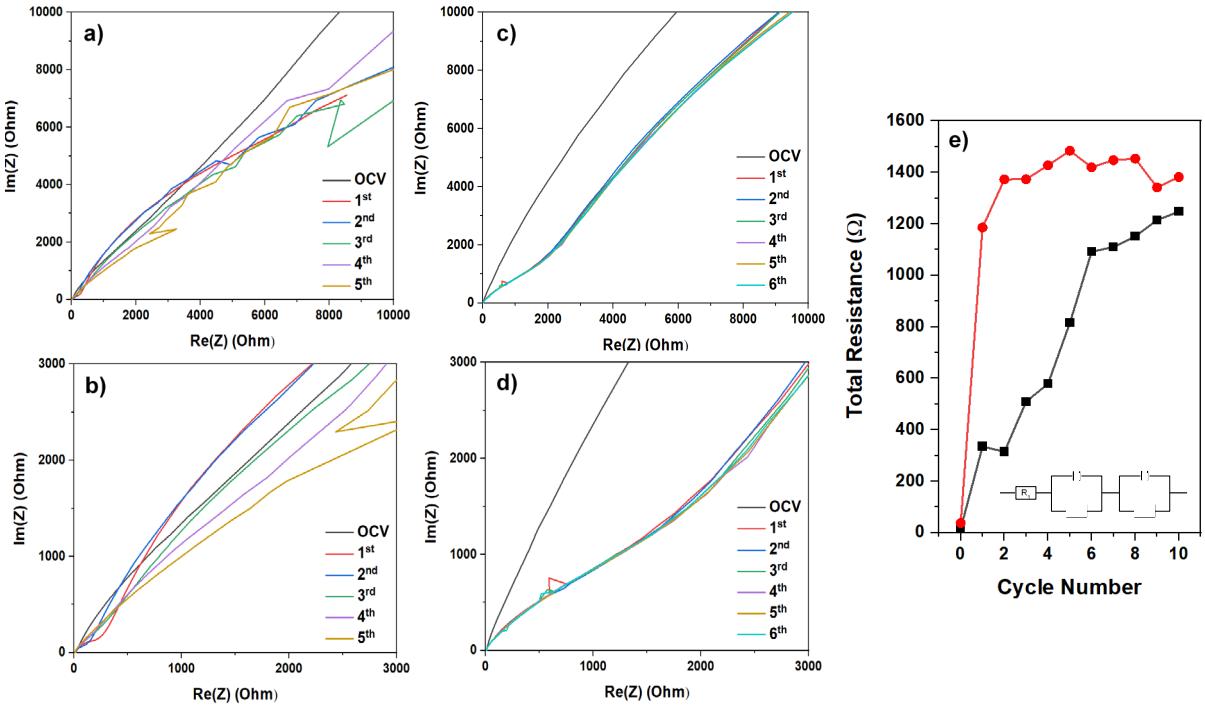

Figure II.1.B.31. (a) Nyquist plots of Si model electrode and (b) their magnified view. (c) Nyquist plots of $Al_{58}Mn_{12}Si_{30}$ glass and (d) their magnified view. (e) The total resistance evolutions of the metallic glass and the Si model electrode with increasing cycle number.

We further confirm the improved interfacial stability of $Al_{58}Mn_{12}Si_{30}$ by EIS. EIS is measured after each CV cycle to compare the stability of SEI between the Si model electrode (Figure II.1.B.31a,b) and the $Al_{58}Mn_{12}Si_{30}$ glass (Figure II.1.B.31c,d). The total resistance accounting for the electrode, electrolyte, and the interface is calculated from the Nyquist plot and presented in Figure II.1.B.31e. It is clear from the total

resistance evolution that the $Al_{58}Mn_{12}Si_{30}$ glass formed a stable SEI during initial cycles, whereas Si forms continuously evolving SEI.

To assess the specific capacity, three independent $Al_{58}Mn_{12}Si_{30}$ pellets are galvanostatically cycled at a current density of ~50 μA/cm^2. It should be noted that the metallic glass is in a foil form with the lateral dimensions in millimeter scale and the thickness of 2–4 mm. With the enormous volume change of both Al and Si, the foil form of metallic glass is expected to undergo severe mechanical degradation. Thus, only the first discharge capacity is selected to evaluate the specific capacity. Figure II.1.B.32 shows the potential profiles of three $Al_{58}Mn_{12}Si_{30}$ during one galvanostatic cycling. The average specific discharge capacity of $Al_{58}Mn_{12}Si_{30}$ is ~950 mAh/g, with the maximum value of 1,150 mAh/g. The measured capacity is already comparable to its theoretical capacity of ~1,490 mAh/g. It is found that the galvanostatic cycling causes severe pulverization (inset of Figure II.1.B.32). Thus, optimizing the electrode structure is expected to improve the practical capacity close to its theoretical capacity.

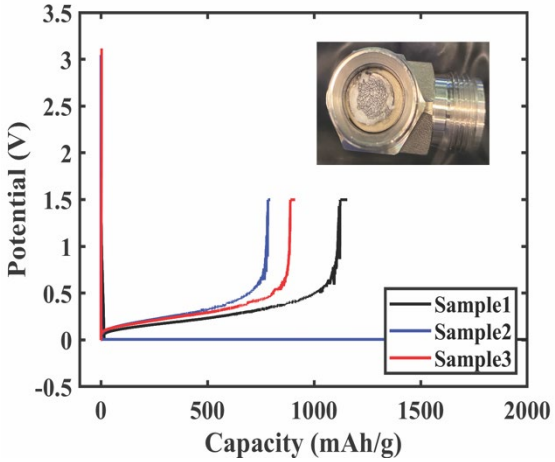

Figure II.1.B.32. Galvanostatic cycling of three $Al_{58}Mn_{12}Si_{30}$ glass samples. One GV cycling causes a drastic pulverization of the metallic glass (inset).

For XPS characterization, the $Al_{58}Mn_{12}Si_{30}$ film is subjected to a linear voltage sweep from the open circuit potential to 5 mV (half CV cycle) vs. Li at a sweep rate of 0.1 mV/s. Both this sample and pristine MG were analyzed. In the pristine sample (Figure II.1.B.33), all the constituent elements are detected but in slightly different concentrations than the nominal stoichiometry. The composition at the surface is $Al_{84}Mn_{01}Si_{15}$. Further, the more oxyphilic elements—Al and S—are in part oxidized. It is unclear if this is just a small amount of surface oxidation or if it is a property of the bulk, due to the fact that the pristine powders were exposed to an ambient atmosphere.

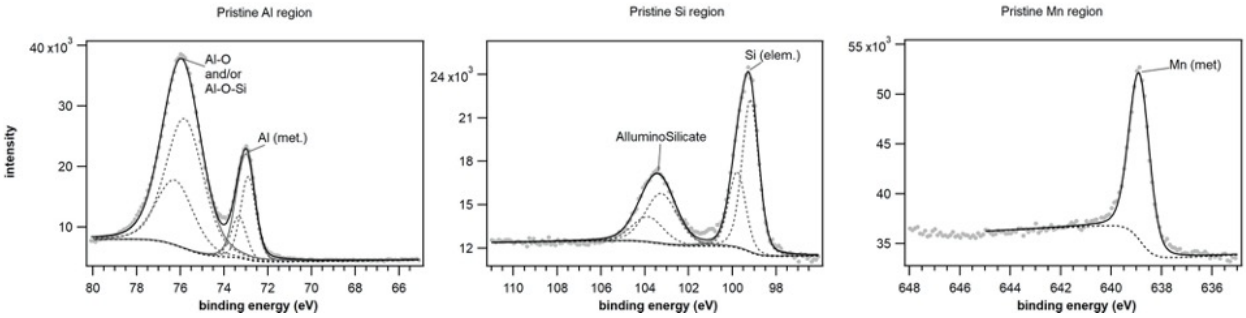

Figure II.1.B.33. XPS spectra of the glasses in pristine state. A small amount of oxides was detected in addition to the elements in their unreacted metallic state.

The BM glasses were further analyzed after the first lithiation step. The constituent elements of the MG do not show much evolution except for the oxide's components (Figure II.1.B.34). The aluminosilicate phase in part

converts to the binary oxides and the silicon peak further shows a component attributed to fluorinated silica. A small amount of manganese oxide is also formed.

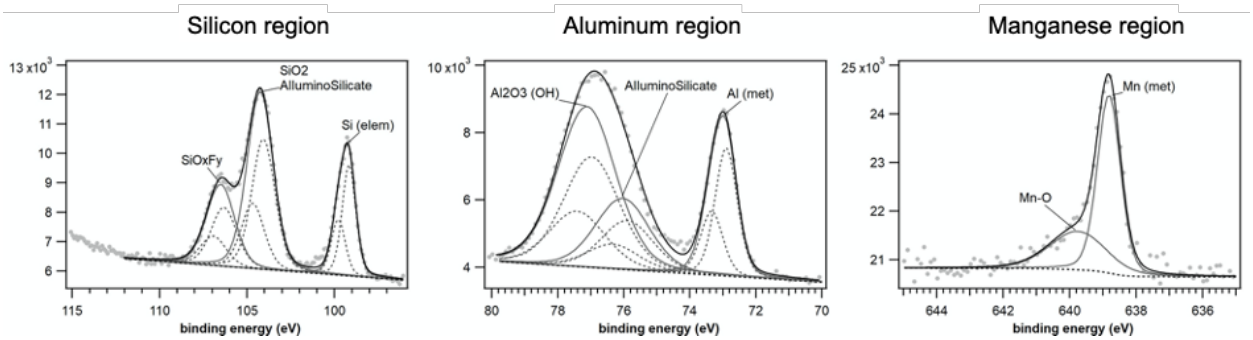

Figure II.1.B.34. XPS spectra of the BM glasses in pristine state. A small amount of oxides was detected in addition to the elements in their unreacted metallic state.

In terms of the SEI formed during the lithiation steps, we can claim that this is a very thin layer, in agreement with the CV data showing very limited charge consumption. This statement is based on the fact that all the constituent elements of the metallic glasses' electrode can be easily detected—Al, Si, and Mn—which means that the SEI is much thinner than the probing depth of these measurements (4–6 nm). This is the opposite of what happens for the Si anode, where a thick SEI is formed on the electrode surface. The composition of the SEI is also different from the one usually observed in silicon (Figure II.1.B.35). The most noticeable difference is the complete absence of carbonate decomposition products. The C1s core levels shows some compounds that contain oxygen, but at the moment it is not possible to determine the exact nature of these species and FTIR will have to be performed to be conclusive. The main SEI components are the decomposition products of the salt, namely LiF and fluorophosphates.

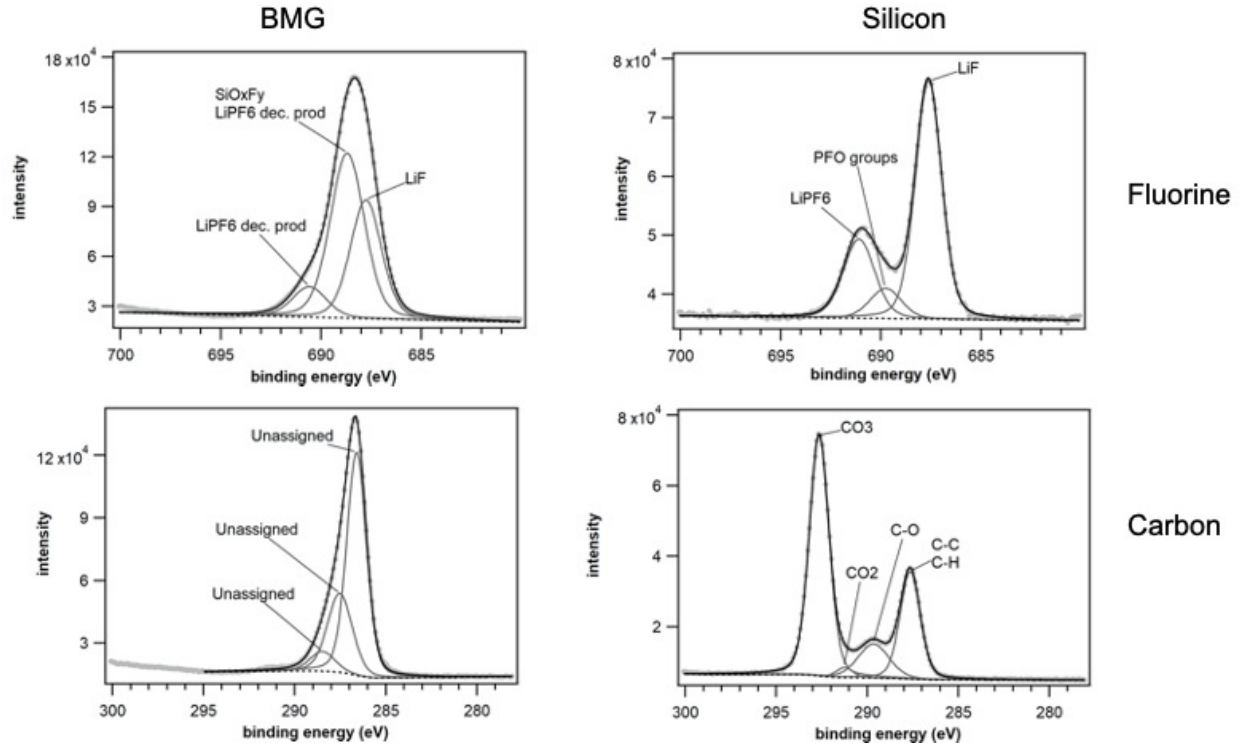

Figure II.1.B.35. XPS spectra of the BM glasses (BMG) SEI components compared to the SEI formed on Si anodes. A much thinner SEI is observed, which is also compositionally different.

Overall, the metallic glasses show an improved surface passivation in comparison to Si as demonstrated by a lower-charged consumption in electrochemical test and much thinner SEI as determined by spectroscopic methods, consisting primarily of inorganic species.

Alloying mechanisms

In order to maintain structural integrity and avoid pulverization, the glass should remain amorphous throughout electrochemical cycling. In this regard, it is essential to investigate whether $Al_{64}Si_{25}Mn_{11}$ glass phase separates into crystalline phases as it alloys with Li. Ex situ XRD (Figure II.1.B.36a) is performed on $Al_{64}Si_{25}Mn_{11}$ glass at the lithiated (0.005 V) and delithiated (1.5 V) states to investigate the possible phase change during cycling. At the lithiated state, a broad-band emerged at higher 2θ, at 62°, indicating a formation of a new amorphous phase. The broad-band observed at ~42°, which also presents in the XRD pattern of the as-synthesized, can be explained by incomplete lithiation of the glass foil. The additional peak visible in the XRD pattern of the lithiated stage is attributed to LiF and Li_2CO_3 electrolyte decomposition products, as films were only dried but not washed off prior to the XRD measurements. At the delithiated state, the intensity of the broad peak at 2θ = 62° decreased. The peak is not expected to fully disappear based on the irreversibility observed in the CV and galvanostatic cycling curves. The increased intensity of the 2θ = 42° peak and the reemergence of the broad-band at lower 2θ indicates the formation of the original $Al_{64}Si_{25}Mn_{11}$ phase observed in the pristine samples. Most importantly, no crystalline phases were observed, suggesting $Al_{64}Si_{25}Mn_{11}$ glass remains amorphous throughout the cycling. For further confirmation, ex situ TEM analysis was conducted on the lithiated glass (Figure II.1.B.36b). The high-resolution TEM and the SAED pattern of the lithiated glass show no sign of a crystalline phase, which agrees with the results from the ex situ XRD measurements.

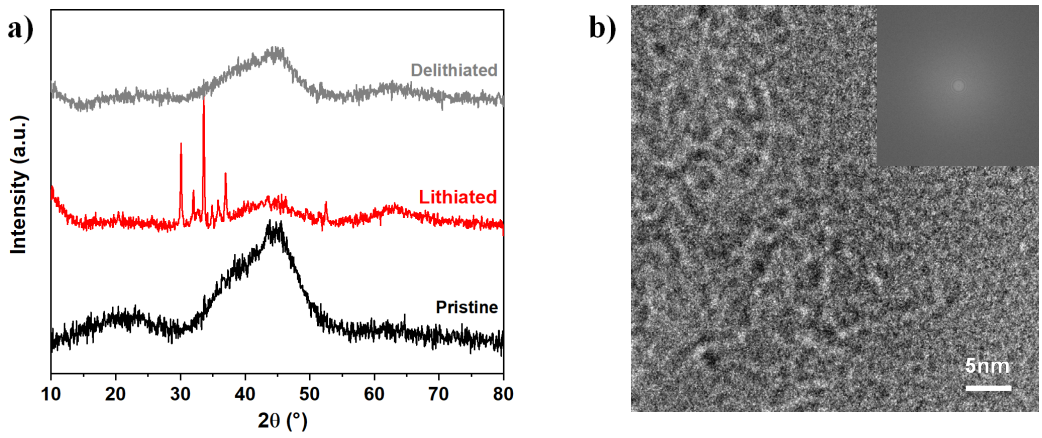

Figure II.1.B.36. (a) Ex situ XRD of the $Al_{64}Si_{25}Mn_{11}$ glass at the pristine state (black), lithiated state (red), and delithiated state (gray). (b) Ex situ TEM of the $Al_{64}Si_{25}Mn_{11}$ glass at the lithiated state.

Density Functional Theory and Ab Initio Molecular Dynamics Studies on Various Si-Based Alloys

Volumetric expansion is perhaps the most crucial factor in the cycling stability of an electrode, as evidenced by the wide body of published research surrounding morphological tuning of Si to mitigate electrode cracking from volumetric expansion. Obrovac et al. previously claimed that the volumetric expansion of Si electrodes cannot be mitigated through the use of alloyed components, because the volumetric expansion is linearly proportional to the number of Li atoms alloyed [21]. Although this is generally true in crystalline alloys, we find that this is not the case for amorphous alloys. The Li partial molar volume in crystalline silicides is constant, 14.8 $Å^3$ per Li atom; however, in amorphous silicides, it can vary between ~12 and 21 $Å^3$ per Li atom, as seen in Figure II.1.B.37. The effects of Li partial molar volume can be seen when comparing MnSi and SiNi, both of which have nearly identical initial molar volumes; however, the Li partial molar volume is lower in SiNi. Although the Li partial molar volume is 14% lower than MnSi, the volumetric expansion at $x_{Li} = 0.5$ is nearly the same. Additionally, a low Li partial molar volume is most prevalent in compositions that have a low unlithiated molar volume.

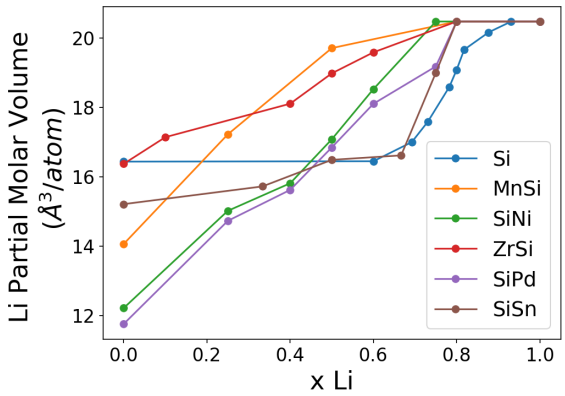

Figure II.1.B.37: Li partial molar volumes of Si alloy electrodes.

More impactful to the volumetric expansion is the initial molar volume of the electrode. As illustrated in Figure II.1.B.38, the Si alloys with the highest initial molar volume (Si-Sn) have the lowest volumetric expansion. Likewise, MnSi and SiNi have the lowest molar volumes and in turn have the largest volumetric expansions. With this in mind, we conclude that alloyed components, although capable of mitigating volumetric expansion, do so at the expense of volumetric energy density.

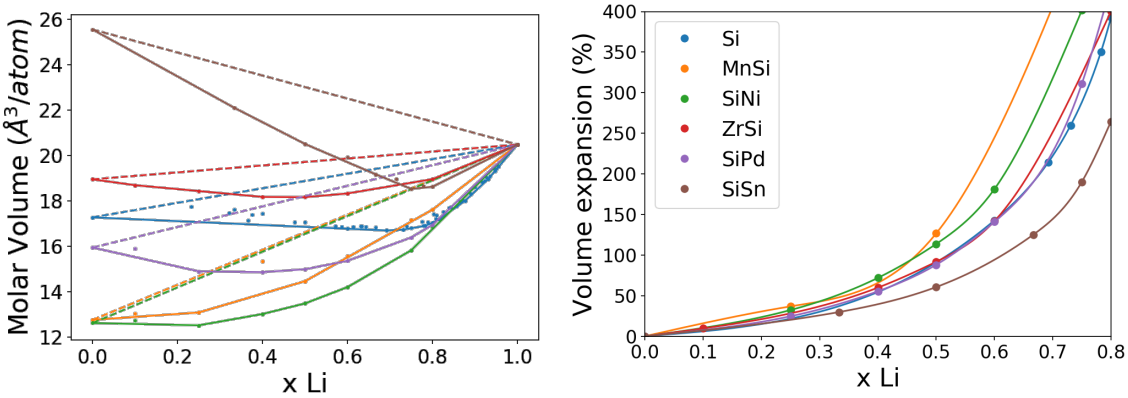

Figure II.1.B.38: (a) Molar volumes and (b) volumetric expansion of Si alloy electrodes. The dotted lines in (a) indicate the volume of ideal mixtures.

In addition to the volumetric expansion, we have investigated the Si clustering and networking behavior in the Si alloys upon lithiation. We have previously reported on the clustering of Si, finding a quick decline in the amount of networked Si as Li is alloyed, eventually breaking up into aggregates of 2, 3, 4, and 5 atoms. We have extended this analysis, converting each structure into graph representations, where each atom and bond

is represented by a node and edge, respectively. By including periodic boundary conditions, we can easily identify aggregates as connected components; all other Si atoms are considered networked. This is used to explicitly identify Si networks and track their breakup. In the case of pure Si, the Si becomes half-networked at $x_L \approx 0.28$. When alloyed with active elements, the Si networks persist longer than in the base case. This is generally due to the active element lithiating before Si, allowing larger Si aggregates/networks to remain. Conversely, inactive elements result in a breakup of the network at lower lithiation levels. This is primarily the result of more uniform distribution due to the favorable bonding between Si and the inactive elements.

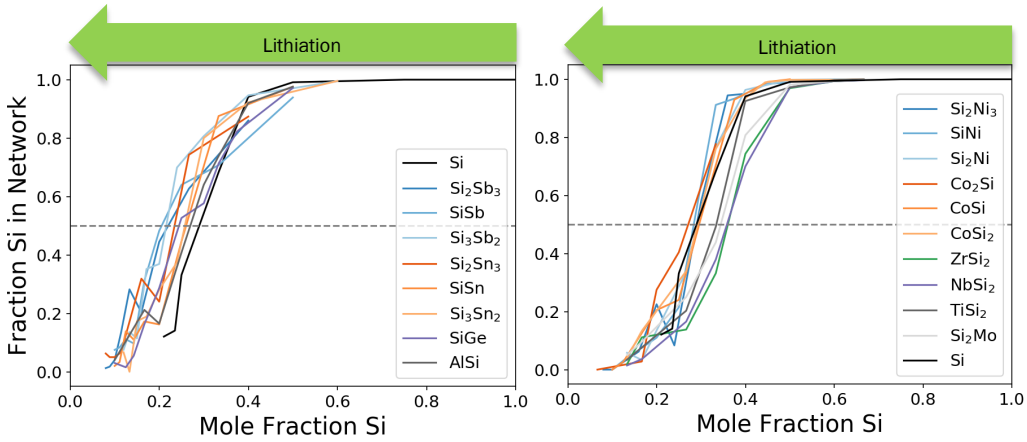

Figure II.1.B.39: Si connectivity/networking in binary Si alloys with active (left) and inactive elements (right). Dotted line is a reference line indicating the point at which half the Si atoms are not clustered.

Conclusions

Various combinations of Si-based alloys were thoroughly explored using microscopy, spectroscopy, electrochemical, and computational methods.

First, Si-Sn thin-film electrodes prepared by magnetron co-sputtering were studied and compared with Si thin-film model electrodes. The calculated experimental capacities of the Si_xSn_{1-x} thin films suggest nearly full lithiation at a high capacity of over 2,000 mAh g^{-1} for the films with $x \geq 0.69$. The optimal composition ($x = 0.8$) achieves stable cycling without the use of any binder, conductive carbon, or electrolyte additive. Interfacial studies on Si vs. Si-Sn by SEM and EDS reveal dramatically different morphology/composition for the Si and Si-Sn thin-film electrodes upon initial lithiation. The Si film surface is teeming with O-rich microstructures, whereas the Si-Sn surface shows uniform morphology and elemental distribution. This observation deserves further investigation on the interphase species formed on the Si-Sn vs. Si during (de)lithiation in an air-free environment.

Second, the nonthermal PECVD synthesis method was used successfully to produce Si-Sn alloy NPs. Si-Sn NPs were incorporated into composite anodes using our air-free process and demonstrate excellent capacity retention and cumulative coulombic efficiency over 50 cycles. Future work will explore the origin of the redox wave in the dQ/dV plots with respect to strain induced by Sn and by modifying our synthetic procedures to increase the Si-Sn NP size. Additionally, we plan on exploring whether the surface chemistries that result in higher performance for intrinsic Si NP-based anodes also translate to better performance in Si-Sn-based composites.

Third, Si-based metallic glass, $Al_{64}Si_{25}Mn_{11}$, was successfully synthesized through a splat cooling system by rapidly cooling the liquid melt alloy and suppressing the nucleation and growth of the crystalline phase. $Al_{64}Si_{25}Mn_{11}$ glass exhibits good specific capacity and has demonstrated superior interfacial stability in comparison to elemental Si. EIS shows a drastic increase in the total resistance of the 500-nm Si electrode after 10 cycles. On the contrary, the total resistance of the glass stayed almost constant, suggesting the formation of a stable SEI layer. This was further confirmed by both electrochemical and XPS analysis, which shows a lower amount of charges consumed during the lithiation process resulting in a very thin SEI. These findings strongly

support the validity of our approach: a stabilization of electrode–electrolyte interface by using amorphous multicomponent metallic glass as an anode material.

Finally, the computational studies revealed the impacts of alloying on volumetric expansion: (1) electrodes with large initial molar volumes yield lower volumetric expansion, at the expense of volumetric capacity, and (2) decreasing Li partial molar volume produces a decreased volumetric expansion, although its impact is far less pronounced than the initial molar volume. Thus, we conclude that although alloying can help decrease volumetric expansion, due to the inverse relationship between initial molar volume and volumetric expansion, a trade-off must be made. The Si networking/clustering in the amorphous alloys can be tuned through (1) the addition of active components to promote network retention and (2) the use of inactive components to promote a more homogeneous single-phase lithiation.

To sum up, the investigated Si-Sn alloys and Si-based metallic glasses were commonly showing improved electrochemical characteristics and physical properties compared to pure Si electrodes. Further optimization of elements and stoichiometry of Si-based alloy guided by the computational studies has the potential to resolve the problems associated elemental Si and serve as the next-generation lithium-ion battery anode materials.

Understanding SEI Chemistry

Gabriel Veith (ORNL), Nathan Neale (NREL), Elisabetta Arca (LBNL), Chunmei Ban (NREL), Chen Fang (LBNL), Sarah Frisco (NREL), Yeyoung Ha (NREL), Sang-Don Han (NREL), Steve Harvey (NREL), Emma Hopkins (ORNL), Bin Hu (ANL), Zoey Huey (NREL), Chun-Sheng Jiang (NREL), Baris Key (ANL), Robert Kostecki (LBNL) Xiang Li (ANL), Zhifei Li (NREL), Gao Liu (LBNL), Mowafak Al-Jassim (NREL), Jagjit Nanda (ORNL), Andrew Norman (NREL), Kristin Persson (LBNL), Manuel Schnabel (LBNL), Zhangxing Shi (ANL), Paul Stradins (NREL), Caleb Stetson (NREL), Glenn Teeter (NREL), Guang Yang (ORNL), Insun Yoon (LBNL), Andriy Zakutayev (NREL), Zhencheng Zhang (ANL), Lu Zhang (ANL).

Background

It has become abundantly clear that the solid–electrolyte interface on a silicon electrode is unstable, resulting in a poor calendar life. We have coined this effect "breathing" due to the continuous decomposition and reformation of the SEI with cycling and at various states of charge along with the commensurate growth of a thick or thin SEI structure at these various states of charge. What is not clear is how changes in the surface chemistry and electrolyte chemistry may affect this SEI stability and breathing. This fundamental lack of knowledge prompted the areas of inquire detailed here.

The first focus area revolved around identifying what the role is of a silicon oxide surface versus a pure silicon or silicon sub-oxide surface. Previous work in FY 2019 revealed that the choice of silicon surface chemistry resulted in drastic changes in electrolyte decomposition at open circuit voltage. This year, we explored the possibility of the change in surface chemistry directing the formation of a more (or less) stable SEI layer.

Another focus area involved understanding how a binder changes the SEI. In composite cells, the binder covers all or some of the available surface area, likely indicating that this will directly mediate SEI formation. Indeed, in FY 2019, neutron reflectivity work revealed that a binder may act as an ion- or solvent-selective membrane, enabling the transport of one or more species to the surface where they may form an SEI layer. Could this effect be used more extensively to control and direct the SEI formation and improve stability by driving specific ions or molecules to the surface or preventing them from leaving?

The third area focuses on new electrolyte formulations. It has become clear that the standard 1.2 M $LiPF_6$ ethylene carbonate/ethyl methyl carbonate electrolyte (commonly described as Gen 2) is not stable in direct contact with most silicon-based surfaces over extended calendar lifetimes. The SEISta team previously identified that one of the stable species on a silicon electrode was an ether functionality. Based on this result, the team explored glyme-based electrolytes (ether functionality).

The fourth area of focus was on the use of gaseous additives (CO_2) as a way to promote the SEI formation reaction. This approach differs from the traditional use of additives like vinylene carbonate or FEC. This approach also offers the opportunity to explore what happens to the gasses produced when the electrolyte decomposes with cycling.

In a fifth area, the team focused on understanding the mechanical properties of the SEI. The hypothesis was that the mechanical stability of the SEI could play a role in stabilizing the silicon at extended periods of time and low voltages (<0.1 V). To explore this hypothesis, we undertook various mechanical and optical experiments to evaluate the mechanical stability of the SEI as a precursor to changing the electrolyte composition in a way to introduce improved mechanical stability.

Finally, we explored how both size and surface chemistry of silicon nanoparticles grown via nonthermal PECVD synthesis affect the performance and stability of Si NP-based composite anodes. Specifically, we compared how the SEI growth and dissolution differs in 3.9-nm vs. 30-nm-diameter Si NPs. We also explored hydrophobic vs. hydrophilic molecular coating on the Si surfaces to test the influence of the differing ionic and electron properties of the formed coatings.

Results

1. Role of surface oxides in SEI formation and chemistry – vapor deposited films

To alleviate the large volume change, silicon oxides have been considered as alternatives to pure silicon electrodes. There have been some mechanistic studies about the lithiation process of SiO as anodes in lithium-ion batteries; however, it is not yet fully understood how different levels of oxygen in the SiO_x electrodes affect the lithiation behavior and the SEI formation. The presence of oxygen is almost inevitable in Si anodes, where the surface of Si forms a native oxide layer when exposed to air; different preparation processes for Si electrodes may also lead to different levels of oxygen content in the bulk Si. To investigate the role of oxygen in Si anodes, we prepared model Si thin-film electrodes with different levels of oxygen to study their lithiation behaviors and the SEI formation. We have demonstrated the impact of oxygen on the electrochemical behavior of the Si electrodes, where Si electrodes with higher oxygen level in the bulk exhibit a longer irreversible plateau at around 0.6 V during the first lithiation process. In this report, we present the chemical and physical characterization of pristine and cycled electrodes to clarify the impact of oxygen on the SEI formation and the lithiation/delithiation behaviors of Si anodes.

In this study, SiO_x anode with minimum oxygen content (referred to as Si) was prepared by magnetron sputtering of Si target under low base pressure (~2×10^{-7} torr), low deposition pressure (5 mtorr), and short work distance (8 cm). This Si anode was assembled into coin cells after the deposition and did not expose to air in the process. We intentionally expose this Si anode in air to obtain Si with native oxide layer (Si_NO). To prepare SiO_x anodes with higher oxygen level, we performed Si and SiO_2 co-sputtering with different power combinations (90-30 W, 90-60 W, 90-90 W, 60-90 W) for the Si and SiO_2 target and obtained SiO_x anodes with four different oxygen levels.

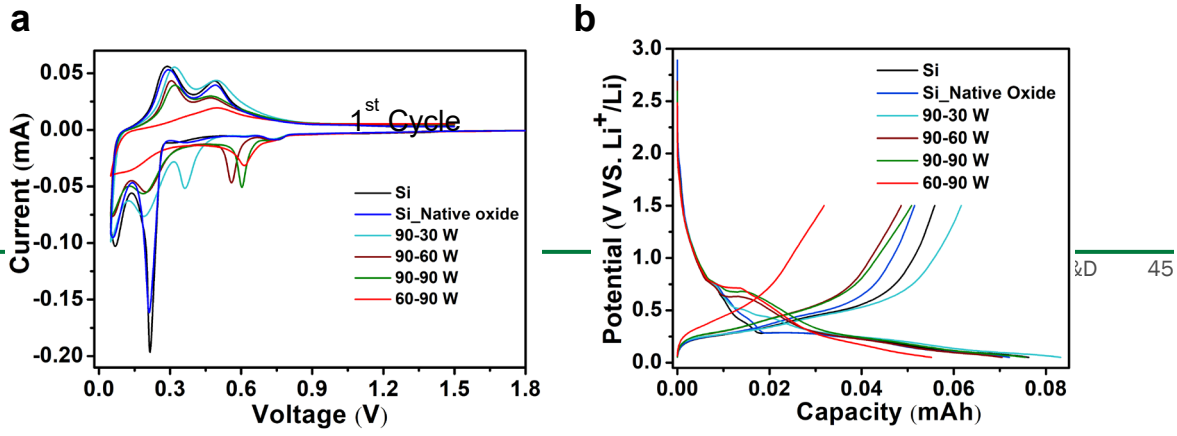

Figure II.1.B.40. The CV and first-cycle galvanostatic charge-discharge profiles of Si, Si with native oxide layer, and four SiO_x anodes with different oxygen levels tested in the potential range of 0.05–1.5 V (a) CV and (b) galvanostatic charge-discharge.

The obtained Si, Si_NO, and SiO_x anodes with different levels of oxygen content were first evaluated with CV. As shown in Figure II.1.B.40a, all the Si, Si_NO, and SiO_x anodes exhibit a small reduction peak at around 0.7 V, which should be due to electrolyte reduction. By comparing Si, Si_NO, and SiO_x anodes, a distinct difference is observed in the first CV cycle. All the SiO_x anodes prepared by co-sputtering show an extra reduction peak in the potential range of 0.3–0.6 V, where the peak position shifts to lower potential with lower oxygen content. The galvanostatic charge-discharge profiles of all Si, Si_NO, and SiO_x anodes (Figure II.1.B.40b) agrees well with the CV data, where the Si and Si_NO show similar shape during the first discharge and the SiO_x anodes with higher oxygen content have a much longer plateau in the potential range of 0.5–0.7 V. The potential of the plateau is higher for SiO_x with higher oxygen level, which again agrees with the potential of the reduction of SiO_x during the first cathodic CV cycle. This potential range should correspond to the reduction of SiO_x by lithium. As the Si anode has very low oxygen content, it did not show this plateau. Even for Si_NO with surface native oxide layer, the oxygen level is still not high enough to exhibit this plateau.

Sample	Original Pristine Film Resistivity	Resistivity Change After Lithiation to 0.55 V	Resistivity Change After Lithiation to 0.05 V	SEI Thickness After Lithiation to 0.05 V
Si **(Si/SiO_2 90/0)**	~10^3 Ω·cm	Slight decrease	Three order of magnitude decrease	Thickest
Si_NO **(Si/SiO_2 90/0)**	~10^3 Ω·cm	Slight decrease	Three order of magnitude decrease	Thicker
SiO_x_1 **(Si/SiO_2 90/30)**	~10^5 Ω·cm	Order of magnitude decrease	Five order of magnitude decrease	Thicker
$SiO_{0.6}$ **(Si/SiO_2 90/60)**	~10^6 Ω·cm	Order of magnitude decrease	Five order of magnitude decrease	Thin

$SiO_{0.7}$ **(Si/SiO_2 60/90)**	~10^8 Ω·cm	Greater than order of magnitude decrease	Five order of magnitude decrease	Thin

Table 4: Summary of SSRM Findings on the Pristine and Cycled Thin-Film Samples

To understand the cause of the irreversible plateau of the co-sputtered electrodes and the impacts of oxygen on the SEI formation of the Si anodes, we characterized the pristine electrodes and electrodes after their first lithiation to 0.55 V (vs. Li^+/Li, hereafter) and held at that potential for 1 h, with duplicate samples lithiated to a lower potential of 0.05 V. The cycled cells were disassembled in an Ar-filled glovebox and rinsed with dimethyl carbonate (DMC) with no exposure to air in the sample transfer process. The samples were first characterized using the SSRM resistivity vs. depth profiling technique [22]. Results summarizing the electronic resistivity of the pristine films, resistivity change from the pristine samples to the 0.55-V lithiated samples, resistivity change from the pristine samples to the 0.05-V lithiated samples, and formed SEI thickness after full lithiation are depicted in Table 4. The pristine samples show the expected result of higher electronic resistivity with higher O content. The change in resistivity from pristine to after lithiation to 0.55 V shows an interesting trend: the two thin films with the lowest O content have a minor decrease in resistivity, whereas the three thin films with nontrivial O content display a significant decrease in resistivity, proportional to the original O content. This result suggests that at 0.55 volts, Si electrodes with oxygen in the bulk undergo a lithiation, whereas lithiation of Si with only surface oxygen does not proceed, resulting in a conductivity enhancement proportional to the original O content. Lithiation to 0.05 V shows a more significant conductivity enhancement for all samples, with a greater conductivity decrease for samples with higher O content. This measured conductivity increase from SiO_x to $Li_xSi_yO_z$ is consistent with experimental results established in the literature [23,24]. SEI thickness after lithiation to 0.05 V was shown to decrease with increasing O content of the pristine electrode.

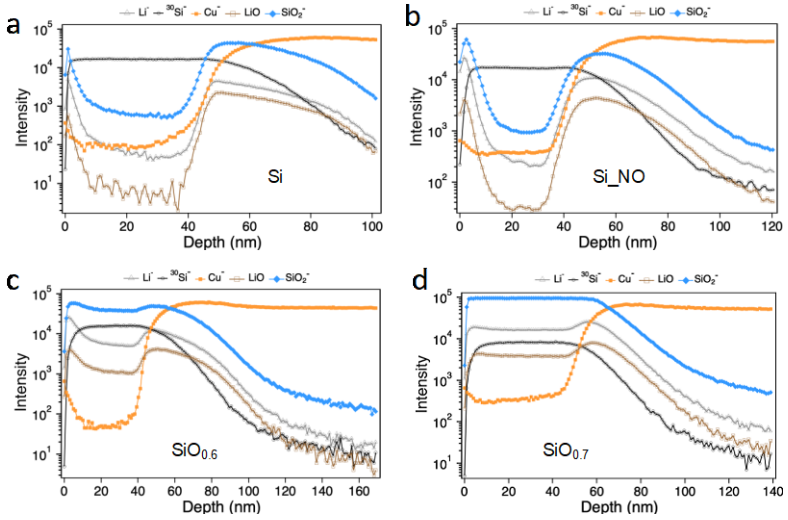

Figure II.1.B.41. TOF-SIMS profiles of the Si, Si_NO, SiO_x (90-60 W) and SiO_x (60-90 W) electrodes after being lithiated to 0.55 V.

Time-of-flight secondary ion mass spectrometry (TOF-SIMS) profiles of the cycled electrodes after lithiation to 0.55 V were collected to further investigate the possible lithiation of electrodes with oxygen in the bulk. As shown in Figure II.1.B.41, the Si and Si_NO electrodes only show Li^-, LiO, and SiO_2^- signal on the surface, which drop quickly along the depth of the samples, revealing that only the surface of these two electrodes contains Li, lithium oxides, and silicon oxides, which should be attributed to SEI. In contrast, both the SiO_x (90-60 W) and SiO_x (60-90 W) electrodes exhibit Li^-, LiO, and SiO_2^- signal throughout the bulk, especially the SiO_x (60-90 W) electrode, which shows steady Li^-, LiO, and SiO_2^- signal along the depth of the sample. This result confirms the lithiation of these two electrodes at 0.55 V, whereas the Si and Si_NO electrodes only contain lithium at the surface, agreeing with the SSRM results. In addition, the presence of LiO signal in the bulk of the SiO_x (90-60 W) and SiO_x (60-90 W) electrodes indicates that the lithiation of silicon oxides would produce lithium oxides.

Table 5: Surface Composition of Cycled Electrodes Obtained from XPS

Atomic composition (%)	C	O	F	P	Si
Si, 0.55 V	19.9	18.3	41.2	2.2	18.4
Si_NO, 0.55 V	36.8	17.0	23.2	2.8	20.2
SiO_x (90-60 W) 0.55 V	37.2	20.1	24.7	1.8	16.2
SiO_x (60-90 W) 0.55 V	25.9	17.0	41.7	1.7	13.7
Si, 0.05 V	56.0	25.4	15.4	0.79	2.47
Si_NO, 0.05 V	41.6	20.1	31.7	1.2	5.5
SiO_x (90-60 W) 0.05 V	36.9	21.8	35.0	1.2	5.1
SiO_x (60-90 W) 0.05 V	64.3	19.6	12.7	1.2	2.2

We further examined the surface properties of the cycled electrodes via XPS. The surface composition of the electrodes after the first lithiation to 0.55 V and 0.05 V is summarized in Table 5. In general, the electrodes lithiated to 0.55 V show lower carbon and oxygen content but higher F, P, and Si content. The much higher Si content suggests a thinner SEI on the electrodes at this potential than those lithiated to 0.05 V as XPS is a surface-sensitive technique, with a sampling depth of 5–10 nm. Because the only source of phosphorous is $LiPF_6$, the relatively high P content of the electrodes at 0.55 V than at 0.05 V indicates that there are more decomposition products from $LiPF_6$ on the surface of the electrodes. After lithiating the electrodes to 0.05 V, the thickness of the SEI increases with a decrease in P and F content and an increase of the C and O content. As the C and O composition is expected to originate from the decomposition of the electrolyte solvent molecules, the change in thickness and composition of the SEI suggests that there is more $LiPF_6$

decomposition in the higher potential range and more electrolyte solvent decomposition in the lower potential range.

Furthermore, in the electrodes lithiated to 0.55 V, the P content decreases as the oxygen content of the electrode increases, indicating that oxygen may help suppress the decomposition of $LiPF_6$. When being lithiated to 0.05 V, the electrodes with lower oxygen content show lower Si content but higher C content, except the $SiO_{0.7}$ electrode. The lower Si content again suggests a thicker SEI of the lithiated electrodes, and the higher C content should be due to more electrolyte solvents decomposition. The deviation of the trend for the $SiO_{0.7}$ electrode indicates that it may have quite different lithiation behaviors from other electrodes. Overall, the surface composition of these electrodes lithiated to different potentials reveals the impact of oxygen content on electrolyte decomposition and formation of SEI.

Role of oxides – silicon wafers

In addition to these studies, we also fabricated custom wafer samples for the whole SEISta multi-institutional team, including wafer samples with specialized formfactors (e.g., rotating disc electrodes), and produced diffused dopant profiles and oxide overlayers. In addition, we designed an O-ring cell, distributed it to other SEISta project labs, and demonstrated the methodology to use it for electrochemistry studies. The research effort of our team focused on the role of SiO_2 overlayers, particularly as possible means to stabilize the SEI formation and evolution during cycling [25,26].

In our contribution to the SEISta project, we performed two systematic studies to elucidate the effect of SiO_2 overlayers on Si anode performance. In the first study, we used thermally grown SiO_2, which is dense and stoichiometric when grown at high T > 700°C, and varied its thickness over a wide range. We established a thickness range of 1–2 nm of thermal oxide as optimal for the Si anode performance boost—in particular, a more stable SEI and good cyclability. Based on this, in the second study, we compared two thin oxides—high-quality thermal oxide and native oxide—to show that the dense, stoichiometric thermal oxide is far superior for Si anode performance boost via controlled SEI and excellent cyclability. These studies resulted in two journal papers published in 2020 [25,26].

Importance of isolation of the Si wafer edges by O-ring cells for accurate electrochemical characterization

Si wafers with SiO_2 coatings must be tested in cells that isolate the wafer edges or rear from the electrolyte. Defining the active area by an O-ring is crucial because the edges are not coated with SiO_2 and are thus initially much more electronically conductive. We designed such a cell (Figure II.1.B.42) and showed that it yields an electrochemical response as expected from the 100-nm-thick, insulating SiO_2 (Figure II.1.B.42a)—a purely capacitive response—whereas the coin cell with exposed wafer edges exhibits electrochemistry as expected from a bare Si wafer (Figure II.1.B.42b). However, a cell with an O-ring uses a larger electrolyte volume, and we found that this can lead to more pronounced side reactions. When only cleaning cell parts in dimethyl carbonate between experiments, galvanostatic cycling at 20 μAcm^{-2} yields continuous electrolyte reduction at voltages far above the lithiation potential. Through a series of experiments, it was found that using fresh Li metal for reference and counter electrodes, using fresh electrolyte, and cleaning cell parts in organic

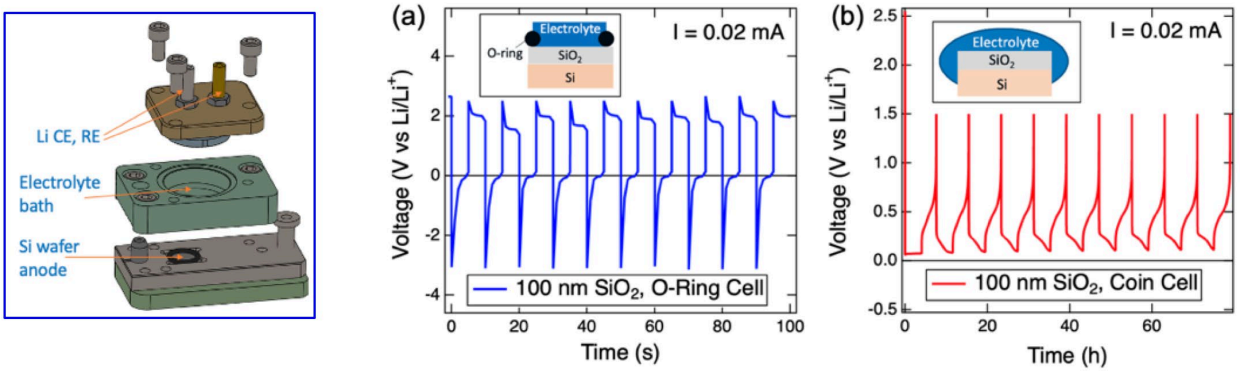

solvents as well as water between experiments was crucial to suppress electrolyte reduction. With this procedure, we are able to achieve lithiation at current densities down to 5 μAcm^{-2}, with ~1.4 mL electrolyte used per cm^2 of anode area, as opposed to ~20 μLcm^{-2} in a typical coin cell. With this approach, we used 20 $\mu A/cm^2$ in our experiments.

Figure II.1.B.42. Left: a detailed schematics of the O-ring cell used in our experiments. Galvanostatic cycling of a Si wafer with 100-nm SiO_2 in (a) a custom cell with an O-ring on the SiO_2 and (b) a coin cell. The O-ring is essential to ensure that only the oxidized surface of Si is lithiated; in a coin cell, the electrode edges can be lithiated (see insets in (a,b)) [25,26].

Effect of high-quality, thermally grown SiO_2 of different thickness

Figure II.1.B.43 shows that there is a striking difference between the oxide thicknesses below 3 nm and above 3 nm. In this experiment, galvanostatic cycling was performed at 20 μAcm^{-2} in Gen2 electrolyte against Li metal counter and reference electrodes with no lower voltage cutoff. In samples with less than 3.0-nm SiO_2, their cycling curves essentially overlap, their coulombic efficiencies are over 99% from the second cycle onwards, and photographs of cycled samples show uniform lithiation. For oxides thicker than 3 nm, we observe localized (pinhole) lithiation and coulombic efficiencies well below 90%.

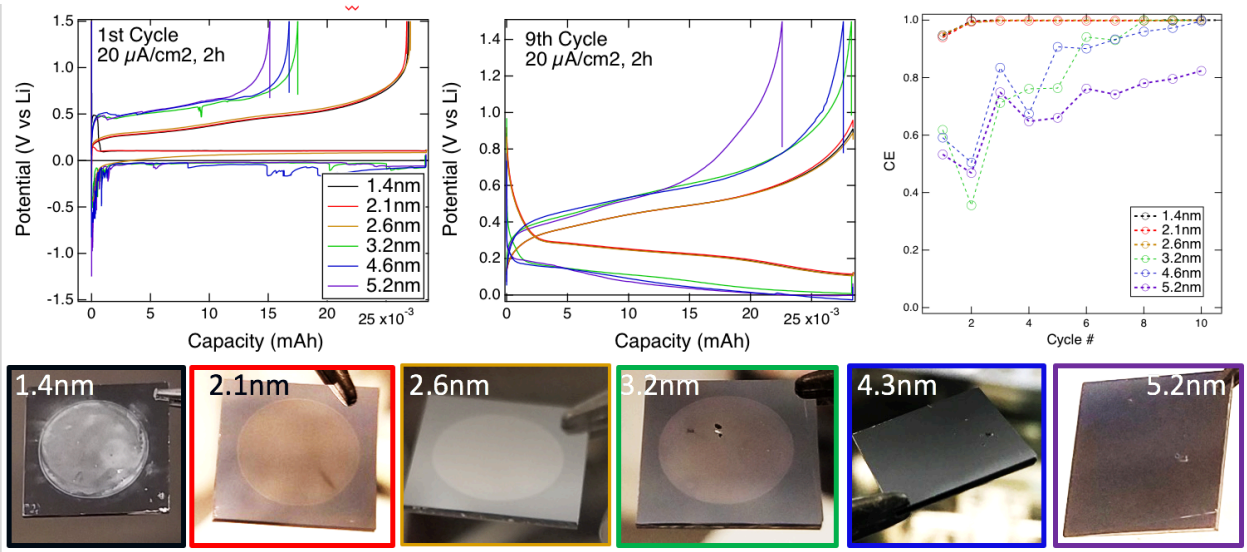

Figure II.1.B.43. Cycling of Si wafer anodes with variation of SiO_2 coating thickness at 20 μAcm^{-2} with no lower voltage cutoff. Top: first and ninth cycles as a function of SiO_2 thickness (left, middle), and coulombic efficiency as a function of cycle number (right). Bottom: Photographs of Si wafers after 10 cycles [25,26].

The pinhole character of lithiation was confirmed and explored by SSRM, TOF-SIMS, and XPS. In this experiment, the anodes were lithiated in half-cells for 70 h at 10 mV up to a current of 200 nA/cm^2 and a total charge of 2.6 $\mu Ah/cm^2$. Figure II.1.B.44 summarizes the microscopic findings and presents our model of pinhole lithiation regime based on the following experimental observations. First, the TOF-SIMS map (Figure II.1.B.44b) shows round, uniformly and heavily lithiated near-surface regions (Figure II.1.B.44c) in the Si wafer, extending ~10 nm deep and ~70 µm in radius. These regions are also seen optically as lighter contrast (Figure II.1.B.44a). These findings indicate that Li^+ ions enter the Si wafer via pinholes, then propagate radially. Surprisingly, the radial propagation is very fast and long-range and consists of two stages: (1) the heavily, uniformly lithiated region ~70 µm in radius and (2) interfacial diffusion of Li over even longer radii ~200 µm. The latter is evidenced by the Li SIMS profile (Figure II.1.B.44d) showing Li present outside the heavily lithiated region (Figure II.1.B.44c). Further evidence comes from the XPS maps (lower left panel of Figure II.1.B.44). There, shifts of O1s peaks consistent with near-interfacial lithiation and n-type doping of the wafer surface causing band bending, extend to over 200-µm radius. This is illustrated by our SIMS maps of Li^+ taken over narrow depth intervals (Figure II.1.B.45; positions shown in Figure II.1.B.44c by gray bands).

Figure II.1.B.45e shows that Li signal in these maps largely disappears at depths deeper than 13 nm. At shallower depth, Li is strongly present in the Li silicide region of ~70-µm radius (see 1-nm depth map).

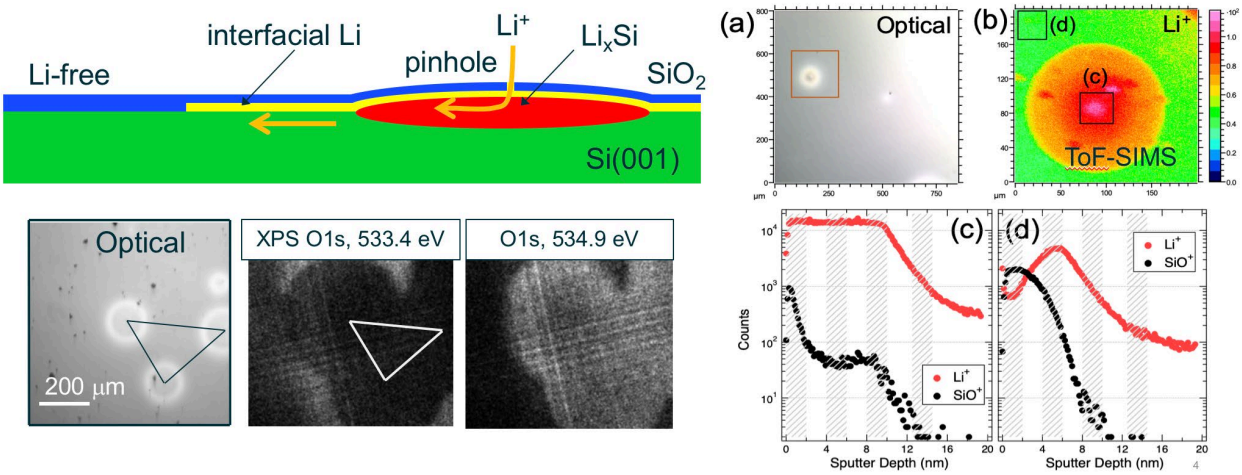

Figure II.1.B.44. Right panel: TOF-SIMS map (b) from the vicinity of a heavily lithiated region shown by a square in the optical image (a) for the 5-nm-thick thermal oxide layer on Si wafer. Bottom right: TOF-SIMS depth profiles from wafer locations (c) near the pinhole center and (d) outside the heavily lithiated region. Note that despite the weak integrated Li signal in SIMS map in location (d), there is a sharp Li peak at the wafer/SiO_2 interface (at a depth of 5 nm). Bottom left: XPS maps of O1s peak at two different electron energies on either side of the peak. The contrast indicates shift of this peak due to interfacial Li. Top left: our model schematics of Li penetration via pinhole in SiO_2 (blue), its rapid interfacial diffusion to ~200 µm (yellow) and formation of Li silicide region ~70 µm in radius (red). TOF-SIMS data from [25,26].

However, at a specific depth of 5 nm (our oxide thickness), Li signal fills the whole map, indicating its rapid interfacial propagation to distances well beyond 70 µm. We observe a similar long-range Li propagation in SIMS maps taken over larger sample size (Figure II.1.B.45, right panel). There, a different sample location was mapped over longer distances. Ones notices different sizes for the optical contrast regions (corresponding to Li-rich regions of Figure II.1.B.44, which we attribute to Li silicide, evidenced by low O content), most likely due to different preexisting pinhole sizes or pinholes being continuously formed upon lithiation. The integrated Li maps over the 500-µm sample area clearly shows Li propagation to distances a few times longer than the Li silicide regions, >100 µm, in agreement with O1s peak shift XPS maps of Figure II.1.B.44. Notably, the C- and P-related signals corresponding to the formed SEI and are restricted to near the center (c) of the lithiated region near the pinholes. On other hand, SiO^+ signal associated with SiO_2 appears relatively intact across the sample, indicating that the integrity of the oxide is preserved except for the near the larger pinholes.

To summarize the oxide thickness effect, we observe two distinct regimes. At thermal SiO_2 thickness below 3 nm, the lithiation proceeds uniformly with coulombic efficiency close to 100% and stable cycling performance. As the oxide thicknesses increases over 3 nm, lithiation electrochemistry occurs via pinholes in the oxide. The origin of these pinholes is still not fully understood, but they are likely associated with electric breakdown and "weak" spots in the oxide layer. Li ion penetration also might play a role in pinhole formation. In the pinhole regime, Li exhibits remarkably fast interfacial diffusion, forming thin, circular Li-containing "platelets" up to hundreds of microns in diameter, whereas the $LiSi_x$ region extends only ~10 nm deep into the wafer. These platelets consist of two distinct phases: a $LiSi_x$ region ~50 microns in radius, lithiated uniformly down to ~10 nm in 70 h, and interfacial Li-containing outer regions, where Li is at the wafer/oxide interface. The latter interfacial Li extends as far as ~200 µm from the pinhole center, far beyond the $LiSi_x$ platelet. As Li spreads radially along the Si/SiO_2 interface, ~100 microns in 70 h, its effective interfacial diffusion coefficient is ~10^{-9} cm^2/s, which is 10^3–10^4 times greater than the bulk diffusion of Li in Si and SiO_2.

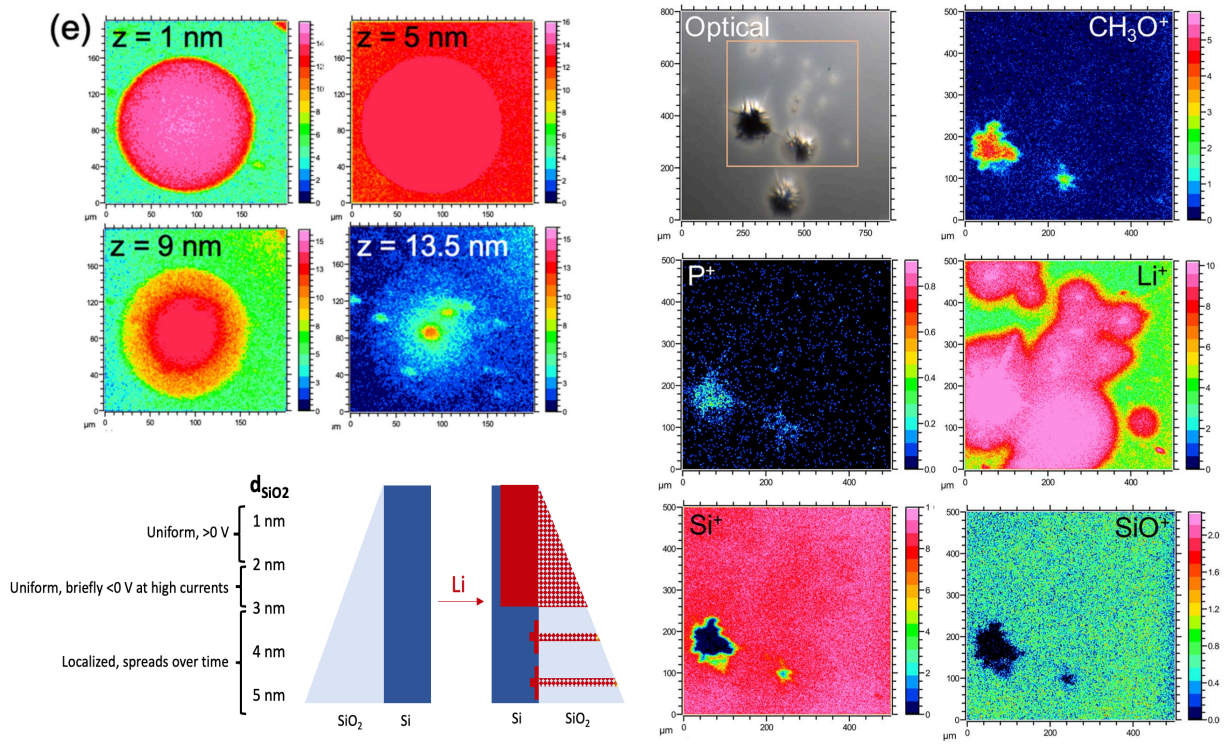

Figure II.1.B.45. Left panel: TOF-SIMS Li^+ maps from the sample of Figure II.1.B.41, integrated over narrow depth intervals shown in Figure II.1.B.41 depth profiles (c) and (d) by gray bands. Right: TOF-SIMS maps of several species from a different sample location than Figure II.1.B.41, showing several pinholes with Li silicide regions formed around them (optical image). Bottom: brief summary of our observations of Si lithiation mechanism as a function of thermal SiO_2 overlayer thickness [25,26].

Thin thermal oxide layer improves the performance of Si anode

To examine the oxide layer protective properties further, we focused on the uniform lithiation regime and chose thermal oxide thickness 1.4 nm, thermally grown at 850°C in a tube furnace. This was compared with 1.3-nm native oxide and "no oxide" on the Si wafer (the preexisting SiO_2 was removed by an HF dip). Figure II.1.B.46 compares their electrochemical responses.

The oxide-free Si wafer performs the worst: it has low coulombic efficiency of about 94% that does not improve with cycling, and large overpotentials for lithiation. The wafer with native oxide has lower overpotentials and significantly higher coulombic efficiency starting from the second cycle; however, the CE drops beyond the fifth cycle. With more detailed analysis, we identified two types of electrolyte reduction processes in the first cycle: A and B for the two oxidized wafers, and A' and B' for the oxide-free wafer (see the inset in Figure II.1.B.46).

Thermal and native oxide have similar processes A, B. Cao et al. [28] associated process A with LiF formation, B with Li_2O. Yin et al. [27] also assigns A to LiF, whereas B is associated with C-O groups. To correlate these processes with particular electrolyte reduction chemistries, we used XPS. Our XPS study did not detect any Li_2O signal in the early-stage SEI formation (es-SEIs), so we identify process B with solvent reduction, most likely the EC reduction. As for process A, we see clear LiF signal and P-F signals in the SEI layer. Therefore, we assigned A to the $LiPF_6$ reduction. Processes A' and B' are essentially the same as A and B (supported by the same evidence from the XPS), but occur at higher potentials than A, B. A' and B' occur at the theoretical reduction potentials for these processes, and the oxide layers suppress the electrolyte reduction potential values significantly.

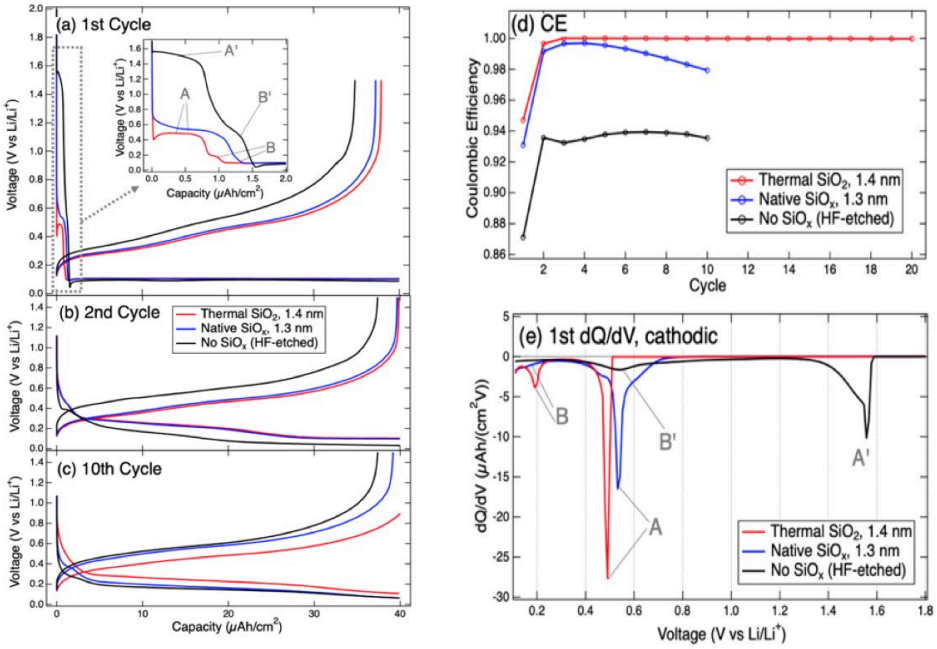

Figure II.1.B.46. Galvanostatic cycling of Si wafers with three states of surface oxidation. (a) First cycle, with enlarged start of the cathodic half-cycle at the inset; its differential capacity dQ/dV is shown in (e). (b) Second cycle. (c) Tenth cycle. (d) Coulombic efficiency [25,26].

The electrolyte reduction is strongly suppressed for the thermal oxide wafer in the second and subsequent cycles, while it continues for the non-oxide wafer and the native oxide wafer. In Figure II.1.B.47 (left), we show the integrated charge (from the differential capacity plots dQ/dV) consumed by the electrolyte reduction as a function of cycle number. The charge approaches nearly zero for the thermal oxide by the tenth cycle, but stays high for no-oxide and native oxide wafers. This correlates with the low CE for those wafers in Figure II.1.B.44. Furthermore, the XPS shows, by the height of the substrate Si peak, that the SEI grows thick on the non-oxidized wafer (see Figure II.1.B.47, right) but thinner for the oxidized wafer.

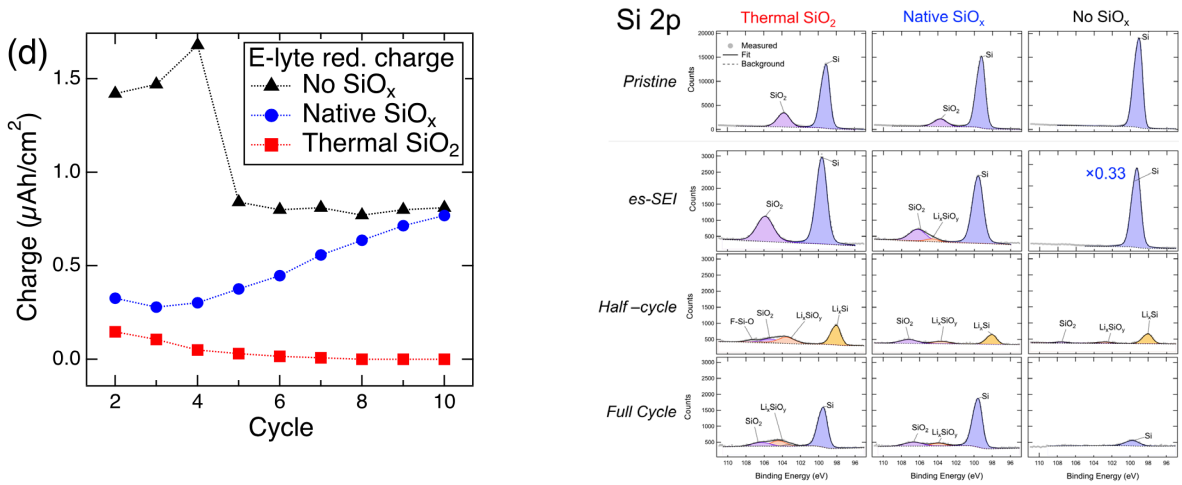

Figure II.1.B.47. Left: The charge consumed by the electrolyte reduction process in cycles 2–10, determined by peak integration in dQ/dV curves. Right: Si peak reduction measured by XPS, due to SEI formation in three stages of the first cycle: early-stage SEI, half-cycle, and full cycle. Strong and irreversible reduction of Si peak, associated with formation of a thick SEI, is evident in the non-oxidized wafer [25,26].

To summarize our work on the different oxide comparison, we found that 1.4-nm-thick, dense, stoichiometric thermal oxide significantly improves the Si anode performance. Its coulombic efficiency remains ~99% over 20 cycles, and the electrolyte reduction is suppressed by a stable, well-formed SEI. The native oxide initially exhibits high CE, but the electrode reduction is not suppressed with cycling, likely indicating poorer and less stable SEI. Finally, the oxide-free Si performs the worst, exhibiting persistently low CE ~94%, large charge consumption due to electrode reduction upon cycling, and uncontrolled growth of the SEI.

Electron microscopy of the SEI over silicon oxides

Five samples with the different O content were characterized using the SSRM resistivity vs. depth profiling technique (profiles not shown): the pure Si electrode contains low surface oxygen (9.3 at. % O, referred as Si), a native oxide layer formed on the Si thin film (Si_NO) by exposing the film in air, SiO_x films prepared by co-sputtering under the power combinations of 90 W for Si target and 30 W for SiO_2 (SiOx_1), 90 W and 60 W ($SiO_{0.6}$), and 60 W and 90 W ($SiO_{0.7}$). Different power ratios between targets result in roughly proportional concentrations in the sputtered material. Table 4 summarizes the electronic resistivity of the pristine films, resistivity change from the pristine samples to the 0.55-V lithiated samples, resistivity change from the pristine samples to the 0.05-V lithiated samples, and the formed SEI thickness after full lithiation. The pristine samples show the expected result of higher electronic resistivity with higher O content. The change in resistivity from pristine to after lithiation to 0.55 V shows an interesting trend: the two thin films with the lowest O content have a minor decrease in resistivity, whereas the three thin films with nontrivial O content display a significant decrease in resistivity, proportional to the original O content. This result suggests that at 0.55 volts, Si electrodes with oxygen in the bulk undergo lithiation, whereas lithiation of Si with only surface oxygen does not proceed, resulting in a conductivity enhancement proportional to the original O content. Lithiation to 0.05 V shows a more significant conductivity enhancement for all samples, with a greater conductivity decrease for samples with higher O content. This conductivity measurement is consistent with the increase from SiO_x to $Li_xSi_yO_z$. SEI thickness after lithiation to 0.05 V was shown to decrease with increasing O content of the pristine electrode.

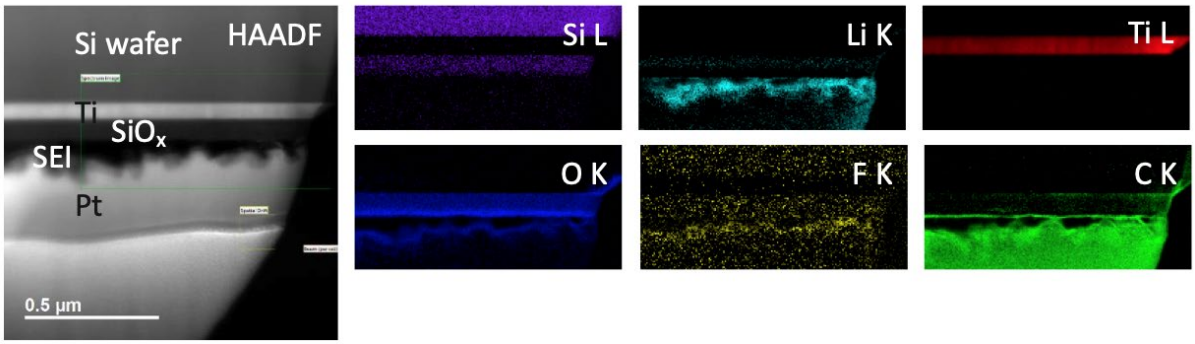

Figure II.1.B.48. STEM HAADF image and EELS edge elemental maps showing the layer structure and distribution of Si, Li, Ti, O, F, and C in a model SiO_x electrode lithiated to 0.05 V.

STEM analysis has been performed on both the pristine $SiO_{0.7}$ and after lithiation to 0.05-V $SiO_{0.7}$ electrodes. The pristine sample showed the expected deposited layer structure. After lithiation to 0.05 V, STEM EDS and

EELS elemental mapping revealed the formation of a non-planar SEI layer of thickness 70–140 nm. The SEI layer was found to contain Li, O, C, and F as observed by EELS elemental mapping (Figure II.1.B.48).

2. Role of binder and formation of the SEI

Binders are one critical component that works directly with Si particles and plays an important role of providing strong adhesion/cohesion between the active materials (graphite and/or Si), conductive additives, and the current collector [27-29]. Whereas the traditional PVDF binder does not work well with Si-based electrodes due to its relatively low stiffness and poor adhesion [30,31], hydroxy-containing polymers including sodium alginate [32], sodium carboxymethyl cellulose [30], poly(vinyl alcohol) [33], xanthan gum [34], and PAA [35] have demonstrated promising cycling performance for silicon anodes [36]. These polymers appear to have stronger binding strength, possibly because they tend to form hydrogen or even covalent bonding with the siloxyl groups (Si-OH) that are often found on the surface of Si particles [28,29,37]. Among these binders, PAA-based polymers are particularly attractive due to their low cost, facile synthesis, and excellent cycling performance [35,38-40]. Pre-lithiation of PAA (PAA-Li) binders is an important yet not fully understood process that brings in contradicting effects on Si-based anodes, such as improved rheology properties and undermined cycling performance. Although we have established the cycling metrics over Si anodes using various pre-lithiated PAA binders [39], a still better understanding of the impacts on SEI formations is highly desired to inspire possible solutions toward the critical challenges of Si anodes, such as cycling life and calendar life. To this end, we revisited our systematical studies of pre-lithiation of PAA binders and identified previously overlooked correlations between binders and SEI formations. It is noted that a Si-Gr composite electrode containing 73 wt % graphite, 15 wt % silicon (70–130-nm NanoAmor), 10 w t% binder, and 2 wt % C45 is used in this report.

As shown in Figure II.1.B.49a, the pre-lithiation of PAA binders not only causes dramatic fluctuation of pH values, but also results in huge differences in cycling performance of the fabricated cells. Specifically, the dependence of PAA-Li is reminiscent of the textbook strong base–weak acid titration curve, and the added LiOH affords much more ionized binders that bear less protons but more Li^+. Such changes prodoundly affect the overall properties of the binder solutions and slurries. As shown in Figure II.1.B.49b and II.1.B.49c, the fabricated cells demonstrate very different cycling perfomrance. The pre-lithiation leads to more aggressive capacity fading. As preliation of PAA becoms dominating and pH (indicated in notations [e.g., PAA-2.1 is the sample with pH 2.1]) increases, the cell performance underperforms with less initial capcity, worse capacity rententions, and lower coulombic effciencies. Such observation implies there are underlying causes asscociated with the PAA pre-lithiation process.

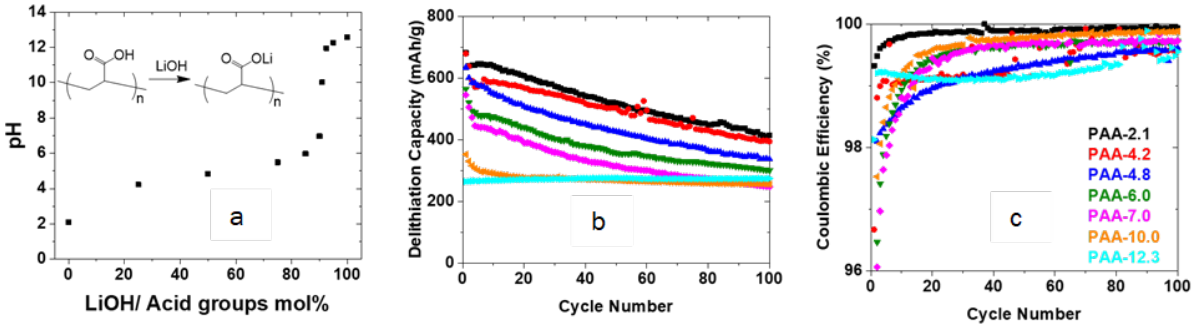

Figure II.1.B.49. (a) pH profiles of PAA-LiOH titration, (b) specific discharge capacity profiles, and (c) coulombic efficiency profiles of half cells using the pre-lithiated PAA binders over 100 cycles at C/3 rate.

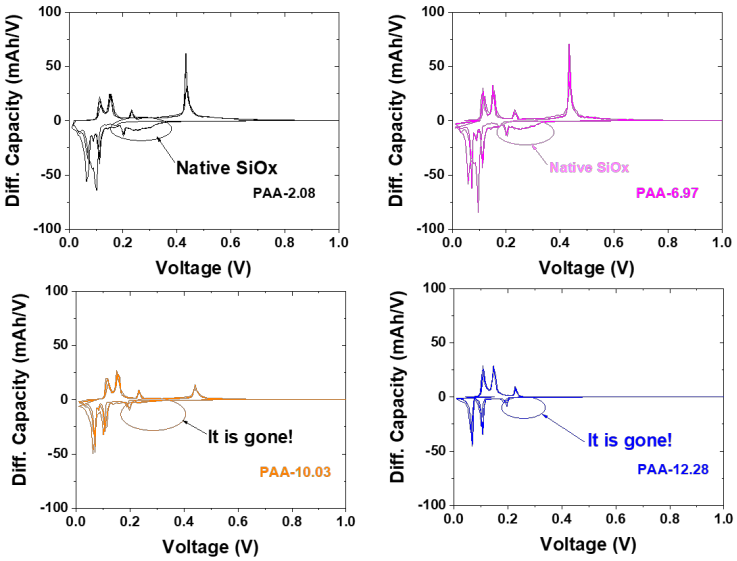

Figure II.1.B.50. Differential capacity (dQ/dV) profiles of half cells containing Si-Gr composite electrodes using PAA-Li binders during the formation cycles at a C/20 rate. The pH of the PAA solutions in Figure 1 is indicated in each panel.

As shown in Figure II.1.B.50, differential capacity profiles of half cells fabricated using lithiated PAA binders reveal the changes of the electrochemical reactions during formations. While peaks associated with graphite are presented in all the plots, certain peaks show huge differences. With less lithiated PAA binders bearing pH < 7, we observe a broad peak at approximately 0.23–0.33 V, indicating a layer of SiO_x formed on the Si anode surfaces. However, as lithiation increases and pH reaches 10 and above, the SiO_x peak becomes absent, implying the more lithiated PAA binders may help to erode the native SiO_x.

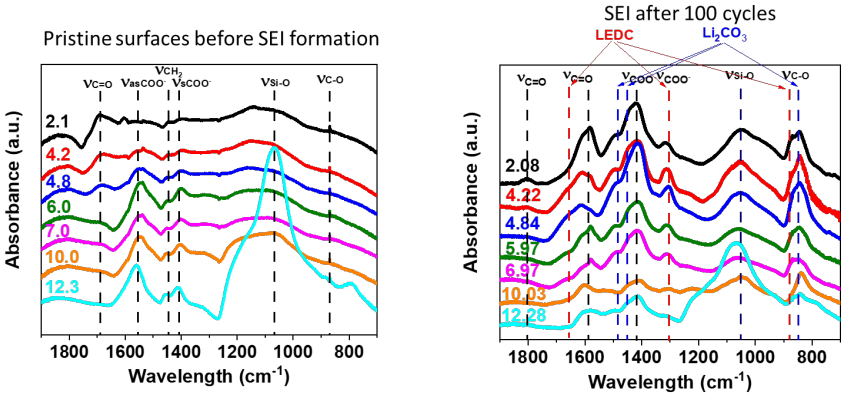

Figure II.1.B.51. SEI species evaluation: FTIR spectra of pristine (left) and cycled (right) electrodes.

FTIR spectra further reveal such changes with more in-depth information. Figure II.1.B.51 complies the FTIR spectra of the pristine and cycled electrodes (after 100 cycles) from half cells using various lithiated PAA binders. The pristine electrodes show a huge SiO_2 peak with binders bearing basic conditions (pH > 10), indicating such binder conditions promote SiO_2 formation as Si is more readily to react with water under basic conditions [27]. On the other hand, on the surface of cycled electrodes, lithium ethylene dicarbonate (LEDC) (1,490, 1,451 and 875 cm^{-1}) and Li_2CO_3 (1,653, 1,400, 1,315, 1,100 and 825 cm^{-1}) are more pronounced at acidic or neutral conditions with pH ≤ 7.

Differential capacity profiles indicate the acidic conditions with less lithiation of PAA may help to preserve the native SiO_x layers of Si particles, whereas FTIR spectra imply basic conditions with pH >10 promote the SiO_2 formation. After extensive cycling, FTIR reveals less pre-lithiation with acidic condition (pH < 7) of binders favors LEDC and Li_2CO_3 formations, two components that are required for stable SEI layers. Although many efforts are needed toward understanding, these findings reveal strong correlations between binder alternation and SEI formation.

Surface sensitive microscopy and influence of binder

SSRM 3D resistance mapping was conducted on two Si nanoparticle-based composite electrodes: one is a surface-engineered Si (SE-Si) containing Si, carbon nanotubes as the conductive carbon material, and PAA binder. The intrinsic Si (i:Si) electrode contains i:Si, graphite, and PAA. SE-Si and i:Si electrodes were lithiated/delithiated to 100 and 500 cycles, respectively. The results (Figure II.1.B.52) show highly nonuniform resistivity due to the multiple phases in the electrode. Individual Si nanoparticles could not be resolved because of their small sizes of ~6 nm. Instead, larger agglomerates of the particles were probed. Figure II.1.B.52e shows a histogram of the resistivity distribution in the four pristine and cycled anodes. The resistivity of pristine SE-Si in the analyzed area shows primarily two distinguishable phases, probably due to carbon nanotubes and SE-Si. In the pristine i:Si sample, the graphite phase dominates the analyzed area, along with the i:Si and PAA phases, likely contained in the long tail on the right of the histogram. With cycling, the resistivity maps show significant increases of high-resistivity phases on both the anode surface and in the bulk, indicating the formation and ingress of SEI. This resistivity increase occurs much more in the SE-Si sample than the i:Si sample, although SE-Si had been cycled (100 cycles) much less than i:Si (500 cycles), likely due to the much more Si phase present that resulted in more volume expansion and more subsequent SEI ingress and active material fouling.

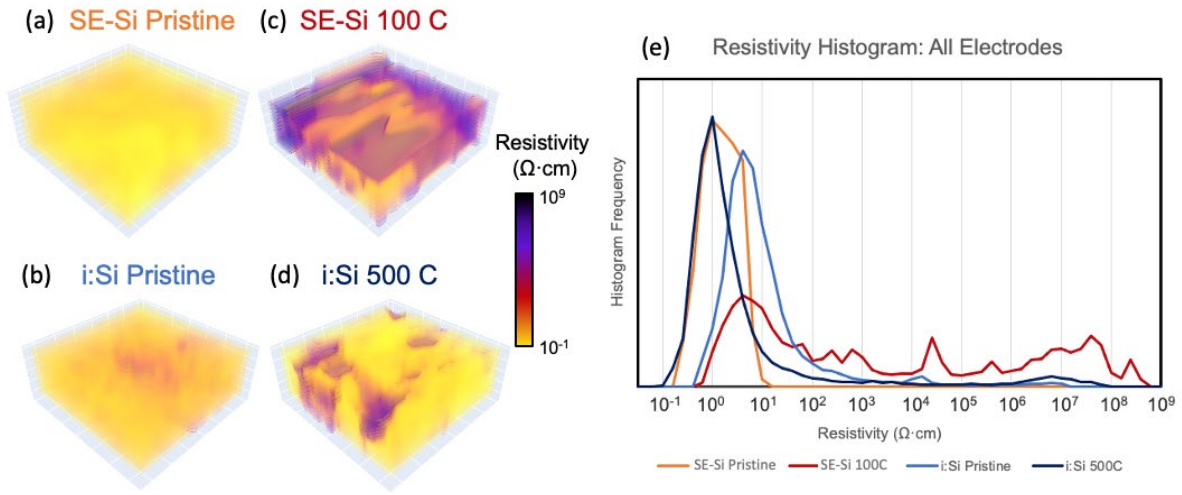

Figure II.1.B.52. 3D resistance mapping on (a),(c) SE-Si and (b),(d) i:Si anodes at (a),(b) pristine and (c),(d) cycled states. (e) Histograms of resistance of the four samples.

By approximately defining the resistivity range of the different phases (Figure II.1.B.53a), 3D distribution of the phases can be identified from the resistivity mapping. One example of cycled SE-Si is shown in Figure II.1.B.53b, where the more- and less-resistive phases were drawn with significant weights of all the phases (Figure II.1.B.53).

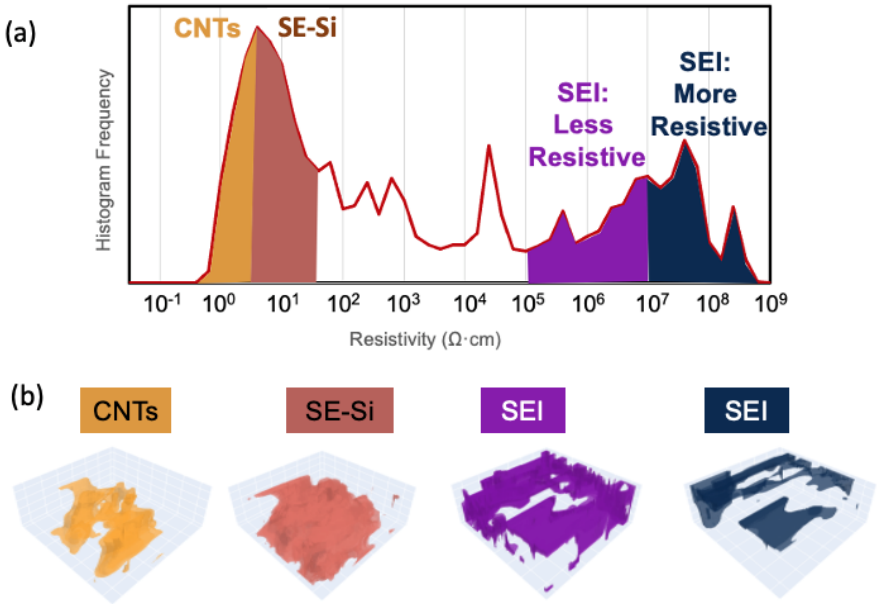

Figure II.1.B.53. (a) A histogram of the SE-Si after 100 cycling and related resistivity definition of the phases; (b) 3D identification of the multiple phases derived from the 3D resistance mapping.

3. New electrolytes and understanding the SEI formation

Glyme electrolytes

The conversion type of Si anode shows almost 10-times larger specific capacity than the conventional graphite anode. However, the commonly used carbonate-based electrolytes (e.g., standard Gen2 electrolyte—$LiPF_6$ in an EC/EMC mixture) that have been widely used to stabilize the carbonaceous anodes have been found incapable of stabilizing the Si anodes. It is partially ascribed to the non-passivation behavior of carbonate-based electrolytes. Even with the best-performing carbonate electrolyte with addition of a fluorinated carbonate additive, FEC, a finite parasitic or leakage current always exists per our previous corrosion-related reports on a-Si anodes. One possible explanation is that due to the severe volumetric change of Si upon lithiation/delithiation, the sustained reaction between the electrolytes with freshly exposed silicon surface leads to an unstable SEI with the thickness increasing. One method to solve this issue is to explore solvents and salts other than commonly used carbonate-based electrolytes for Li-ion batteries that could potentially demonstrate better passivating properties on Si. Earlier study by our team investigating SEI formation on amorphous silicon (a-Si) thin film indicates that polymeric ether components such as poly(ethylene oxide) (PEO) are formed during the first couple of GCs [41], enabling certain viscoelasticity of the SEI to buffer the volumetric change of the Si anodes. Glyme is a type of under-evaluated electrolyte solvent for Si anode. The rational of using glyme is it has similar chemical structure as the PEO in SEI. A series of glyme-based electrolytes are thus being explored for their effects on the SEI formation using a model a-Si thin film anode at ORNL. We have shown in our previous reports that a type of glyme electrolyte containing lithium bis (fluorosulfonyl) imide LiFSI-DME, and a fluoroadditive, 1,1,2,2-tetrafluoroethyl-2,2,3,3-tetrafluoropropyl ether (TTE) can better stabilize the a-Si thin-film anode after extended GC. We show that the a-Si thin-film anode with a certain combination of the LiFSI, dimethoxyethane (DME) and fluorinated ether, fluoroether, 1,1,2,2-tetrafluoroethyl-2,2,3,3-tetrafluoropropyl ether (TTE) (denoted as LiFSI-3DME-3TTE) outperforms the best-performing carbonate electrolyte (Gen2 + 10 wt % FEC). A 50-nm amorphous (a-Si) thin-film anode was used as the model anode and lithium metal was used as a counter electrode. When using 1C equivalent rate GC test, the capacity retention for Gen2 in first 110 GC cycles was around 30%, whereas this value of the glyme electrolyte reached close to 89%. Preliminary characterization based on infrared spectroscopy indicates that the SEI on a-Si surface possibly has rich polymeric ether-based species. However, chemical details of thus-formed SEI and the role the polymeric ethers to stabilize the a-Si anode still remain largely elusive. We further consolidate the surface chemistry of the cycled a-Si using energy dispersion EDS and XPS. The topography of the a-Si cycled in different electrolytes is evaluated by the SEM micrographs.

Here, Gen2 electrolyte was used as a benchmark. The surface morphology of both early-stage cycling (denoted as 5 cyc) and prolonged cycling (110 cyc) are of interest. For the first 5 cycles, a-Si cycled in both Gen2 and 1-3-3 (LiFSI-DME-TTE molar ratio as 1:3:3) electrolytes exhibits cracks on the SEI, as shown by both the SEI micrographs and the EDS mapping of oxygen and carbon in Figure II.1.B.54. Further investigation on the EDS mapping of Si shows that those cracks may stem from the volumetric change of the a-Si thin film upon (de)lithiation. The EDS mapping of the Cu substrate provides complementary proof toward this point. After prolonged GC, a-Si in Gen2 electrolyte exhibits more distinguished crack pattern, as demonstrated by both the SEM micrographs and the O and Si EDS mappings.

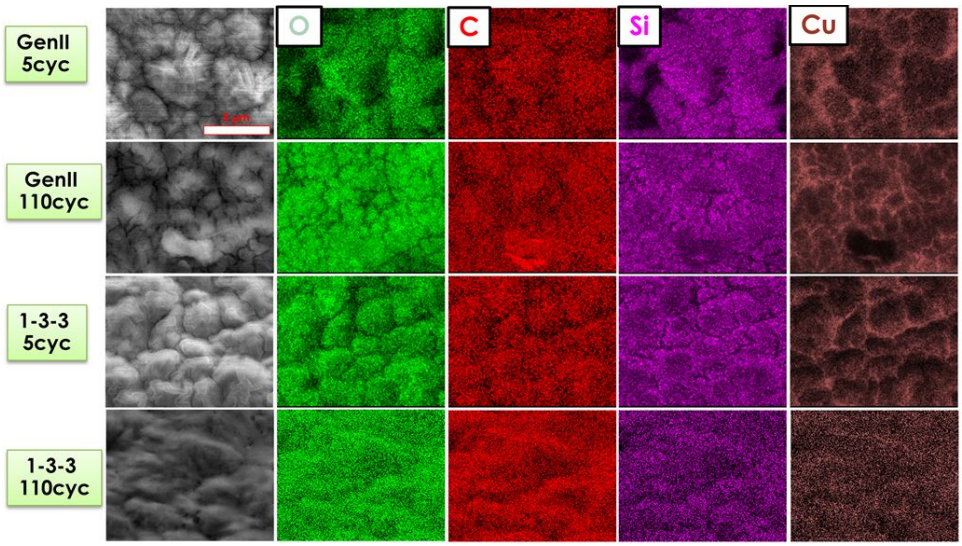

Figure II.1.B.54. SEM micrographs (left column) of cycled a-Si in different electrolytes for various cycle numbers. The EDS mapping of several elements on the corresponding scanned area by SEM are shown on right columns.

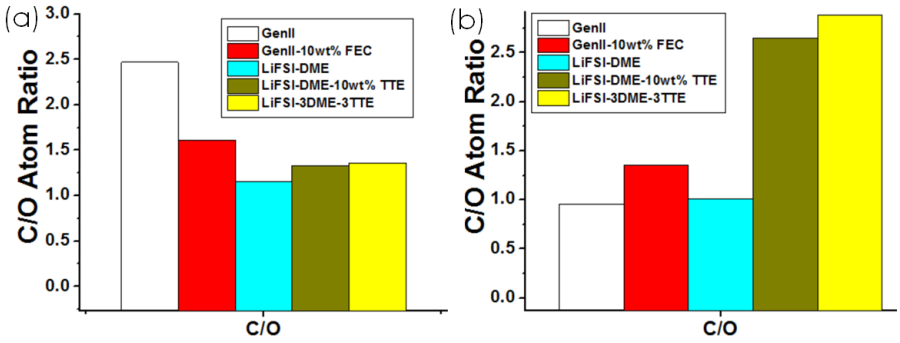

Figure II.1.B.55. The elemental molar ratio of the C/O analyzed based on the EDS mapping on a-Si anodes for various electrolytes after (a) 5 cycles and (b) 110 cycles.

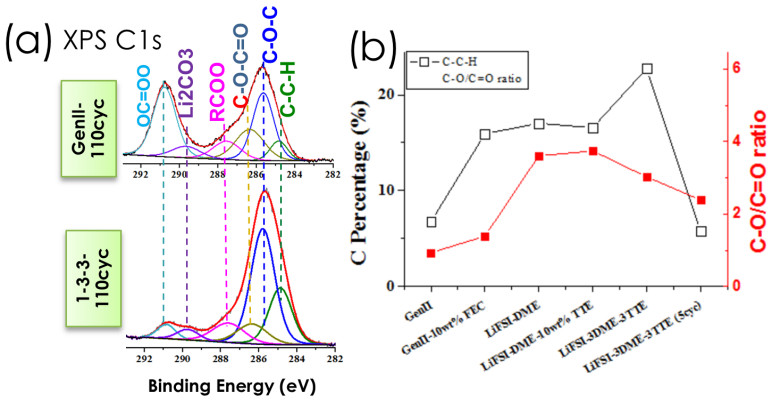

Figure II.1.B.56. (a) C 1s XPS spectra of the a-Si anodes cycled for 110 cycles in Gen2 and 1-3-3 glyme electrolytes. (b) The concentration of the C—C-H and the molar ratio of the C-O/C=O for various electrolytes.

The C/O ratio is important because two main polymeric species in SEI, namely polymeric carbonate (-COO) and polymeric ether (-COC) have different C/O ratios. This ratio serves as an initial indication of the concentrations of the carbonate and ether functional groups. Seen from Figure II.1.B.55, a-Si in Gen2 electrolytes exhibits high C/O ratio in the early GC stage, whereas the C/O ratio of the a-Si anodes cycled in

glyme electrolytes with TTE additive outperforms those cycled in carbonate electrolytes, indicating the increase of the polymeric ether species in SEI. To further solidify this statement, XPS measurements were performed on a-Si cycled in different electrolytes (Figure II.1.B.56). It is manifest from the C 1s core-level XPS spectra after prolonged GC cycling that ether carbon dominates over other species in the SEI with 1-3-3 glyme electrolyte. In contrast, the SEI of the a-Si anode from Gen2 electrolyte enriches in carbonate species. The C-O/C=O on a-Si surface with the 1-3-3 glyme is 3.2 times that with Gen2 electrolyte. The aliphatic chains (C-C-H) have the highest concentration for a-Si with 1-3-3 glyme electrolyte at 22.8%, whereas it was only 6.7% for a-Si cycled in Gen2 electrolyte. Taken together, the SEI on a-Si anode with 1-3-3 glyme electrolyte has rich polymeric ether species, which are quite possibly PEO oligomers. It is also interesting to notice that at early GC stage (5 cyc), the abundance of the ether function group is low on a-Si with 1-3-3 glyme electrolyte, agreeing very well with the EDS analysis in Figure II.1.B.41. It also corresponds to the observation that when cycled in glyme electrolytes, a-Si anode was much less stable due to the large parasitic current (corrosion test using LBNL's protocol shown in a previous quarterly report) compared with Gen2 electrolyte.

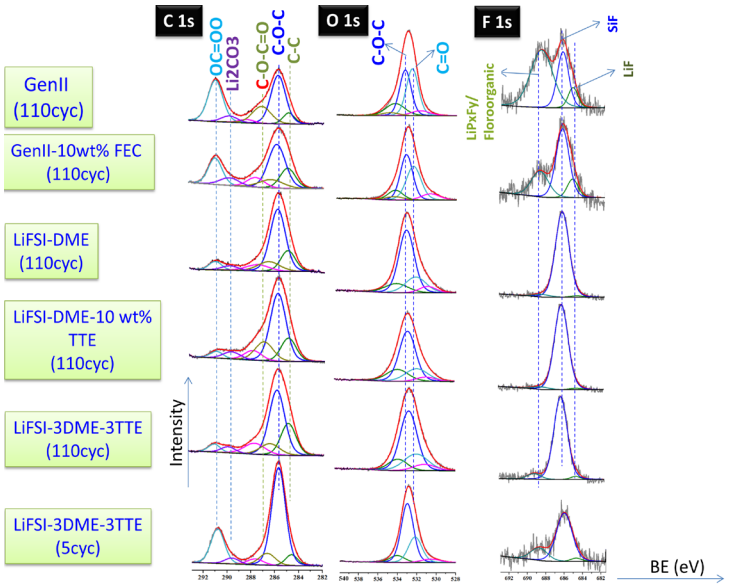

Figure II.1.B.57. Variation of XPS spectra of the a-Si thin-film anodes cycled in carbonate and glyme electrolytes at three different core levels.

A more comprehensive comparison of the surface chemistry among a-Si anodes cycled in various electrolytes characterized by XPS is shown in Figure II.1.B.57. The SEI formed on a-Si from both carbonate and glyme electrolytes have complicated chemical conformations. The first chemical difference between the carbonate SEI (denoted as c-SEI) and the glyme SEI (denoted as g-SEI) worth noting lies in the peak at 290.8 eV. This peak represents the C 1s core level of the carbonyl carbon in carboxylate compounds (OCOO) [21]. The intensity of this peak is noticeably larger in c-SEI from both Gen2 and Gen2 10 wt % FEC after 110 GC cycles than in the g-SEI counterparts. Interestingly, g-SEI on a-Si cycled for 5 times (5 cyc) in LiFSI-3DME-3TTE electrolyte exhibits higher carboxylate abundance than its 110 cyc counterpart. Regardless, the C 1s core level of the ether oxygen centered at 285.7 eV [42] shows a larger intensity than the carbonyl carbon peak for all g-SEIs. This statement is further corroborated by the O 1s core level. The ether oxygen O 1s at 533.0 eV has a comparable intensity with the carbonyl oxygen at 531.9 eV for c-SEI of the Gen2 (110 cyc) sample. Whereas the ether oxygen O 1s peak intensity of the c-SEI is only slightly larger than carbonyl O 1s peak for the Gen2-10 wt % FEC (110 cyc), the former overweighs the latter for all g-SEI samples. Taken together, it clearly demonstrates that the g-SEI has more ether functional groups than its c-SEI counterparts. Fluorinated species is another group of SEI compounds worth exploring. Shown in the right column in

Figure II.1.B.57, the c-SEI for Gen2 (110 cyc) has enriched LiP_xF_y components stemmed from the decomposition of the $LiPF_6$ salt [43]. The resultant fluorinated species has been found responsible for instability of the c-SEI [44] Addition of the 10 wt % FEC decreased the abundance of the LiP_xF_y component (F 1s core level at 688.7 eV) [45], agreeing with other studies in which the FEC reductive decomposition at the Si surface aids in forming a better and more stable SEI layer [46], further mitigating the $LiPF_6$ salt reduction. Lacking $LiPF_6$ salt, the intensity of the 688.7 eV F 1s core level peak for g-SEI drops significantly. Notably, when cycled in LiFSI-3DME-3TTE electrolyte for 5 cycles, there is a shoulder at 688.7 eV for F1s core level. This may be ascribed to the aliphatic fluoroorganic species derived from the polymerization of the glyme electrolyte components. According to [47], the peak centered at 686.3 eV is ascribed to Si-F moieties. This indicates that both c-SEI and g-SEI contain abundant fluorinated silicon species. However, for glyme-based electrolytes, the abundance of the fluorinated species was not increased upon adding more TTE. This suggests that the resource of the fluorinated species in the SEI layer on a-Si may stem from the decomposition of the LiFSI salt instead of the TTE additive.

Figure II.1.B.56b details the relative abundance of a few polymeric moieties in the SEI layer stemmed from both carbonate and glyme electrolytes. The aliphatic C-C backbone counts for 7% for Gen2 electrolyte, but it is more than doubled for Gen2 10 wt % FEC, LiFSI-DME, and LiFSI-DME 10 wt % TTE, suggesting the existence of more than doubled polymeric species. For LiFSI-3DME-3TTE, this value is further increased to 23%, demonstration that even more polymeric components are derived for g-SEI in this case. Focusing on the C-O/C=O ratio (r), the g-SEI exhibits >12.5% r value, whereas r is <5% for c-SEI. Taken together, the g-SEI contains more than twice as much CH_2-CH_2-O repeating unit with respect to inorganic carbonate or carboxylate (C=O) compounds compared to c-SEI counterparts.

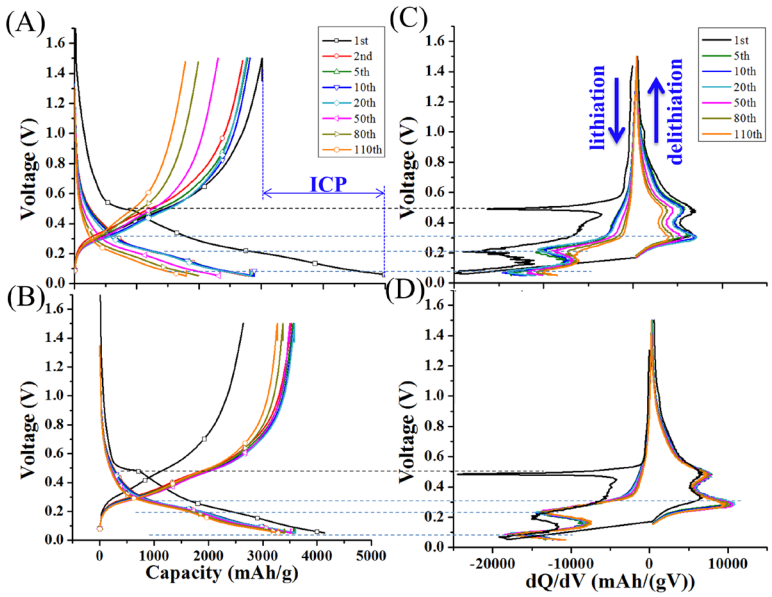

Figure II.1.B.58. Galvanostatic charge/discharge curves for a-Si anodes cycled in (A) LiFSI-DME and (B) LiFSI-3DME-3TTE. The corresponding differential capacity plots are shown in (C) and (D), respectively.

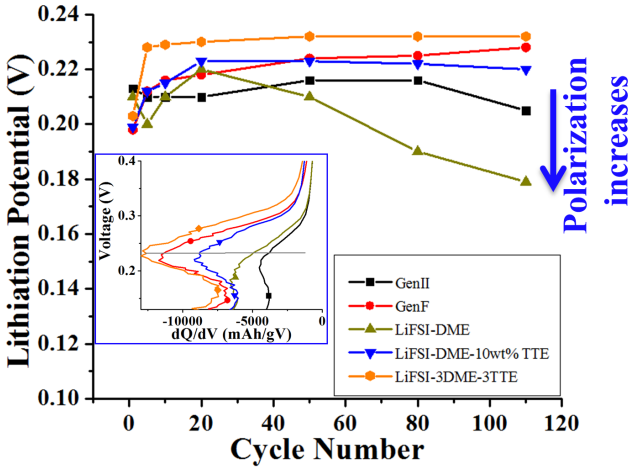

Figure II.1.B.59. The lithiation potential as a function of cycle numbers for a-Si anodes cycled in various electrolytes.

Electrochemical evaluations were further performed to evaluate the a-Si anodes cycled in carbonate and glyme electrolytes. Two types of representative long-term charge-discharge profiles of the glyme electrolytes with and without TTE are shown in Figure II.1.B.58 (A-B). Notably, the lithiation capacity of the initial cycle for LiFSI-DME is 4,975 mAh/g, larger than its Gen2 counterpart. These values are even higher than the theoretical lithiation capacity of Si (4,200 mAh/g), indicative of the side reaction occurrence during the first lithiation. This observation is further evidenced by the partial differential capacity curve shown in Figure 5(C-D), where a sharp irreversible lithiation peak shows at ~0.49 V vs. Li^+/Li in the first cycle, >0.2 V above the a-Si lithiation potential, ascribed to the electrolyte reduction to form initial SEI layer and reduction of the surface SiO_x species [48]. These side reactions result in a large initial irreversible capacity loss of 39.7% for LiFSI-DME and 27.6% for Gen2. The initial inductively coupled plasma (ICP) value is important to estimate additional lithium loss to unveil a more accurate n/p ratio for practical design of Li-Si batteries. For glyme electrolytes, addition of TTE additive decreases the ICP to 36.4% for the LiFSI-3DME-3TTE electrolyte. On the contrary, addition of 10% FEC leads to ICP increasing to 32.8% versus Gen2 for carbonate electrolyte, agreeing with the higher parasitic current at early cycles for GenF in GC-CA test (2019 Q2 report). After the first cycle, the delithiation capacity is slightly increased and stabilized until around tenth cycle, followed by continuous fading to a certain value at the ending cycle, indicating the SEI layer constantly evolving as cycling prolongs. The primary difference upon TTE cosolvent addition is the drastically improved capacity and capacity retention as cycles progress (2019 Q4 report), manifested by the stable partial capacity peaks in Figure II.1.B.58D after the first cycle. Whereas the lithiation capacity of the LiFSI-DME is only 1,787 mAh/g, it is increased to 3,266 mAh/g for LiFSI-3DME-3TTE at 110^{th} cycle, 15% larger than its best-performing carbonate counterpart (at 2,841 mAh/g for GenF).

LiFSI-3DME-3TTE also enables the lowest polarization effect, ensuring lower energy barriers for lithiation and delithiation of a-Si. Such an observation is based on detailed exploration on the differential capacity profiles as a function of the cycle number for various electrolytes. After the first cycle, two lithiation peaks at ~0.07 V and ~0.20 V are observed (Figure II.1.B.58D). For LiFSI-DME, the intensity of these two peaks continuously decreases as cycling prolongs, in accordance with the lithiation capacity fade as cycling prolongs in Figure II.1.B.44A. The similar trend is observed for two delithiation peaks at around 0.30 V and 0.49 V. Whereas decrease in intensity of these four peaks is >40% for LiFSI-DME from Cycle 5 to Cycle 110, it is less than 12% for LiFSI-3DME-3TTE. Another benefit LiFSI-3DME-3TTE distinguishes itself from the other electrolytes is its highest lithiation potential after 5 cycles, shown in Figure II.1.B.59, indicative of its lowest polarization effect in prolonged cycles. This in turn allows for ease of a-Si lithiation in prolonged cycling. The passivation on the Si anode is generally considered the major driving force to increase the polarization effect upon cycling [49]. Research on EIS of the a-Si cycled in different electrolytes for various cycle numbers are

ongoing to unveil the relation between the surface resistance due to SEI growth and the polarization effect for the glyme electrolytes.

Ongoing research in collaboration with the NREL team includes elucidating and consolidating the surface chemistry heterogeneity on both of the in-plane and through-plane of the a-Si surface using depth-profile XPS and TOF-SIMS, exploring glyme SEI mechanical property by nano-indentation and local electrochemical and electronic properties of SEI formed in glyme-based by AFM- Scanning Probe Microscopy (SSRM).

XPS depth profiles (3-keV Ar^+ ions) were performed on each sample to reveal compositional changes throughout the SEI layers. Curve-fitting analysis was performed on the initial XPS spectra collected prior to the onset of sputtering to identify species present in the SEI.

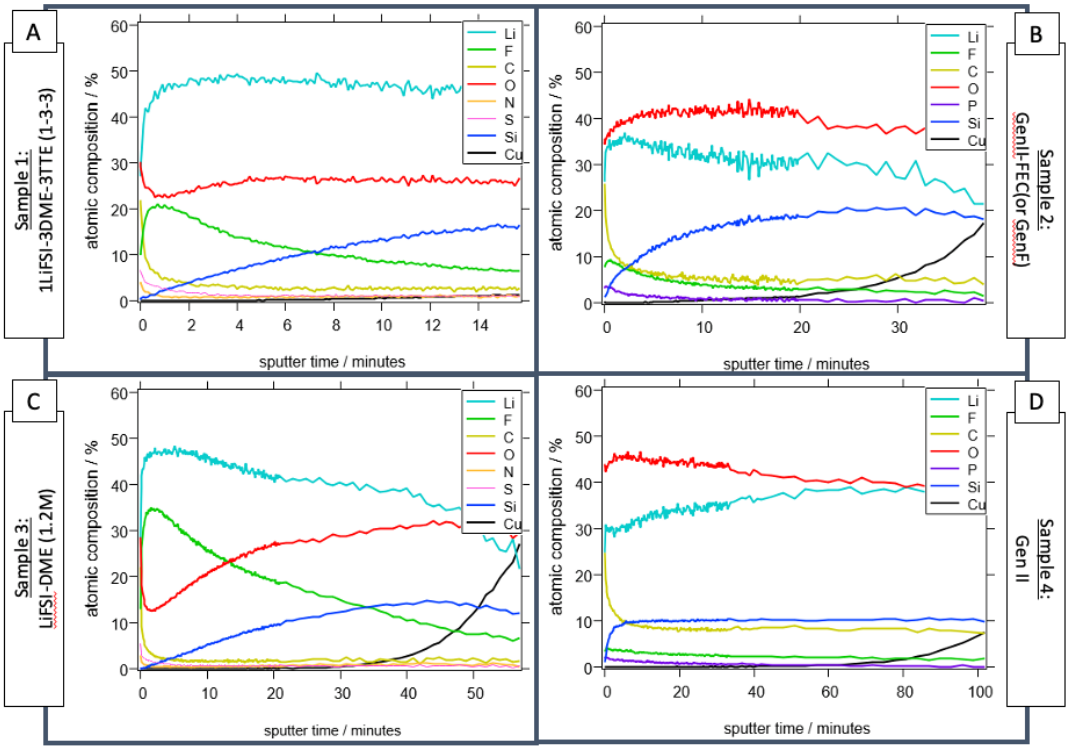

Figure II.1.B.60. XPS depth profiles of each sample, plotting atomic % composition as a function of sputter time for (A) sample 1 - 1LiFSI-3DME-3TTE (1-3-3) electrolyte, (B) sample 2 - Gen F electrolyte, (C) sample 3 - 1.2 M LiFSI in DME electrolyte, and (D) sample 4 - Gen 2 electrolyte.

Figure II.1.B.60shows that the samples cycled in glyme-based electrolytes (samples 1 and 3) are dominated by lithium content, whereas the Gen F and Gen 2 reference samples show higher oxygen concentrations. Curve-fitting analysis of the XPS core-level spectra (Figures II.1.B.61–II.1.B.65) further reveal that the glyme-electrolyte sample SEIs were composed of carbon-free inorganic compounds (e.g., Li_2SO_3 and LiF) to a greater extent than those of the carbonate-based electrolyte samples. Conversely, the Gen F and Gen 2 samples contain significantly higher amounts of Li_2CO_3.

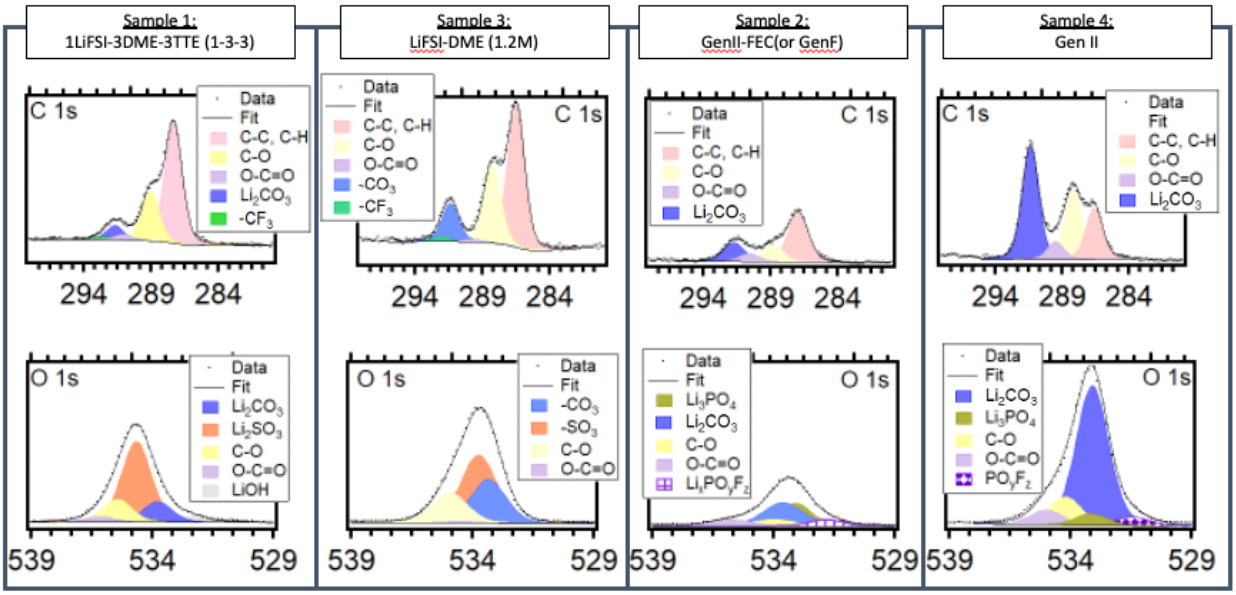

Figure II.1.B.61. C 1s and O 1s XPS core-level spectra for samples 1, 3, 2, and 4.

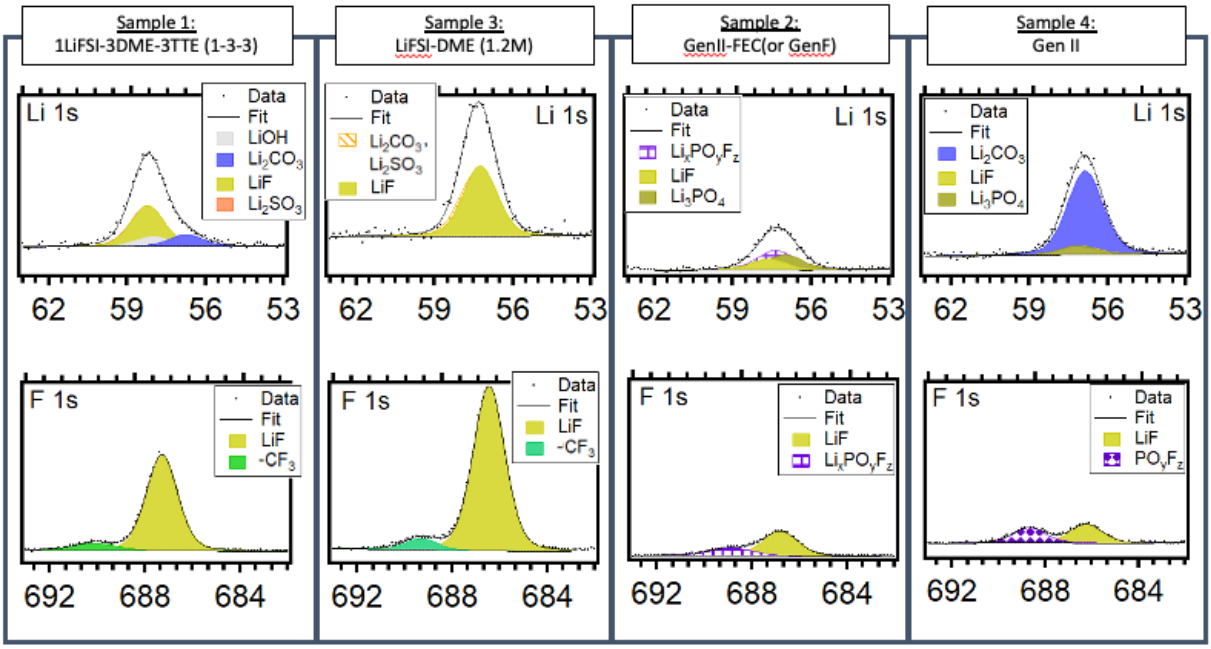

Figure II.1.B.62. Li 1s and F 1s XPS core-level spectra for samples 1, 3, 2, and 4.

Figures II.1.B.61 and II.1.B.62 identify SEI species associated with the core levels that have been most widely studied in previous lithium battery SEI studies (C 1s, O 1s, Li 1s, and F 1s). All spectra for particular core levels are plotted in the same intensity range so relative signals can be directly compared across samples. Phase assignments are made via a curve-fitting analysis where suitable constraints between binding energies and sensitivity-factor-weighted peak areas are simultaneously applied to relevant core-level peaks [50]. For instance, sample 1 was determined to likely contain Li_2SO_3 due to the fact that the sensitivity-factor-weighted oxygen intensity was three times that of the correlated sulfur intensity. The $(SO_3)^{2-}$ features were then tentatively assigned to Li_2SO_3 based on the presence of unassigned intensity in the Li 1s core level at the expected binding energy and at roughly the expected stoichiometric ratio. In the case of sample 2, the lithium

intensity is not high enough to confidently report that all of the carbonate and sulfite species are lithiated, and so it is more likely a mixture of lithiated and organic carbonate and sulfite species. The other major component of the glyme species is LiF, with sample 2 having more than sample 1. This is in agreement with the depth profiles in Figure II.1.B.60, where sample 2 shows a higher fluorine signal.

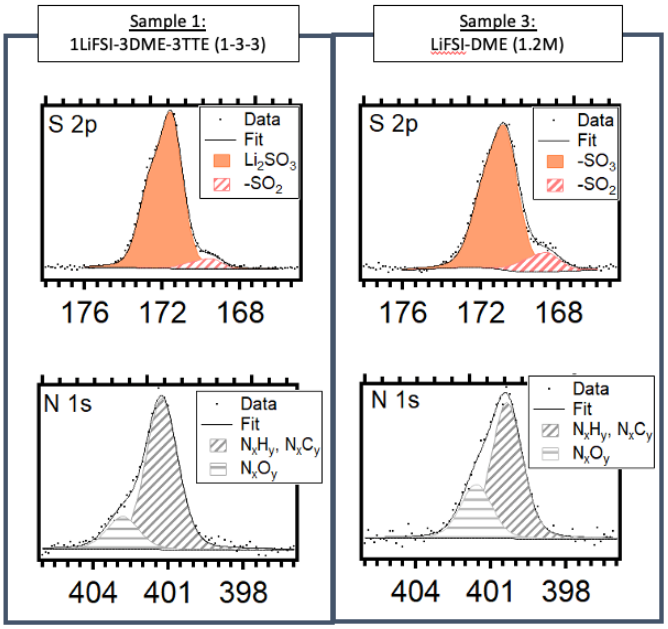

Figure II.1.B.63. S 2p and N 1s XPS core-level spectra for samples 1 and 3.

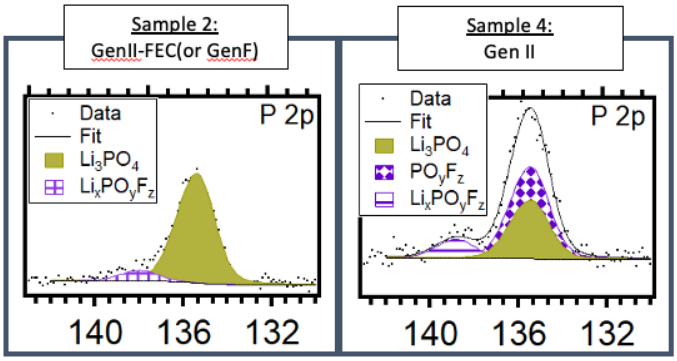

Figure II.1.B.64. P 2p XPS core-level spectra for samples 2 and 4.

Figures II.1.B.62 and II.1.B.64 show the XPS core-level spectra of the elements specific to the salts used in the glyme-electrolyte samples (S 2p and N 1s in Figure II.1.B.63), and carbonate-based electrolyte samples (P 2p in Figure II.1.B.64). Few quantitative XPS studies have been conducted in the precise identification of these species. In the case of the glyme samples, it is clear that similar amounts of sulfur- and nitrogen-based salt byproduct are deposited on the surface of the electrode. The sulfur species were determined to likely be SO_x compounds when considering the O 1s signal intensities, as discussed previously. For the nitrogen compounds, additional XPS data sets on reference materials would be acquired to confidently report specific species. In the case of the carbonate-based samples, NREL researchers have previously collected reference spectra on lithium phosphate, and can therefore identify its presence in the SEI with confidence. The remaining signal intensity is likely various fluorophosphate compounds.

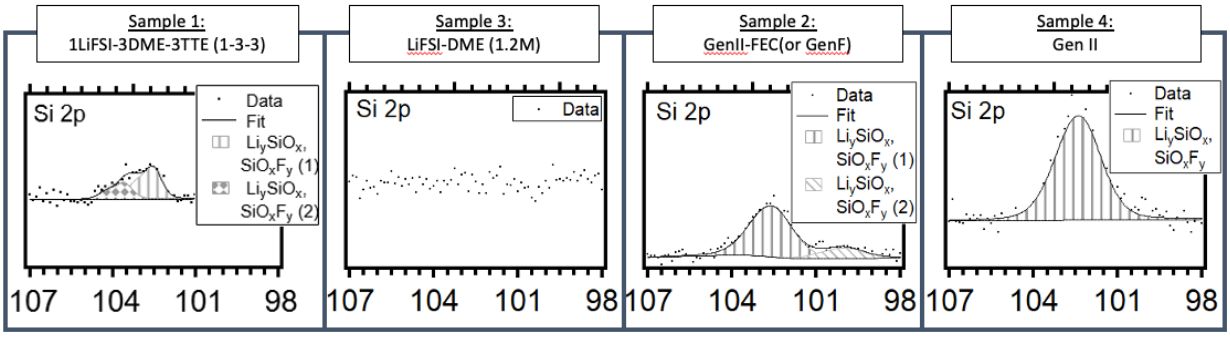

Figure II.1.B.65. Si 2p XPS core-level spectra for samples 1, 3, 2, and 4.

Figure II.1.B.65 shows that all samples except for sample 2 have some silicon signal that can be observed. Either the silicon-based species exist only at the surface of the original Si film, in which case the SEI would have to be less than 10 nm in order for there to be detectable XPS signal, or some of the silicon species are incorporated into the SEI further from the Si surface. The signal is strongest in sample 4, but it is still dwarfed by the intensity of the other core-level spectra. In Si-anode-based SEIs, silicon can exist in a variety of oxygenated, fluorinated, and lithiated species, but due to the very low Si 2p signal intensities, it is not possible to make definitive assignments for these samples.

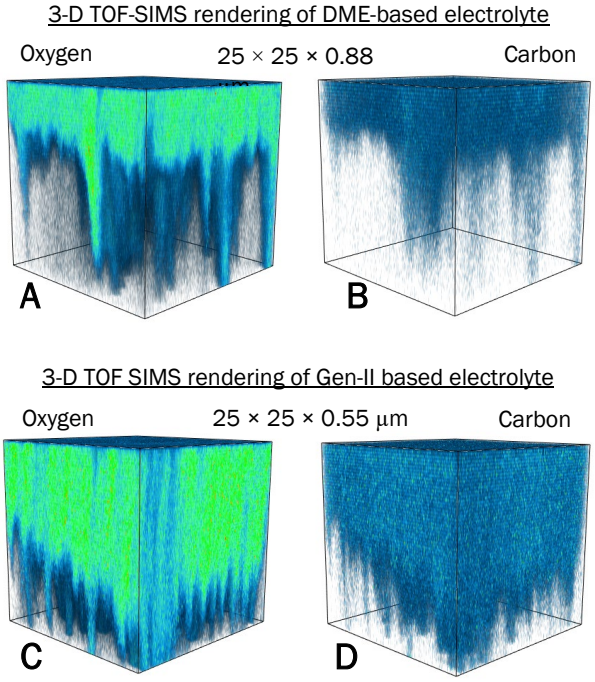

Figure II.1.B.66. TOF-SIMS tomography data for the cycled Si anodes in glyme-based (top row) and Gen 2 (bottom row) electrolytes. The formed SEI is much thinner with the cycled Si anode in glyme-based electrolyte, and more oxygen and carbon are noted in the cycled anode in Gen 2 electrolyte. 3D rendering of oxygen in the electrodes cycled in (A) glyme-based and (C) Gen 2 electrolytes. 3D rendering of carbon in the electrodes cycled in (B) glyme-based and (D) Gen 2 electrolytes.

TOF-SIMS results on the glyme-based electrolytes were consistent with XPS results, and the samples cycled in the glyme-based electrolytes had much less carbon and oxygen in the SEI compared to a sample cycled in Gen 2 electrolyte. This is consistent with the XPS results, which showed less carbonate species in the SEI for the glyme-based electrolyte cycled samples. A higher content of sulfur and fluorine in the glyme-based electrolyte

was also noted. The TOF-SIMS 3D tomography results, as shown in Figure II.1.B.66, also visually show the SEI was much thinner with the glyme-based electrolyte, also in agreement with the XPS results.

Understanding the chemical properties of the SEI in the glyme-based electrolytes using AFM-SSRM

AFM imaging was conducted to determine roughness and morphology of the electrodes. At larger scales, the sample roughness was dominated by the texture of the copper substrate, so the roughness was determined by an average of the root mean square roughness of four randomly selected 1 × 1-µm sites. These results can be seen in Figure 67. The roughness of all cycled samples increased as compared to the pristine sample, which is expected, and is due to the formation of SEI and the expansion and contraction that Si undergoes during lithiation (discharge) and delithiation (charge). Out of the cycled samples, sample 1 is the least rough, followed by sample 2 and sample 3. Sample 4 is the roughest. A greater increase in roughness is associated with a thicker SEI, and these relative roughnesses correspond with the SEI thicknesses discussed in the following section.

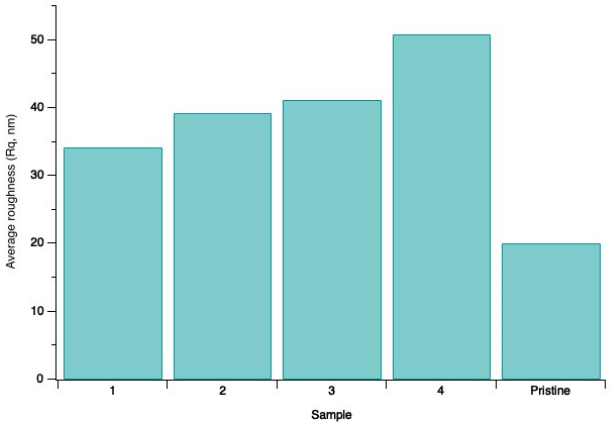

Figure II.1.B.67. Average root mean square roughness determined from 1 × 1-µm AFM scans.

SSRM resistivity vs. depth profiling was conducted for each sample. In this technique, successive SSRM scans are performed with a high enough probe force that material is milled away with each scan while resistivity is also measured. A low-force overview scan is then done after the milling to determine the depth of the resulting crater, which allows one to determine the resistivity as a function of depth. These resistivity vs. depth profiles are shown in Figure II.1.B.68. Samples 1, 2, and 3 all have thin SEIs formed on the surface, whereas sample 4 has a much thicker SEI, as well as a much greater active material depth before the Cu substrate is reached, indicating a larger volume increase. Samples 1–3 also show significant thickness increase of Si active material compared to the pristine sample, but in a less degree than sample 4. Additionally, the α-Si in samples 1 and 2 showed decreased resistivity as compared to the pristine sample. This resistivity decrease is expected as a result of Li incorporation during cycling. Sample 4 showed increased resistivity of the active material, which is consistent with previous SEISta SSRM work with Si cycled in Gen2 electrolyte. Resistivity increase can be the result of SEI ingrowth, fouling from electrolyte species, or mechanical fatigue due to volume expansion and contraction.

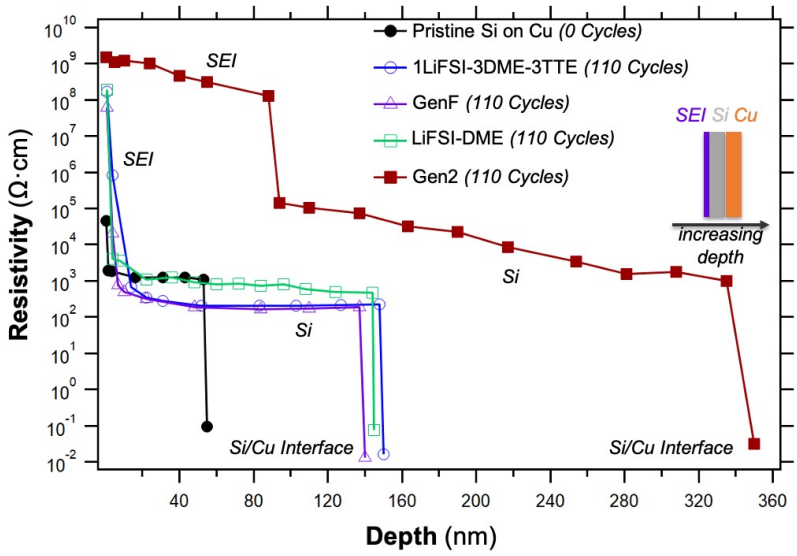

Figure II.1.B.68. Resistivity vs. depth profiles for all samples.

Additionally, 3D resistivity maps for each sample were created by interpolating the series of 2D resistivity scans along the depth direction that were generated during the milling described previously. These 3D maps, as shown in Figure II.1.B.69, provide a clear 3D visualization of the SEI and the underlying Si. Both the SEI and active Si can be seen by the difference in resistivity. For samples 1 and 2, SEI is mostly formed on the surface region with little amount ingress into Si, whereas for sample 3, SEI ingresses largely into Si, and for sample 4 SEI dominates through the milled depth. Due to the volume changes, the Si surface becomes rough, and as a result, the formed SEI is also rough.

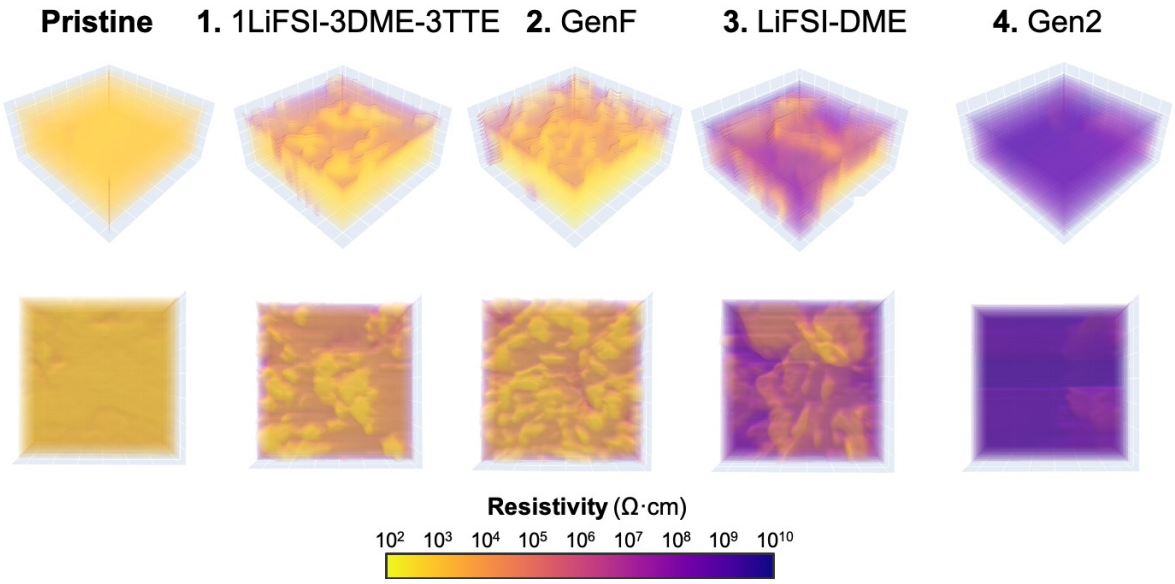

Figure II.1.B.69. 3D resistivity volume interpolations for all samples. Yellow regions are low resistivity and correspond to Si, whereas purple is higher resistivity and corresponds to SEI. The upper row presents a 3D view and the lower row represents a top-down view.

Theoretical understanding of the electrolyte

We use the reaction network approach to extract decomposition pathways of the electrolyte molecules relevant to the Si system. FEC is a common electrolyte additive found to mechanically stabilize the Si anode SEI. The presence of FEC increases LiF content at the SEI, and there is still no clear consensus on the exact pathway that the LiFEC molecule takes to decompose and produce LiF. To understand FEC decomposition mechanisms, a reaction network was constructed using over 9,000 molecules and 180,000 reactions. The network was able to capture four different ways the LiFEC molecule can ring open, and its respective pathways leading to LiF formation, as shown in Figure II.1.B.40. The green path in Figure II.1.B.70 is the shortest pathway predicted by the network, and it is also one of the most frequently expert proposed paths [22]. Although the blue path may seem the best path thermodynamically, it requires an additional LiFEC molecule and Li ion to assist in LiF. Similarly, the purple pathway requires an additional Li-ion to bond with the fluorine in LiFEC to form LiF. The green path does not require any additional species for LiFEC to decompose into LiF, CO_2, and C_2H_3O. This work not only validates our network-based approach but also highlights the value of the automated framework. Our approach can predict mechanistic pathways that took years for the community to identify manually.

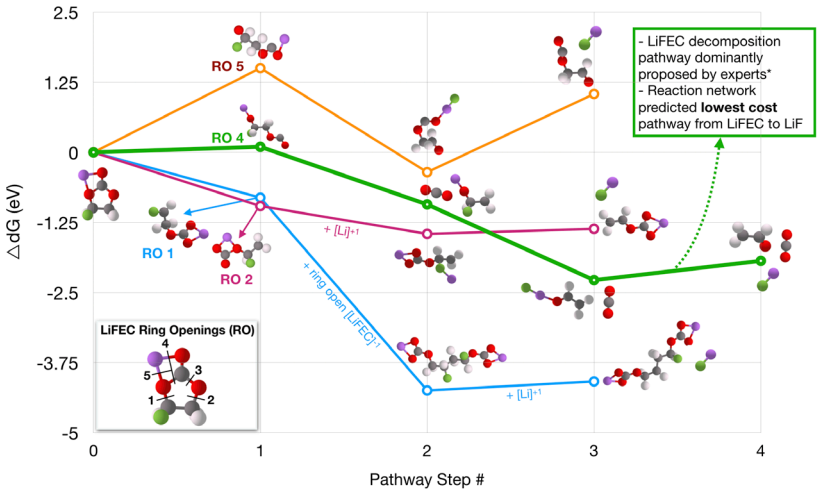

Figure II.1.B.70. Thermodynamic pathways from LiFEC to LiF found using the reaction network.

Furthermore, LiF also forms through $LiPF_6$ salt decomposition, which is commonly used in the Si system. The competing pathways from LiFEC and $LiPF_6$ leading to LiF formation are being investigated using the reaction network. An additional 3,000 $LiPF_6$-related molecules were added to the aforementioned network to form a network with over 12,300 molecules. Path search results from LiFEC and $LiPF_6$ to the four common $LiPF_6$ byproducts at the SEI ($LiPF_4$, PF_3, LiF, and LiF_2PO) are presented in Figure II.1.B.71. The network predicts the shortest path to LiF is for F-ion to leave FEC via FEC reduction and Li-ion to separate from $LiPF_6$. In other words, it is much easier to obtain fluorine from FEC and Li from $LiPF_6$. Moreover, LiF_2PO is formed by a fragment of FEC (CO_2 removed) bonding to PF_2.

The network is still in its preliminary stages of development and does not capture water reactions or energy change due to phase change. Many of the uphill steps in the initial stages of $LiPF_6$ decomposition can be lowered in thermodynamic cost with the assistance of water. Moreover, kinetics are not currently integrated into the network, but will soon be in the future.. Future work will continue the development of the reaction network tool and effectively use it to clarify the LiF formation mechanism at the SEI as a function of electrolyte content.

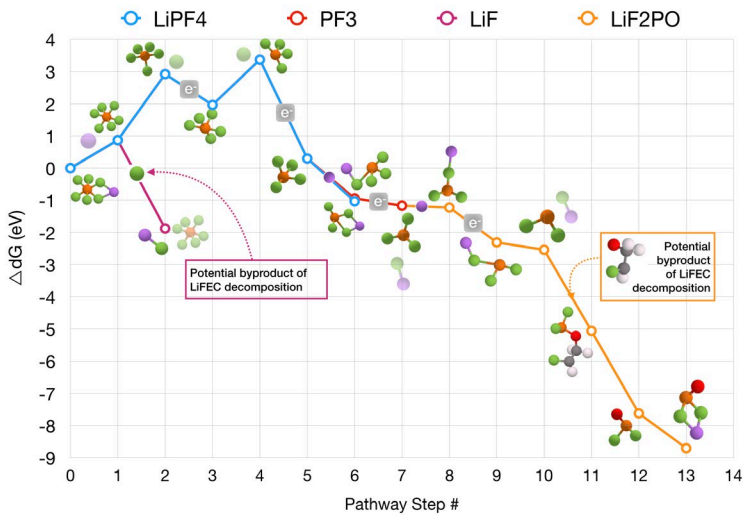

Figure II.1.B.71. Decomposition pathways of $LiPF_6$ in the presence of LiFEC.

4. Role of CO_2 additives

The goal of this work was to determine the effect of CO_2 on the stability of SEI formation on model electrodes, but examining the changes in the nature of the SEI (XPS, FTIR/Raman, and quantitate electrochemical measurement) as a function of CO_2 concentration. To accomplish this, a team of scientists from multiple laboratories collaborated to evaluate the resulting SEI chemistry from pouch cell-type batteries, with and without gaseous CO_2. The cells were built and cycled at ORNL using our standard Gen2 electrolyte with 50-nm amorphous silicon electrodes and lithium metal counter electrodes with Dreamweaver separator to ensure electrolyte wetting and CO_2 transport. Samples were sent to the partner laboratories for FTIR (NREL), matrix-assisted laser desorption/ionization (MALDI) (LBNL), Raman (ORNL), XPS (ORNL), TOF-SIMS (NREL), NMR (ANL), and SSRM (NREL) analysis.

We found the following results:

1. The SEI chemistry changed significantly when using CO_2, resulting in an SEI layer that has significantly more inorganic component

2. The irreversible capacity losses were constant regardless of the presence of CO_2

3. Fabrication of the cells is important, and still an unresolved issue, which we believe is due to air or water infiltration

4. Air or moisture infiltration has a larger impact on cell performance than CO_2.

As part of this set of experiments, we prepared multiple test cells cycled under the same conditions. These test cells involve the formation of pouch cell-type batteries. The electrodes were 2 by 2 in. in area (Figure II.1.B.72). We used three pieces of Dreamweaver separator. This material was chosen because it wets extremely well with electrolyte (almost instantaneous); because of this wettability, we believe it will allow gas infiltration and transport. The cells were sealed in a glovebox under argon. Samples were removed to air and the CO_2 was dosed to the cell using a gastight syringe. Cells were stacked under a 500-gram copper plate to provide stack pressure. The cells were cycled at a C/10 rate for 9.5 cycles (10 lithiations). The cycled cells were loaded into the glovebox and disassembled. Portions of the cells were washed with 2 mL of dimethyl carbonate (dropwise addition) and dried under vacuum. Other parts were unwashed for MALDI or NMR experiments. The advantage of this approach is that all the characterization was performed on the same set of

samples instead of samples made at different laboratories. This is important for this work as the dosing process affects cycling.

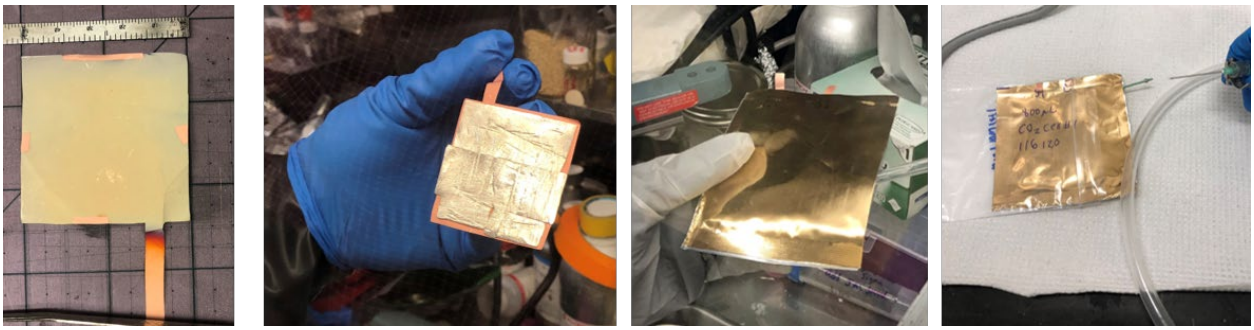

Figure II.1.B.72. Images of the Si electrode (left), Li electrode (center left), pouch cell being injected with electrolyte (center right) and pouch cell injected with CO_2 (right).

During the course of these experiments, we observed that dosing and cell preparation had a major influence on reproducibility. Figure II.1.B.73 shows a collage of data collected for different cell fabrication and dosing protocols. As can be seen in these data, the pie charts show the average elemental composition for at least two samples measured by XPS along with the cycling data. In Round 1, cells were sealed after bringing to air, with or without dosing with CO_2. Under this process, the XPS data looked the same (composition and cycling). In Round 2, the cells were sealed in a glovebox and then the leads were coated in epoxy, as this was viewed as a source of gas leakage. In Round 3, the CO_2 gassing protocol was revised to use a gastight syringe to dose the samples with 2 mL of CO_2 through the smallest hole possible. As can be seen from the experiments in Rounds 2 and 3, the SEI compositions were similar, but varying significantly from Round 1.

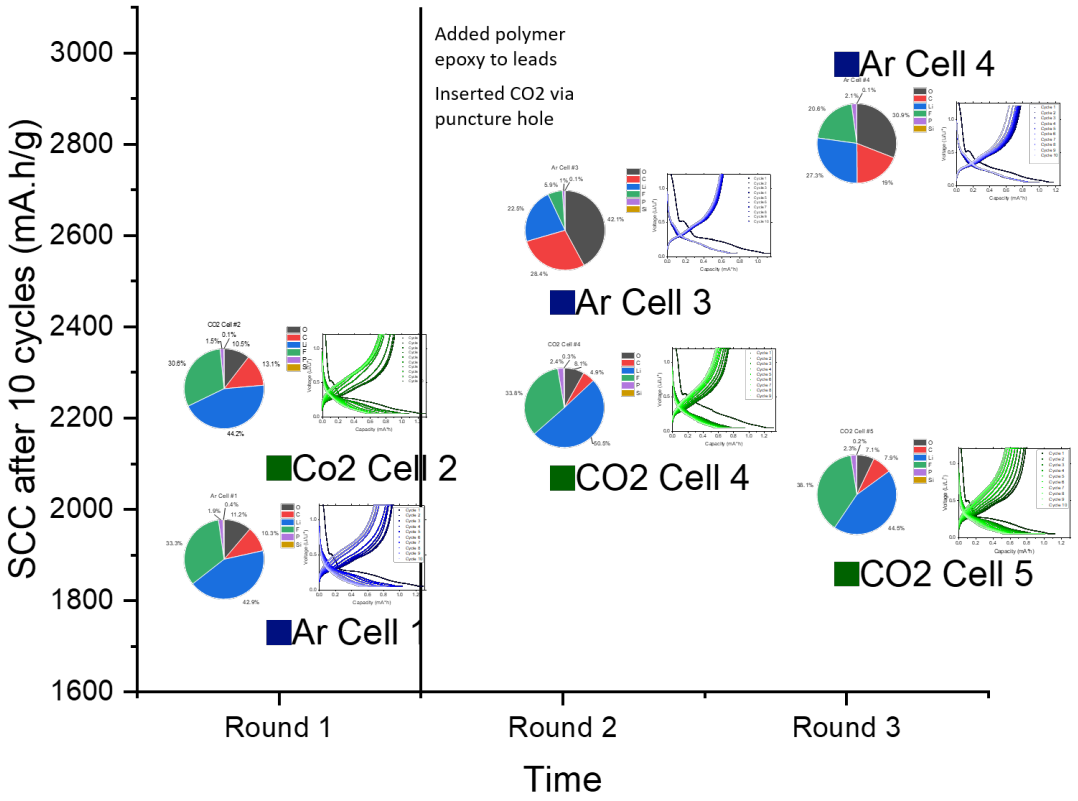

Figure II.1.B.73. Collage of SEI capacity and capacity retention as a function of fabrication method. Left axis is the capacity retention after 10 lithiations for the standard 50-nm electrode.

From these data, it is clear that the SEI becomes more inorganic-like with the introduction of CO_2, as evident by the increase in F and Li content (green and blue data, respectively). Note we use F as a marker for inorganic LiF-type SEI layers. In contrast, the SEI with Ar cells has higher concentrations of carbon (red) and oxygen (black). The higher concentrations of carbon and oxygen is consistent with a more "organic-like" SEI layer. Interestingly, these results mimic what was observed using neutron reflectivity data to follow the SEI formation with and without FEC. The FEC-containing electrolyte resulted in a more F-rich SEI, whereas the FEC-free one was more organic in nature. This points to the CO_2 promoting the inorganic SEI components.

The second observation that is clear from the data is that the CO_2 has no apparent benefit to the cycling performance of the electrodes over a standard argon configuration. Figure II.1.B.74 shows average cycling data collected for at least three cells, along with error bars for these measurements. The left data show the cells measured in argon, whereas the right data show cells dosed with CO_2. Both cells show large irreversible capacity losses with the first cycle and a slow but steady decline in capacity retention with cycles. These data indicate that CO_2 is not the cure to an unstable SEI.

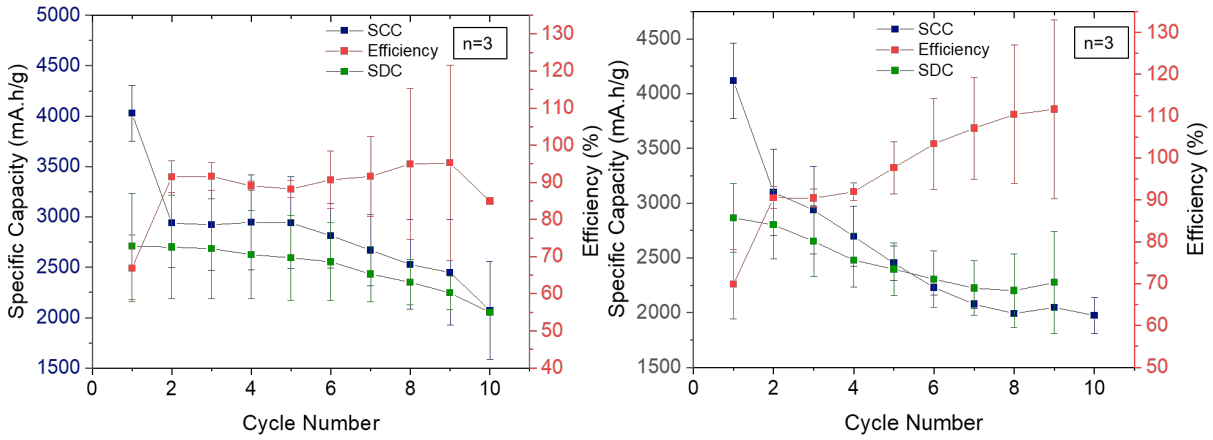

Figure II.1.B.74. Average cycling data for cells cycled in argon (left) and CO_2 (right).

To explore the organic components of the SEI, unwashed electrode samples were subjected to gradient wash and MALDI experiments. Figure II.1.B.75 shows representative FTIR spectra collected during the gradient washing process (after each elution step). In this work, progressively larger fractions of ethyl acetate (EA) are added to a hexane (Hex) solution, which gradually increases the elution intensity in terms of polarity. The electrode is evaluated as a function of EA:Hex ratio. The hexane is a "less" aggressive solvent to remove SEI components, whereas EA dissolves more carbonate and polymer species. After each wash, the electrode surface was probed with FTIR spectroscopy. Figure II.1.B.40 demonstrates that the more aggressive wash removes more and more of the residual EC (marked on the spectra) and $LiPF_6$ (~825 cm^{-1}) both for electrodes cycled with argon and CO_2. It was found that 3:7 EA:Hex elution can fully remove EC and most of $LiPF_6$ from the electrode surface.

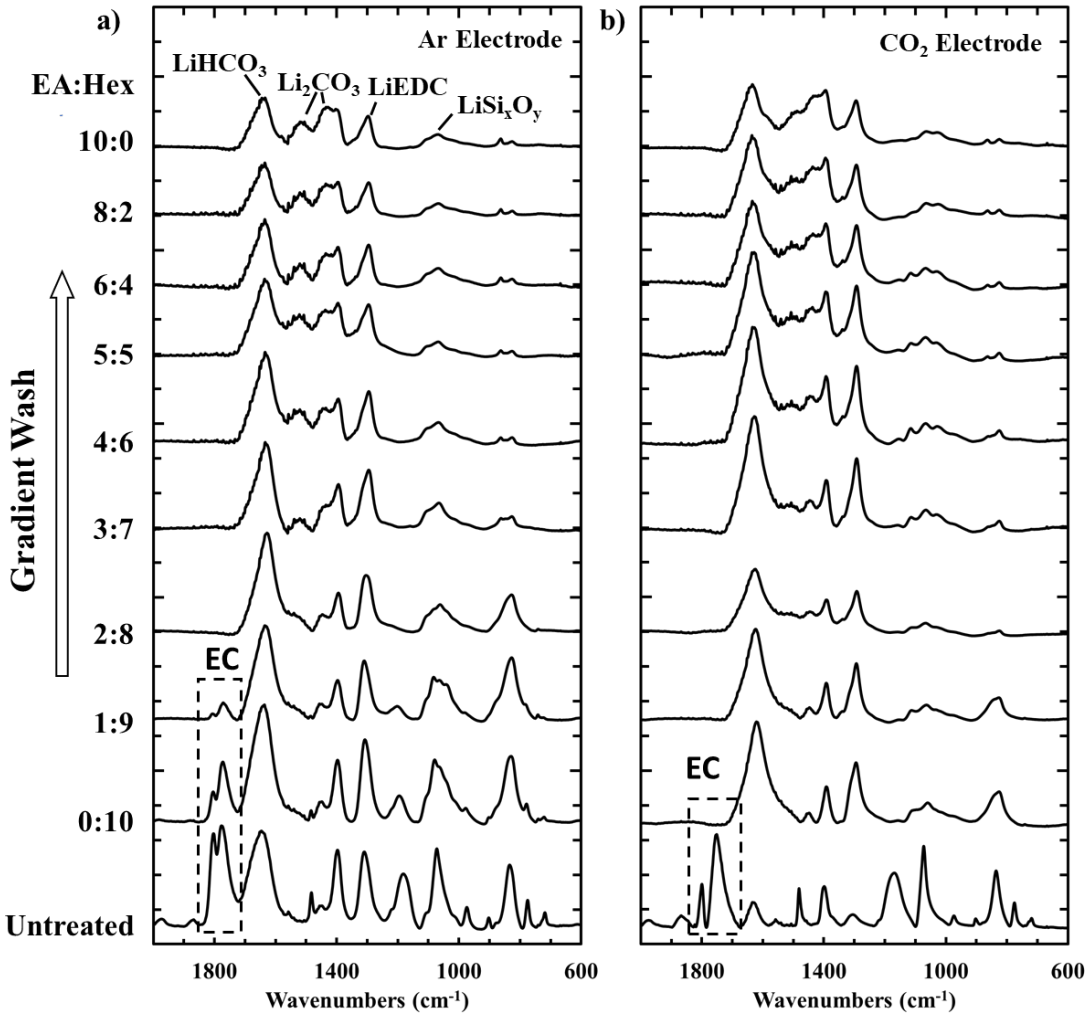

Figure II.1.B.75. FTIR spectra of electrodes after each gradient wash step (a) cycled with argon and (b) cycled with CO_2.

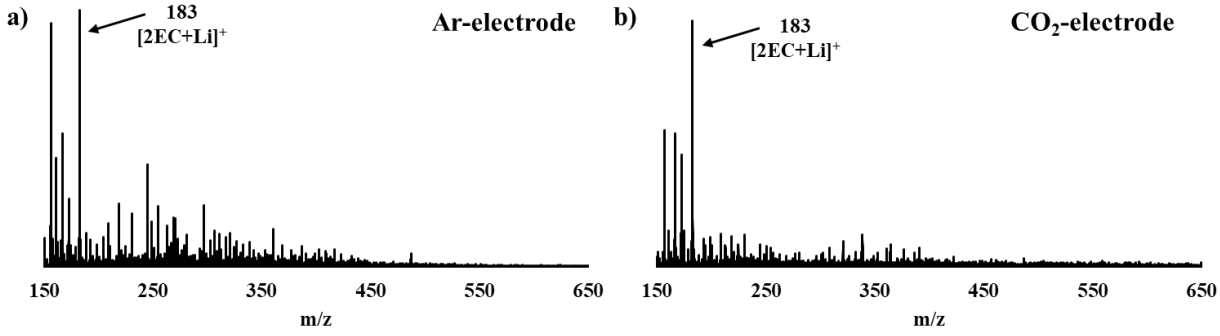

Figure II.1.B.76. MALDI spectra of electrode cycled with (a) argon and (b) CO_2.

The freshly retrieved electrodes (no elution performed) were measured by MALDI as well, and the representative data are shown in Figure II.1.B.76. For both of the electrode samples cycled with argon and CO_2, only EC signal was observed with strong noise in the higher-mass regions. This result demonstrates that residue EC on the electrode surface hinders MALDI measurement of the organic species in SEIs.

When the electrodes were subjected to on-electrode chromatography with 3:7 EA:Hex elution to remove the residual EC and $LiPF_6$, PEO species were found as shown in Figure II.1.B.77 (a and b). The assignment of PEO is based on the repeating pattern of 44 m/z. The same type of PEOs were found for electrodes cycled with argon and CO_2, as evidenced by their identical distribution of PEO masses. On the other hand, PEO formation seems to be promoted by CO_2 additive as the relative PEO signal intensities in the case of CO_2 is significantly higher.

To further investigate the difference in PEO formation, the electrode samples that have gone through the entire gradient wash process (0%–100% EA:Hex), namely treated with stronger elution conditions, have also been characterized by MALDI. As shown in Figure II.1.B.42c, the argon-cycled electrode presents no PEO signals but only matrix signals (2,5-dihydroxybenzoic acid or DHB is the matrix). In contrast, the CO_2-cycled electrode still presents the high-mass PEO species (~1,000 m/z) with the same mass distribution. Notably, a new series of PEO masses were found in the lower mass range (~600 m/z) with a different pattern of mass distribution. These results demonstrate that the PEOs generated with CO_2 additives are higher in quantity in SEIs and are more robust against solvent elution. It is possible that the PEOs formed with CO_2 are generated in the inner sections of the SEIs.

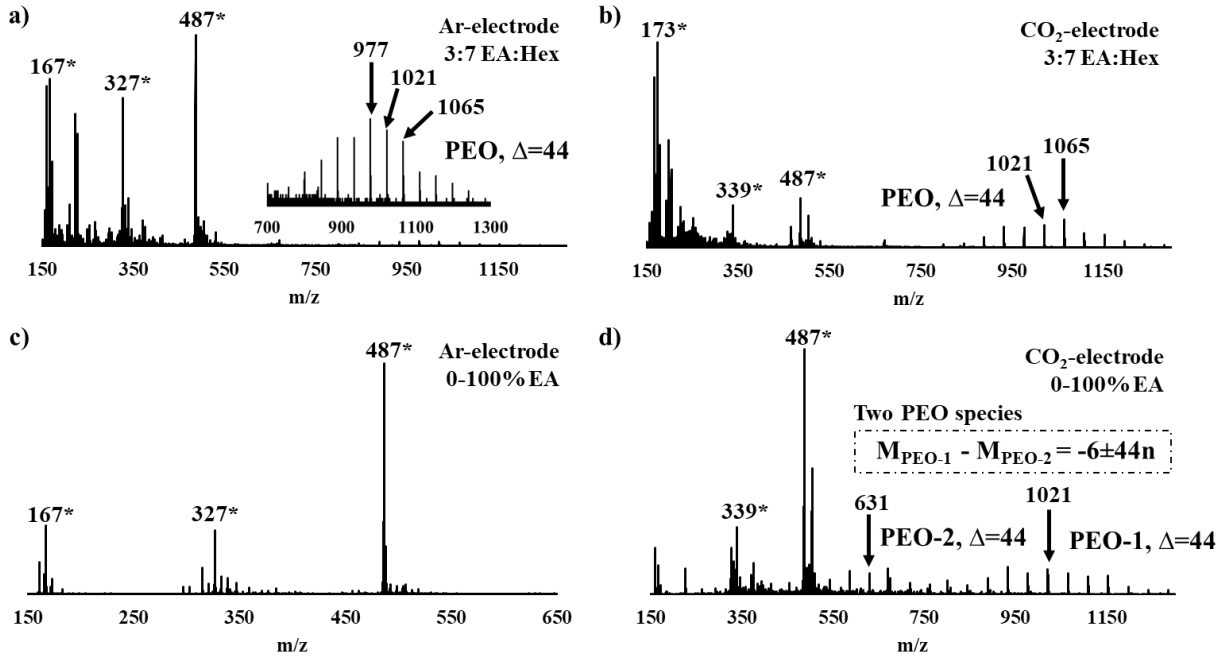

Figure II.1.B.77. MALDI spectra of electrodes cycled with argon after (a) 3:7 EA:Hex elution and (c) 0%–100% EA:Hex elution. MALDI spectra of electrodes cycled with CO_2 after (b) 3:7 EA:Hex elution and (d) 0%–100% EA:Hex elution. *Signals originated from lithiated DHB clusters: m/z 167 = $[DHB\text{-}H+2Li]^+$, 173 = $[DHB\text{-}2H+3Li]^+$, 327 = $[2DHB\text{-}2H+3Li]^+$, 339 = $[2DHB\text{-}4H+5Li]^+$, 487 = $[3DHB\text{-}3H+4Li]^+$.

AFM was utilized to examine the DMC-washed surfaces of the formed SEIs after 9.5 cycles, revealing distinctly different surface morphologies for the Ar and CO_2 electrolyte samples (Fig. II.1.B.78a). Although the roughness and size of features on the CO_2 sample appear to be representative of the underlying Cu substrate, finer features were detected on the surface of the Ar control sample (Fig. II.1.B.78b), suggestive of additional SEI formation.

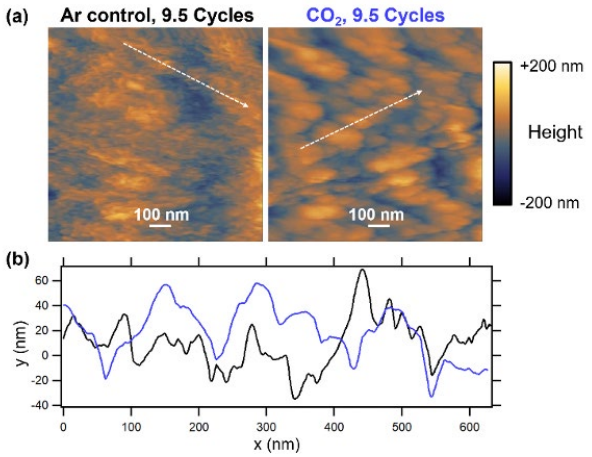

Figure II.1.B.78. 1 × 1-µm AFM images of SEI formed on 50-nm a-Si on Cu after 9.5 cycles. (a) Comparison of the characteristic surface morphologies. (b) Line scans extracted from each image depicting the comparatively smaller surface features on the surface of the Ar control sample (black trace) than the CO_2 sample (blue trace).

Resistivity vs. depth profiles were obtained using SSRM to investigate the thicknesses of the layered structures and the electronic contrast between them (Figure II.1.B.79). The SEI formed from the Ar-containing electrolyte control sample was measured to be thicker and more resistive than the SEI formed from the CO_2-containing electrolyte. The underlying lithiated Si thin film in the Ar sample was 1–2 orders of magnitude more resistive, perhaps due to a more porous SEI formed from the Ar electrolyte, permitting additional fouling by species that contribute to an increase in resistivity. SEI thickness was measured to be 14 nm on the CO_2 sample and 21 nm on the Ar sample. The thickness of the lithiated Si thin film was measured to be approximately 75 nm in the CO_2 sample and 100 nm in the Ar sample.

Further analysis of the unwashed electrodes as well as electrolyte samples was performed via NMR using $^{13}CO_2$ dosed cells vs. undosed cells (Figure II.1.B.80). Solids ^{13}C MAS NMR data for these *electrode* samples are shown in Figure II.1.B.80. New peaks (marked with arrow) in the high-frequency region ~200 ppm due to aldehyde/ketone-type organic solid species were observed, indicating changes in SEI chemistry. However, no clear new soluble species in the solutions ^{13}C NMR of the *electrolyte* samples of $^{13}CO_2$ dosed cells have been found. The results suggest CO_2 dosing altering the solid SEI speciation of the electrodes.

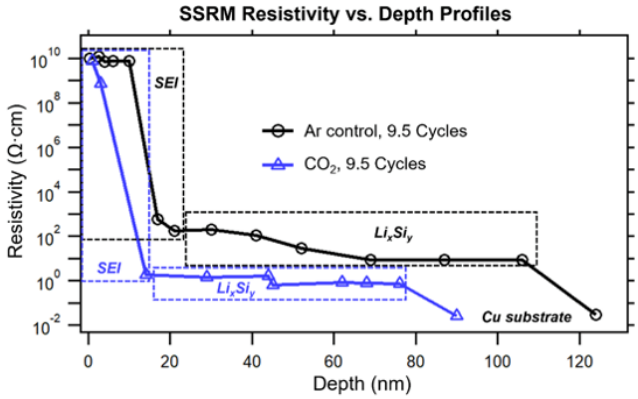

Figure II.1.B.79. SSRM resistivity vs. depth profiles obtained from samples after 9.5 cycles with Ar and CO_2 electrolytes. Composition is labeled for each profile, showing SEI at the surface, the lithiated Si thin film (Li_xSi_y), and the copper substrate beneath.

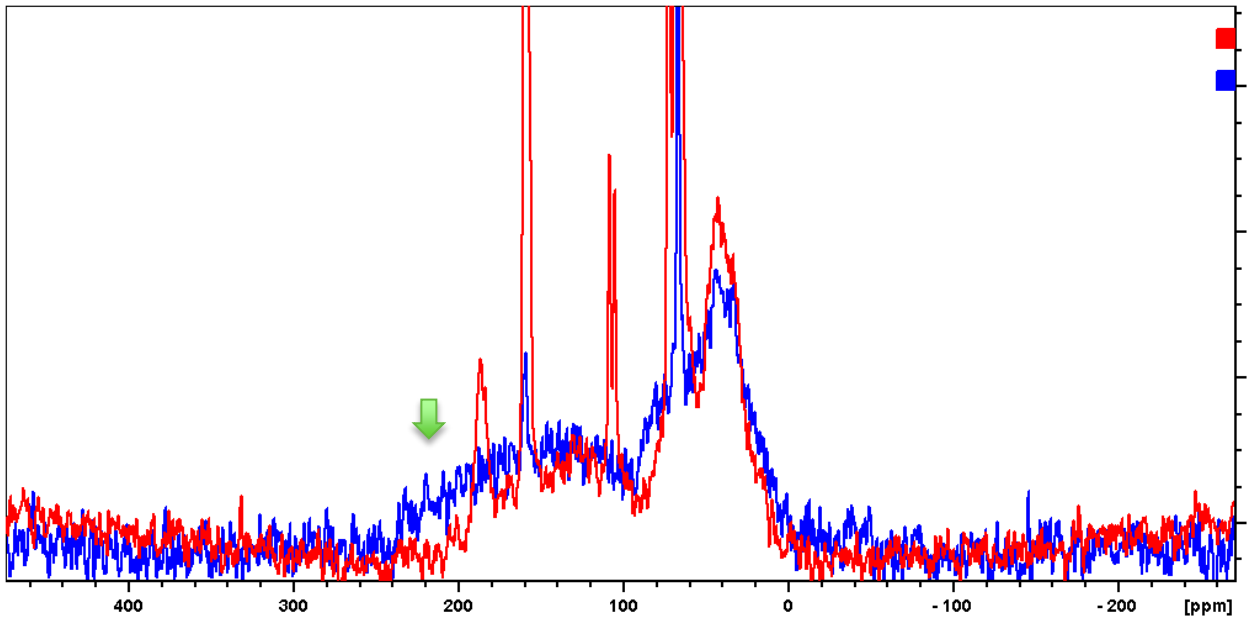

Figure II.1.B.80. NMR data collected for cells with (blue) and without (red) CO_2.

5. Mechanical properties of SEI and impacts

To investigate the quantitative influence of the mechanical degradation of SEI, we designed the following comparative study: A test sample allows lateral expansion of Si thin-film electrode by using a polymeric substrate (polydimethylsiloxane—PDMS), while a control sample does not allow the lateral expansion by using a rigid substrate (fused silica). The lateral expansion of Si thin-film electrodes directly translates to mechanical stretching of SEI (i.e., the SEI formed on the test sample is expected to undergo mechanical deformation, whereas that formed on the control sample does not). Comparing the cycling performance and the SEI compositions of the two types of samples is expected to unveil the influence of the mechanical deformation effect. As the first step, we conducted preliminary experiments to establish a proof of concept of this approach. Both studies contribute to a comprehensive understanding of the decomposition reactions at the Si-electrolyte interface.

As recently reported, one of the main manifestation of the electrolyte chemical and electrochemical instability is the so-called “breathing effect” (i.e., the continuous growth and shrinking of the SEI thickness upon lithiation and delithiation, respectively [51]). We have further confirmed this effect by XPS, being able to determine that during the first delithiation step, the insoluble components of the SEI are removed to a large extent, exposing the underlying Si core levels. This process repeats itself during the second delithiation, but to a lower extent, as a larger fraction of the SEI components are able to remain on the surface. This constant dissolution or detachment of the SEI from the Si surface anode during delithiation and its formation again during the lithiation steps are the source of severe charge consumptions. The use of thin (50-nm) electrode, enabled us to exclude the contribution of cracking to the problem, leaving the intrinsic (electro)chemical or possibly mechanical instability of SEI as the cause of the breathing effect and related charge consumption.

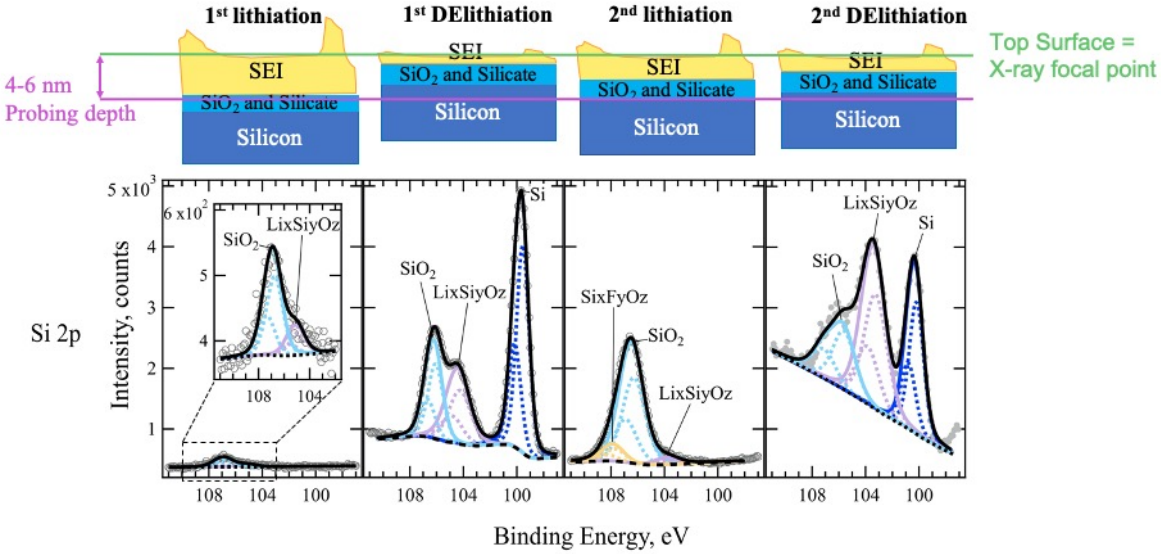

Figure II.1.B.81. The breathing effect revealed through the analyses of the Si core levels.

In order to study the composition of the SEI as a function of state of charge and cycle number, the a-Si/n-SiO_x thin films were galvanostatically cycled, rinsed, and transferred into the XPS system through airtight systems. For each sample, XPS spectra were acquired and peaks were fitted to determine the species present and their relative concentration. An example of the fitting procedure for some relevant core levels is shown in Figure II.1.B.82, whereas the results of the quantitative analysis are shown in Figure II.1.B.83.

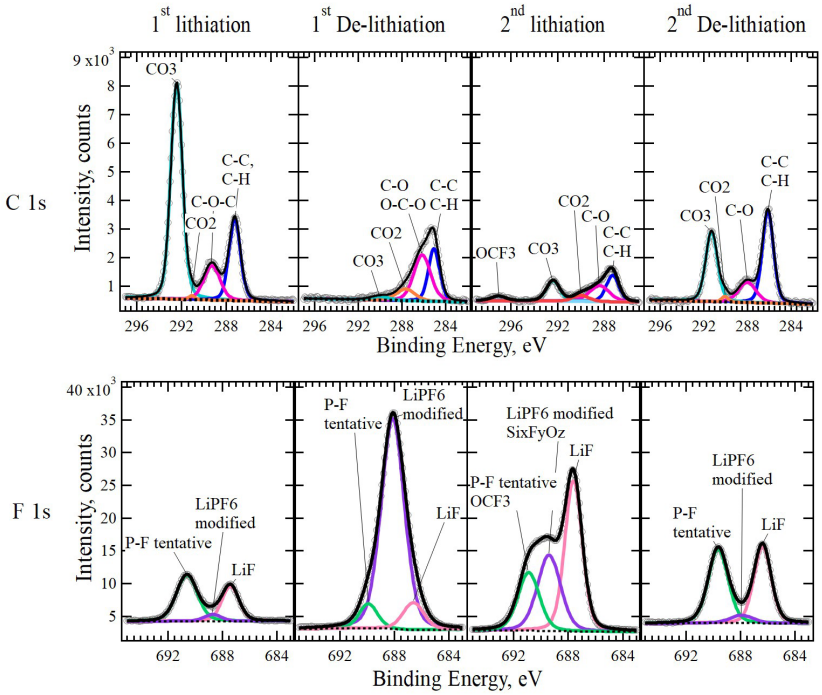

Figure II.1.B.82. An example of the fitting routine used for the phase identification applied to the C 1s and F1s core levels.

Upon the first lithiation, the SEI is rich in the decomposition product of the solvent (overall C signal is ~20 at. %, of which 10 at.% is due to carbonate alone). The salt-derived decomposition products are far less, about 10 at. % based on fluorine, of which only a small fraction (~2 at. %) is due to LiF.

Upon delithiation, the composition of the SEI changes drastically. The amount of carbonate species after delithiation is extremely low (0.4 at. % based on C), a reduction by a factor of 30 with respect to the carbonate content present in the lithiation stage. Surprisingly, the decomposition product of $LiPF_6$ is the major inorganic component, whereas LiF does not vary by much in comparison to the previous measurements.

During the second lithiation, the SEI forms again but with a composition different than the one formed during the first lithiation. Carbonate is the main C-containing species, but they are present in a much lower concentration (1.36 at. % in the second lithiation vs. 11.6 at. % for the first lithiation, thus about an order of magnitude lower). This means that the surface has been largely passivated with respect to the decomposition of the organic solvents and only a tenth of the decomposition of the organic solvent is still happening during the second lithiation. Conversely, the amount of salt-decomposition products is still quite considerable. Indeed, LiF is the major SEI component formed during the second lithiation, with a relative at. % 4–5 times higher than in previous samples (first lithiation and first delithiation). Finally, during the second delithiation, the SEI dissolves or detaches again. LiF is still the main component of the SEI, although its at. % is lower than before. Carbonate is present too, but in much lower quantities with respect to fluorinated compounds.

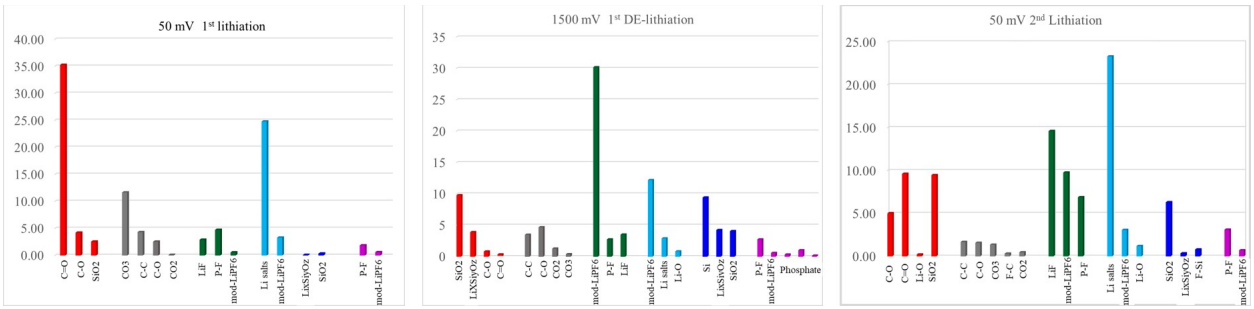

Figure II.1.B.83. XPS quantitative analysis shown for the first lithiation, first delithiation, and second lithiation process.

Regarding the experiments on the mechanical instability of SEI, the lateral expansion of the Si electrode on the polymer substrate (test sample) appears in the form of surface wrinkling. A mechanics analysis suggests that the wrinkles have a uniform wavelength to minimize the total strain energy [23]. Thus, the amplitude and the wavelength of the wrinkles can provide a quantitative level of SEI stretching. Figure II.1.B.84 summarizes the results from our preliminary experiments where we observed this phenomenon. First, a thin-film electrode consisting of Ti (~10 nm)/Ni (~50 nm) current collecting layer and Si (~60–70 nm) layer was created by sputter deposited on a PDMS substrate (Figure II.1.B.43a). Second, we designed/fabricated a custom electrochemical cell for in situ optical microscopy (Figure II.1.B.43b). The sample was assembled to the custom cell and integrated into an optical microscope setup. Next, the Si thin-film electrode was electrochemically cycled while the optical microscope captured the surface topography evolution in real time. Figures II.1.B.43c–e show three representative optical microscopy images taken at as-prepared, lithiated, and delithiated state of the Si electrode, respectively. Also shown is the 2D fast Fourier transform (FFT) images, which visualize the characteristics of the wrinkled patterns. The electrode was initially flat without any pre-wrinkles; thus, the corresponding FFT image shows no particular pattern (Figure II.1.B.84c). After the first lithiation, the lateral expansion of Si spontaneously formed surface wrinkling (Figure II.1.B.84d). Distinctive high-power location was observed in the FFT image (highlighted in dashed squares); this indicated that there was a characteristic wavelength of the wrinkles of approximately 24 μm. The wrinkles mostly disappeared after the subsequent delithiation due to the contraction of the Si electrode (Figure II.1.B.84e). A minor wrinkled patter may be attributed to irreversible Si volume change. The corresponding FFT image also showed a drastic decrease of power, which confirms the fading of the wrinkles. This series of observations implied that the thin-film electrode on a polymer substrate can apply cyclic strain on the SEI.

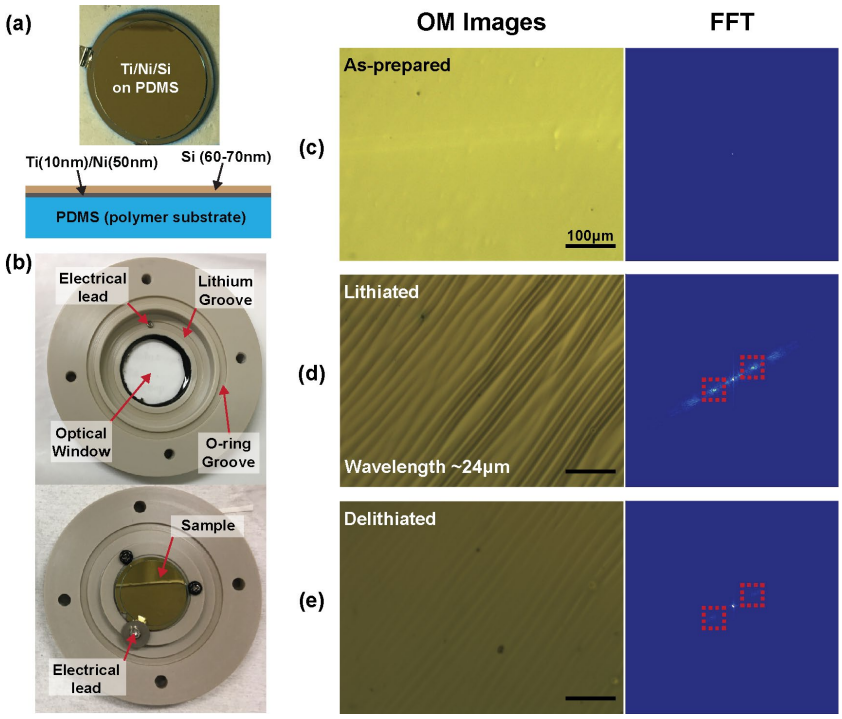

Figure II.1.B.84. Summary of key results from the investigation on the mechanical deformation of SEI. (a) A photograph of Si thin-film electrode consisting of Ti (10 nm)/Ni (50 nm)/Si (60–70 nm) layers on a PDMS substrate. Also shown is a schematic of the electrode structure. (b) A photograph of a custom electrochemical cell for in situ optical microscopy. (c–d) Optical microscopy images of the sample surface at as-prepared, lithiated, and delithiated states. Also shown are corresponding 2D FFT images.

Moiré microscopy continued to be developed and improved for the in situ study of in-plane strain in the SEI and silicon electrode during FY 2020.

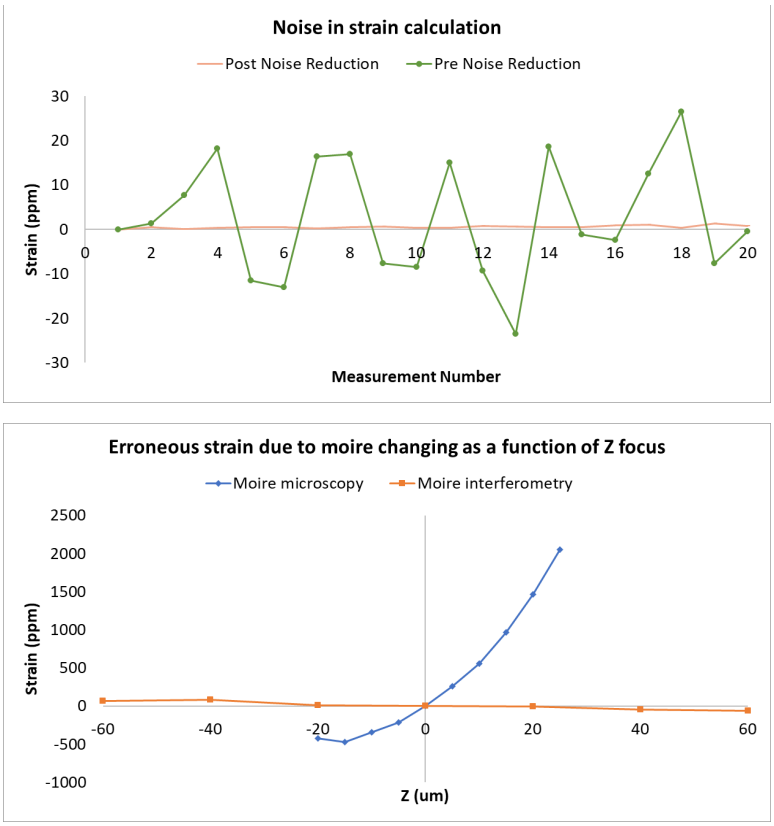

Figure II.1.B.85. Decrease in noise while static imaging by changing cameras and employing more sophisticated data analysis programming (top) and decrease in sensitivity to Z-position when switching from moiré microscopy to moiré interferometry (bottom).

Sample preparation and the in situ cell design were improved. The model electrodes were 50-nm E-beam evaporated silicon on 2-µm copper foils. On the copper side of the electrode, 61-nm silicon gratings were created lithographically. The thickness of the silicon was designed to act as an anti-reflection coating. However, it was discovered that this coating did not provide sufficient contrast to create an adequate amplitude grating. New samples had an improved anti-reflection coating for an improved signal-to-noise ratio. Furthermore, thinner samples were fabricated to improve strain sensitivity. By decreasing the thickness of the copper foil, the strain in the SEI and silicon will increase, decreasing the required strain resolution. Lastly, the use of oversampling techniques was investigated to further improve strain resolution.

The moiré microscope was also improved. The first version used structured illumination as the reference grating and was found to be too sensitive to changes in the Z-focus of the microscope. Various approaches were attempted to compensate for changes in Z-position but were not consistent enough to merit further development. The second version was a moiré interferometer where the reference grating was created through the interference of two beams. To take advantage of the previous setup, the grating used in structured illumination was used to create the ±1 diffraction orders that were recombined at the sample surface, resulting in a more stable reference grating. A filter was used to block all other diffraction orders created by the grating. The interference pattern for the reference grating, and therefore the moiré pattern, was much less sensitive to changes in focus.

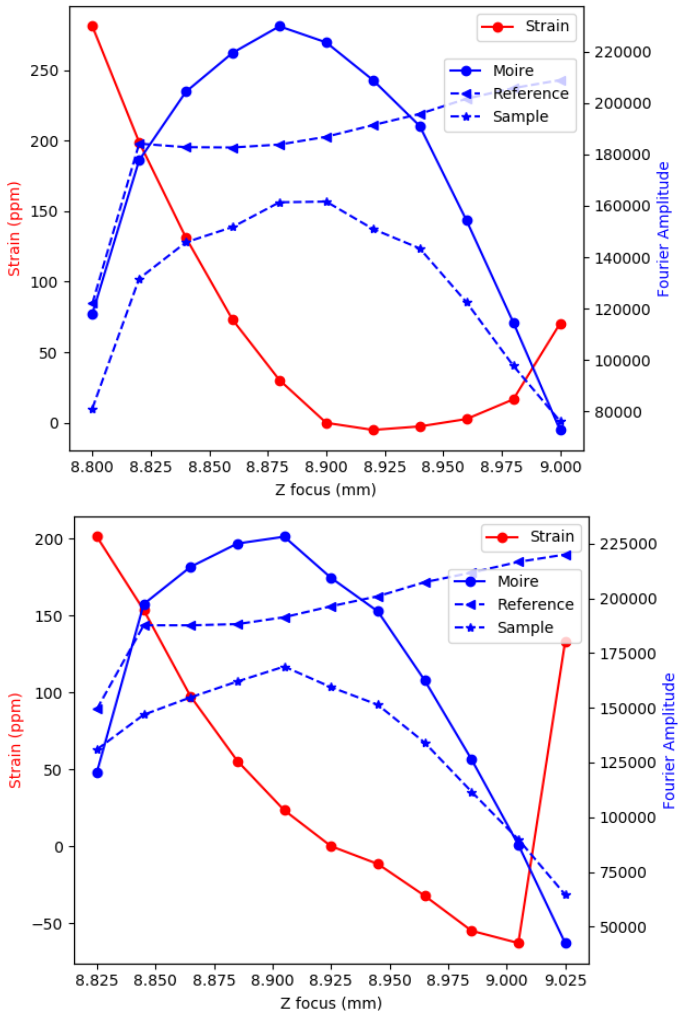

Figure 47. Erroneous strain behavior on a silicon control wafer as a function of Z-position for a well-aligned system (top) with a relatively flat region of the strain curve and the strain behavior for the same sample tilted 0.036° (bottom).

Another issue with the setup was a large (on the same order as the desired measurement) error when static imaging. By changing cameras and writing new data analysis programs, the noise was decreased tenfold. The reduction in noise of the measurement (top) as well as the decreased sensitivity of Z of the moiré pattern (bottom) are shown in Figure II.1.B.85.

Currently, troubleshooting of the moiré interferometer is underway. Earlier in the year, we addressed difficulties with erroneous changes in strain with Z-position of the microscope relative to the sample as well as noise during static imaging. This quarter, we observed large changes in the perceived strain behavior depending on the tip/tilt of the sample. An example of this is shown in Figure II.1.B.86 for a control silicon wafer sample that was well-aligned vs. the same sample that had been purposefully tilted by 0.036°. This was further demonstrated when performing calibration experiments to calculate the coefficient of thermal expansion of silicon. Although controlling the tilt of ex situ control wafers is relatively straightforward, high sensitivity of the tilt of the sample is worrisome for in situ foil electrodes where the tip/tilt of the electrode is much more difficult to control while the cell is operating.

Gaussian beam simulations support the sensitivity of the measurement to changes in tilt of the sample observed experimentally. A differential measurement is being considered to try to address changes in tip/tilt as well as further improve changes due to Z-position.

Also in FY 2020, LiPAA solutions varying in lithium content and polymer molecular weight were used to create thin (less than 0.13 mm thick) films by spreading the polymer solution onto a glass plate, drying, and peeling the film off. EIS measurements were attempted between blocking copper electrodes in coin cells. However, most films shattered upon sealing the coin cell, preventing the collection of reliable data.

6. Effects of silicon nanoparticle size and surface chemistry on SEI

Our work during FY 2020 shows that the nature of the SEI is highly dependent on the initial Si NP surface chemistry. This is reflected in electrochemical cycling data, as well as postmortem characterization using techniques such as ATR-FTIR. To probe the impact of the initial surface chemical environment on the electrochemical cycling properties of Si NP-based electrodes, we have explored several different surface coating chemistries. These pre-coated Si NPs not only provide control over engineering the SEI components, but also act as a probe of the impact on SEI formation of a particular organic or inorganic molecule. Moreover, we also investigate the role of surface area and surface curvature on the SEI formation by varying the size of the Si NPs.

The baseline electrode chemistry from PECVD-synthesized Si NPs has been detailed in previous reports and we summarize briefly here. We first form a covalent bond between the surface of crystalline Si and NMP, which doubles as the slurry solvent. Electrochemical cycling data from Si NP-based electrodes of two different sizes of Si NPs with this NMP surface coating in a half-cell configuration are shown in Figure II.1.B.87. From the cycling data, the smaller (d = 3.9 nm) Si NP electrodes display a superior cycling performance compared to Si NPs with an average d = 30 nm, where the capacity retention of the smaller size exceeds the larger by hundreds of cycles. This is consistent with our prior reports. To quantify the effect of the SEI-stabilizing additive, FEC, we perform side-by-side measurements of both Si NP sizes with and without the FEC. From Figure II.1.B.87, the coin cell with the FEC additive shows an improved capacity retention for both Si NP sizes. The 3.9-nm Si NP size again displays the most robust capacity retention where the value of the 500th cycle is still 80% of that of the first, where the larger particle size displays a retention of only ~20%. The difference between the FEC-stabilized Si and non-FEC-stabilized Si points to the important conclusion that the SEI in these two electrodes is likely composed of different species.

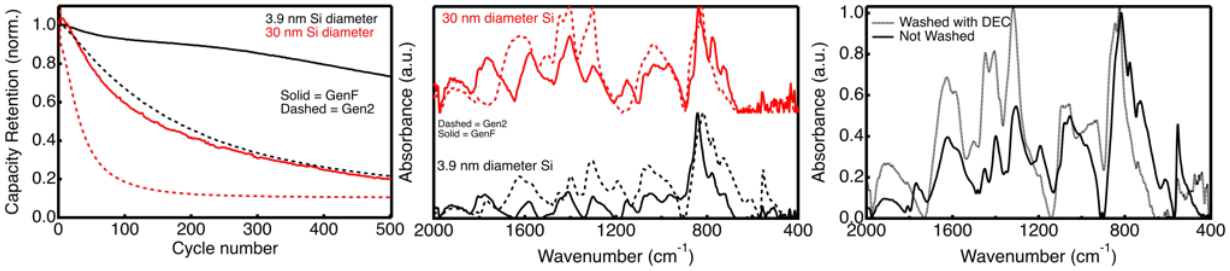

Figure II.1.B.87: (Left) Capacity retention of half-cell coin cells using 30-nm (red) and 3.9-nm (black) Si NP-based electrodes in Gen2 (dashed) and GenF (solid) electrolyte. (Middle) ATR-FTIR data collected on the same washed electrodes as the left panel after 500 cycles. The colors correspond to the same NP size. (Right) ATR-FTIR of the 3.9-nm Si NP electrode after 500 cycles in GenF electrolyte before (solid black) and after (dashed grey) rinsing in dimethylcarbonate.

To inspect how the size and presence of FEC affect the contents of the SEI, we performed ATR-FTIR spectroscopy on the washed composite electrodes, shown in the middle panel of Figure II.1.B.87after completion of their 500 cycles. The spectra of the two different-sized Si NPs are nearly identical for each electrolyte (Gen2 or GenF) used for electrochemical cycling. Moreover, despite the increase in the relative surface area with smaller d = 3.9 nm particles (greater than tenfold compared to d = 30 nm), no new SEI components are apparent in this sample. Though this result is not too surprising considering that both Si NP

sizes have identical initial surface chemistries (NMP molecular coating), the fact that their capacity retentions are so different indicates that the effect of NP size on capacity retention is a dominant effect. Therefore, we attribute the capacity retention differences between these two Si NP sizes to mechanical (swelling/deswelling) properties during lithiation/delithiation and *not* to SEI-related effects. Comparing the two SEI components of electrodes measured in Gen2 vs. GenF, signatures of all of the same components are present, but in different proportions. For example, the electrodes cycled in Gen2 display stronger absorptions at ~1,630 cm^{-1} and ~1,420 cm^{-1} (assigned to lithium alkylcarbonates) compared to the same electrodes cycled in GenF. This observation suggests that the components making up the Gen2 SEI are more organic in nature, and those in GenF are more inorganic in nature. We hypothesize that the organic-rich SEI from Gen2-based electrolyte may be less stable compared with that of the insoluble, inorganic-rich SEI that forms in GenF electrolyte. These conclusions suggest that an organic-rich SEI may be partially responsible for the reduced capacity retention in Gen2-based electrodes.

To confirm the presence of insoluble components largely making up the GenF SEI, we measured ATR-FTIR of the same cycled silicon electrodes before and after rinsing with DMC. The data from this experiment are shown in the right panel in Figure II.1.B.87. From these spectra, the contents of the SEI do not change to any significant degree after being rinsed in DMC, where the same spectroscopic signatures for each component are present and approximately at the same relative intensities. The most striking difference in these data is that the absorption feature at ~800 cm^{-1} decreases following washing. As this absorption is due to the P–F stretch and is likely residual PF_6^- salts, it is not surprising that the feature is diminished upon rising with a polar solvent (PF_6^- salts are expected be soluble). Overall, however, the SEI of GenF cycled 3.9-nm Si NP electrodes appears to remain largely intact after DMC rinsing, consistent with our previous conclusion that it is composed primarily of insoluble, inorganic components.

We next moved beyond our "baseline" NMP-coated Si NP to understand how varying the chemistry of the surface coating on the Si NPs affects the nature and amount of the SEI formed during cycling. We begin by grafting various organic molecules to the surface of d = 30 nm Si NPs. The surface molecules are chosen to test how the coating's ionic and electronic conductivity affects the formation of the SEI in operando. We react 1-dodecene with the as-grown, SiH_x-terminated Si NPs prior to electrode fabrication, which produces an alkyl (dodecyl) coated Si electrode (Si@C_{12}). This alkyl surface coating is both ionically and electronically insulating. Binding polyethyleneoxide (PEO_n) oligomers via similar reaction chemistry to the Si NP surface produces Si@PEO_n electrodes with surface coatings that are ionically conducting but electronically insulating. Figure II.1.B.41 a shows cycling data that compares the baseline Si@NMP electrode to Si@C_{12} and Si@PEO_n electrodes. The Si@C_{12} electrode rapidly (within 5–10 cycles, Figure II.1.B.88a) stabilizes at ~0 mAh/g of reversible capacity and ~100% coulombic efficiency, indicating that the ionically and electronically insulating nature of the alkyl surface coating completely arrests both the reversible lithiation/delithiation reactions as well as the irreversible SEI-forming reactions. In contrast, the Si@PEO_3 electrode shows higher capacity retention and coulombic efficiency than the baseline Si@NMP electrode. This result is consistent with the observation that oligoethers are known to conduct Li ions and, as such, have been proposed to be beneficial components of artificial and in operando formed SEI [52-55]. The ionically conducting and electrically insulating properties of coatings formed by the oligoethers promote facile lithiation/delithiation of the underlying Si while minimizing SEI formation by suppressing electrochemical side reactions between lithiated Si and the electrolyte. However, the electronic insulation of oligoether-derived coatings can also be detrimental to an electrode's performance. Figure II.1.B.88b shows the relative delithiation capacities of Si@PEO_n electrodes with varying lengths of oligoethers. The relative capacities decline to smaller steady-state values with increasing oligomer length. This electrochemical behavior suggests that sufficiently thick oligoether coatings electronically insulate the Si and begin to isolate a portion of the active material from the electron percolation network.

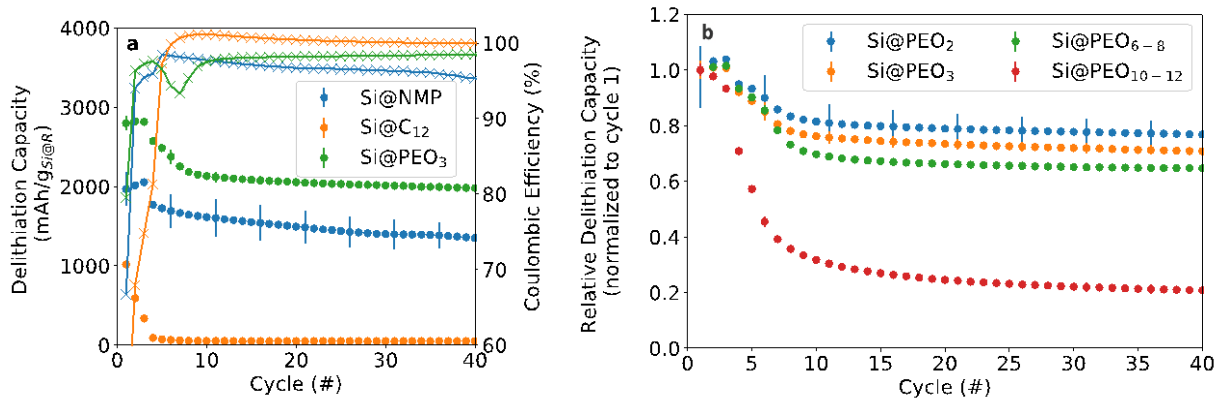

Figure II.1.B.88: (a) Delithiation capacities and coulombic efficiencies of the Si@NMP baseline, Si@C_{12}, and Si@PEO_3 electrodes. (b) Relative delithiation capacities of Si@PEO_n electrodes functionalized with different PEO_n oligomer lengths (n = 2, 3, 6–8, and 10–12).

We also performed surface coating of the Si NPs with polyaromatic molecules that can be both ionically and electronically conducting. Specifically, 4-phenyl-phenol was tethered to Si NPs that were then fabricated into Si@PP electrodes. Electrodes made with Si@PP NPs maintain reversible electrochemistry for many hundreds of cycles, as is shown by the Si@PP electrode cycled in the half-cell (Figure II.1.B.42, left panel). However, despite enabling a stable reversible capacity, the polyaromatic surface coating does not passivate against side reactions with the electrolyte and allows for continuous SEI formation. This is shown by the accumulated irreversible capacity (dotted line) in the left panel of Figure II.1.B.89, which increases continually over the entire cycle lifetime experiment. The consequences of continuous SEI formation are shown in the right panel of Figure II.1.B.89, where the Si@PP electrode is cycled vs. a $LiFePO_4$ cathode (LFP) that supplies a limited Li inventory. The immediate and continual decline of the charge/discharge capacity is a result of the SEI consuming the useable Li inventory of the full-cell, despite the benefits of the SEI formed on the polyaromatic functionalized surface of the Si NPs in half-cell configuration. This result highlights the importance of the in operando formed SEI's ability to passivate the Si active material against further SEI formation, a property that can be achieved by targeting parameters that result in measured coulombic efficiencies reaching values >>99%, especially early in an electrode's cycle lifetime.

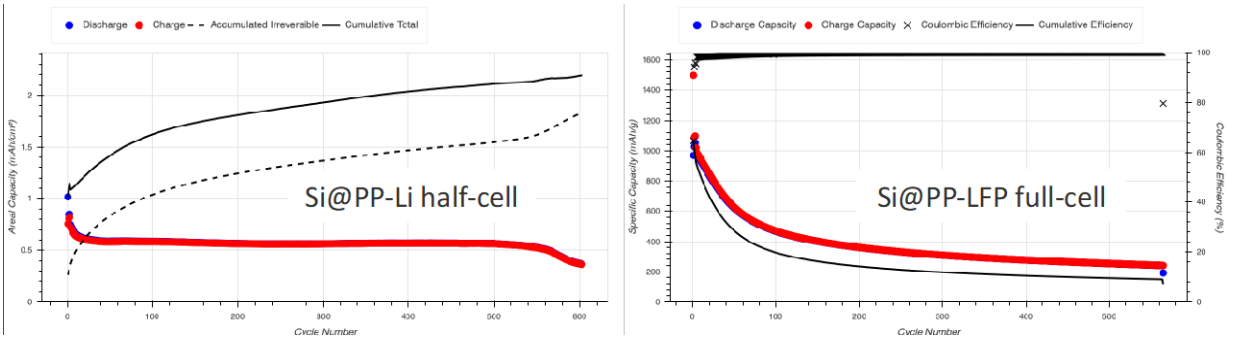

Figure II.1.B.89. Cycling data of Si@PP electrodes fabricated from Si NPs functionalized with 4-phenyl-phenol, and cycle in a (left) half-cell configuration vs. a Li metal foil and a (right) full-cell configuration vs. an LFP cathode.

Additionally, we have explored modifying the Si NP active material as a strategy for improving the performance of Si-based anodes. Related work in the SEISta and Si Deep Dive programs has shown that surface-engineered Si NPs can aid in rapidly forming a relatively stable SEI layer on the Si surface [56]. We have also pursued Si with surface engineering (Si-SE), and find this approach is viable for rapid stabilization of the coulombic efficiency. The first three formation cycles of a Si-SE NP composite anode are shown in Figure II.1.B.90. Compared with all other surface chemistries in this report, the first cycle shows a much sharper onset as the lithiation potential of crystalline Si is reached (~0.1 V vs. Li/Li^+, Figure II.1.B.43, left). The flat nature of the dQ/dV plots at potentials above lithiation is indicative of less charge consumed in

parasitic side reactions in the first formation cycle, which is direct evidence that Si-SE electrodes require a thinner SEI to passivate (equivalently, an SEI that consumes less Li). This facile passivation provided by Si-SE is reflected in the high early-cycle CEs observed not only in the first cycle, but also subsequent early cycles (Figure II.1.B.43, right). In sum, these anodes made with Si-SE NPs demonstrate first cycle CEs of over 70% and reach near-peak CE of 99.5% by the fifth cycle, an impressive result that points to surface engineering as a viable pathway to stabilize Si-based anodes.

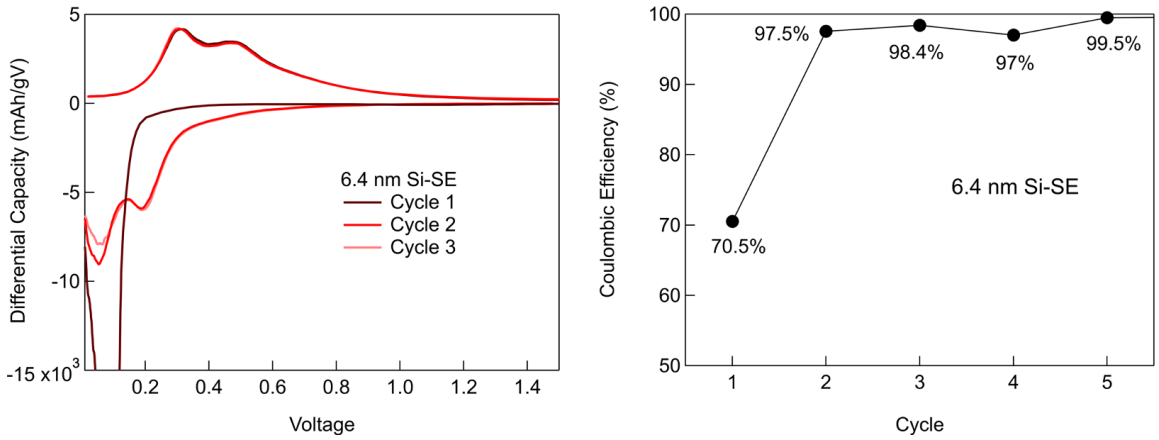

Figure II.1.B.90. Left: dQ/dV data of the first three cycles of an Si-SE composite anode in a half-cell configuration. Right: Coulombic efficiency of the first 5 cycles for the Si-SE composite anode.

Finally, we used ATR-FTIR spectroscopy to probe the nature and amount of formed/soluble SEI species of Si-SE NP composite anodes after 100 cycles in a half-cell configuration and present these data in Figure II.1.B.91. When compared with Si@NMP composite anodes (Figure II.1.B.87, right), the nature of the SEI components in the Si-SE NP-based electrode are clearly distinct. Several peaks between 1,500 and 1,000 cm^{-1} resulting from SEI formation on Si@NMP Si NP-based anodes are absent in Si-SE anodes. This result concurs with the electrochemical data presented in Figure II.1.B.90, which show that Li-consuming SEI formation reactions in Si-SE electrodes are vastly reduced relative to those in Si@NMP baseline electrodes.

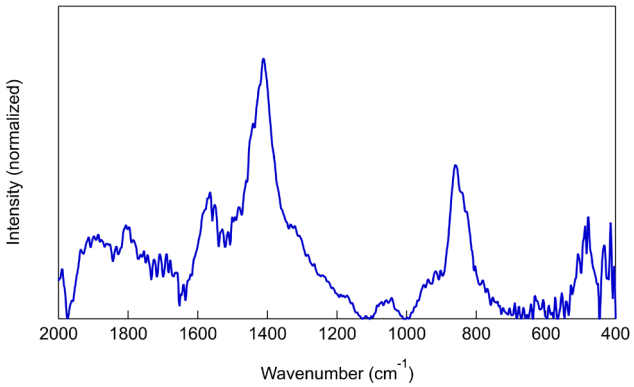

Figure II.1.B.91. ATR-FTIR data collected on an Si-SE composite anode washed with DMC after 100 cycles.

Conclusions

As the aforementioned data demonstrate, the SEI on silicon anodes is highly dynamic and changes with electrolytes and surface chemistry. These data also point to avenues to improve stability through Si NP size reduction, surface modification, and selective electrolyte chemistry. These avenues will be pursued in future studies.

References

1 Profatilova, I. A.; Stock, C.; Schmitz, A.; Passerini, S.; Winter, M., Enhanced thermal stability of a lithiated nano-silicon electrode by fluoroethylene carbonate and vinylene carbonate. J. Power Sources (2013) 222, 140–149.

2 Wang, Y.; Dahn, J., Comparison of the Reaction of LixSi or Li0.81C6 with 1 M LiPF6 EC:DEC Electrolyte at High Temperature. Electrochem. Solid-State Lett. (2006) 9, A340–A343.

3 Wang, J.; Huang, W.; Pei, A.; Li, Y.; Shi, F.; Yu, X.; Cui, Y., Improving cyclability of Li metal batteries at elevated temperatures and its origin revealed by cryo-electron microscopy. Nat. Energy (2019) 4, 664–670.

4 Stetson, C.; Yin, Y.; Jiang, C.-S.; DeCaluwe, S. C.; Al-Jassim, M.; Neale, N. R.; Ban, C.; Burrell, A., Temperature-Dependent Solubility of Solid Electrolyte Interphase on Silicon Electrodes. ACS Energy Lett.

5 An, K. S.; Park, R. J.; Kim, J. S.; Park, C. Y.; Lee, S. B.; Abukawa, T.; Kono, S.; Kinoshita, T.; Kakizaki, A.; Ishii, T. Initial interface formation study of the Mg/Si(111) system. J. Appl. Phys. 1995, 78, 1151.

6 Moriga, T.; Watanabe, K.; Tsuji, D.; Massaki, S.; Nakabayashi, I. Reaction Mechanism of Metal Silicide Mg2Si for Li Insertion. J. Solid State Chem. 2000, 153, 386.

7 Schmuelling, G.; Winter, M.; Placke, T. Investigating the Mg-Si Binary System via Combinatorial Sputter Deposition As High Energy Density Anodes for Lithium-Ion Batteries. ACS Appl. Mater. Interfaces 2015, 7, 20124.

8 Volodin, V.; Koshelev, D. Quantitative analysis of hydrogen in amorphous silicon using Raman scattering spectroscopy. J. Raman Spectrosc. 2013, 44, 1760.

9 Fujiwara, H.; Kondo, M.; Matsuda, A. Depth profiling of silicon–hydrogen bonding modes in amorphous and microcrystalline Si: H thin films by real-time infrared spectroscopy and spectroscopic ellipsometry. J. Appl. Phys. 2002, 91, 4181.

10 Nieroda, P.; Mars, K.; Nieroda, J.; Leszczyński, J.; Król, M.; Drożdż, E.; Jeleń, P.; Sitarz, M.; Koleżyński, A. New high temperature amorphous protective coatings for Mg2Si thermoelectric material. Ceram. Int. 2019, 45, 10230.

11 Brown, Z. L.; Jurng, S.; Nguyen, C. C.; Lucht, B. L. Effect of fluoroethylene carbonate electrolytes on the nanostructure of the solid electrolyte interphase and performance of lithium metal anodes. ACS Appl. Energy Mater. 2018, 1, 3057.

12 Yoon, T.; Chapman, N.; Seo, D. M.; Lucht, B. L. Lithium salt effects on silicon electrode performance and solid electrolyte interphase (SEI) structure, role of solution structure on SEI formation. J. Electrochem. Soc. 2017, 164, A2082.

13 Etacheri, V.; Haik, O.; Goffer, Y.; Roberts, G. A.; Stefan, I. C.; Fasching, R.; Aurbach, D. Effect of fluoroethylene carbonate (FEC) on the performance and surface chemistry of Si-nanowire Li-ion battery anodes. Langmuir 2012, 28, 965.

14 United States Advanced Battery Consortium Battery Test Manual For Electric Vehicles; 2015.

15 Long, B. R.; Rinaldo, S. G.; Gallagher, K. G.; Dees, D. W.; Trask, S. E.; Polzin, B. J.; Jansen, A. N.; Abraham, D. P.; Bloom, I.; Bareño, J.; Croy, J. R. Enabling High-Energy, High-Voltage Lithium-Ion

Cells: Standardization of Coin-Cell Assembly, Electrochemical Testing, and Evaluation of Full Cells. 35th Annu. Int. Batter. Semin. Exhib. 2018 2018, 1 (14), 112–122. https://doi.org/10.1149/2.0691614jes.

16 Single, F.; Latz, A.; Horstmann, B. Identifying the Mechanism of Continued Growth of the Solid–Electrolyte Interphase. ChemSusChem 2018, 11 (12), 1950–1955. https://doi.org/10.1002/cssc.201800077.

17 Attia, P. M.; Chueh, W. C.; Harris, S. J. Revisiting the t 0.5 Dependence of SEI Growth . J. Electrochem. Soc. 2020, 167 (9), 090535. https://doi.org/10.1149/1945-7111/ab8ce4.

18 Khan, M. M.; Nemati, A.; Rahman, Z. U.; Shah, U. H.; Asgar, H.; Haider W. Recent Advances in Bulk Metallic Glasses and Their Applications: A Review. Critical Reviews in Solid State and Materials Sciences 43, 233–268 (2018).

19 Nair, B.; Priyadarshini, B. G. Process, Structure, Property and Applications of Metallic Glasses. AIMS Materials Science 3, 1022–1053 (2016).

20 Fleischauer, M. D.; Dahn, J. R. Combinatorial Investigation of the Si-Al-Mn System for Li-Ion Battery Applications. Journal of The Electrochemical Society 151, A1216–A1221 (2004).

21 Obrovac, M. N.; Christensen, L.; Le, D. B.; Dahn, J. R. Alloy design for lithium-ion battery anodes. J. Electrochem. Soc. 154, 849–855 (2007).

22 Stetson, C.; Yoon, T.; Coyle, J.; Nemeth, W.; Young, M.; Norman, A.; Pylypenko, S.; Ban, C.; Jiang, C.-S.; Al-Jassim, M.; Burrell, A., Three-dimensional electronic resistivity mapping of solid electrolyte interphase on Si anode materials. Nano Energy 2019, 55, 477-485.

23 Charles, R. J., Some Structural and Electrical Properties of Lithium Silicate Glasses. Journal of the American Ceramic Society 1963, 46, 235-243.

24 He, L.-N.; Xua, J., Properties of amorphous SiO2 films prepared by reactive RF magnetron sputtering method. Vacuum 2003, 68, 197-202.

25 Schnabel, M.; Harvey, S. P.; Arca, E.; Stetson, C.; Teeter, G.; Ban, C.; Stradins, P., Surface SiO2 Thickness Controls Uniform-to-Localized Transition in Lithiation of Silicon Anodes for Lithium-Ion Batteries. ACS Applied Materials & Interfaces 2020, 12 (24), 27017-27028.

26 Schnabel, M.; Arca, E.; Ha, Y.; Stetson, C.; Teeter, G.; Han, S.-D.; Stradins, P., Enhanced Interfacial Stability of Si Anodes for Li-Ion Batteries via Surface SiO2 Coating. ACS Appl. Energy Mater. 2020, 3 (9), 8842-8849.

27 Nguyen, C. C.; Yoon, T.; Seo, D. M.; Guduru, P.; Lucht, B. L., Systematic Investigation of Binders for Silicon Anodes: Interactions of Binder with Silicon Particles and Electrolytes and Effects of Binders on Solid Electrolyte Interphase Formation. ACS Appl. Mater. Interfaces 2016, 8 (19), 12211-12220.

28 Chen, H.; Ling, M.; Hencz, L.; Ling, H. Y.; Li, G.; Lin, Z.; Liu, G.; Zhang, S., Exploring Chemical, Mechanical, and Electrical Functionalities of Binders for Advanced Energy-Storage Devices. Chemical Reviews 2018, 118 (18), 8936-8982.

29 Kwon, T.-w.; Choi, J. W.; Coskun, A., The Emerging Era of Supramolecular Polymeric Binders in Silicon Anodes. Chemical Society Reviews 2018, 47 (6), 2145-2164.

30 Li, J.; Lewis, R. B.; Dahn, J. R., Sodium Carboxymethyl Cellulose. Electrochemical and Solid-State Letters 2007, 10 (2), A17.

31 Farooq, U.; Choi, J.-H.; Atif Pervez, S.; Yaqub, A.; Kim, D.-H.; Lee, Y.-J.; Saleem, M.; Doh, C.-H., Effect of Binder and Composition Ratio on Electrochemical Performance of Silicon/Graphite Composite Battery Electrode. Materials Letters 2014, 136, 254-257.

32 Kovalenko, I.; Zdyrko, B.; Magasinski, A.; Hertzberg, B.; Milicev, Z.; Burtovyy, R.; Luzinov, I.; Yushin, G., A Major Constituent of Brown Algae for Use in High-Capacity Li-Ion Batteries. Science 2011, 334 (6052), 75.

33 Park, H.-K.; Kong, B.-S.; Oh, E.-S., Effect of High Adhesive Polyvinyl Alcohol Binder on the Anodes of Lithium Ion Batteries. Electrochemistry Communications 2011, 13 (10), 1051-1053.

34 Jeong, Y. K.; Kwon, T.-w.; Lee, I.; Kim, T.-S.; Coskun, A.; Choi, J. W., Millipede-Inspired Structural Design Principle for High Performance Polysaccharide Binders in Silicon Anodes. Energy & Environmental Science 2015, 8 (4), 1224-1230.

35 Magasinski, A.; Zdyrko, B.; Kovalenko, I.; Hertzberg, B.; Burtovyy, R.; Huebner, C. F.; Fuller, T. F.; Luzinov, I.; Yushin, G., Toward Efficient Binders for Li-Ion Battery Si-Based Anodes: Polyacrylic Acid. ACS Applied Materials & Interfaces 2010, 2 (11), 3004-3010.

36 Hu, B.; Jiang, S.; Shkrob, I. A.; Zhang, S.; Zhang, J.; Zhang, Z.; Zhang, L., Poly(4-vinylbenzoic acid): A Re-Engineered Binder for Improved Performance from Water-Free Slurry Processing for Silicon Graphite Composite Electrodes. ACS Applied Energy Materials 2019, 2 (9), 6348-6354.

37 Bridel, J. S.; Azaïs, T.; Morcrette, M.; Tarascon, J. M.; Larcher, D., In Situ Observation and Long-Term Reactivity of Si/C/CMC Composites Electrodes for Li-Ion Batteries. Journal of The Electrochemical Society 2011, 158 (6), A750.

38 Jiang, S.; Hu, B.; Shi, Z.; Chen, W.; Zhang, Z.; Zhang, L., Re-Engineering Poly(Acrylic Acid) Binder toward Optimized Electrochemical Performance for Silicon Lithium-Ion Batteries: Branching Architecture Leads to Balanced Properties of Polymeric Binders. Advanced Functional Materials 2020, 30 (10), 1908558.

39 Hu, B.; Jiang, S.; Shkrob, I. A.; Zhang, J.; Trask, S. E.; Polzin, B. J.; Jansen, A.; Chen, W.; Liao, C.; Zhang, Z.; Zhang, L., Understanding of pre-lithiation of poly(acrylic acid) binder: Striking the balances between the cycling performance and slurry stability for silicon-graphite composite electrodes in Li-ion batteries. Journal of Power Sources 2019, 416, 125-131.

40 Hu, B.; Shkrob, I. A.; Zhang, S.; Zhang, L.; Zhang, J.; Li, Y.; Liao, C.; Zhang, Z.; Lu, W.; Zhang, L., The existence of optimal molecular weight for poly(acrylic acid) binders in silicon/graphite composite anode for lithium-ion batteries. Journal of Power Sources 2018, 378, 671-676.

41 Nanda, J.; Yang, G.; Hou, T.; Voylov, D. N.; Li, X.; Ruther, R. E.; Naguib, M.; Persson, K.; Veith, G. M.; Sokolov, A. P., Unraveling the Nanoscale Heterogeneity of Solid Electrolyte Interphase Using Tip-Enhanced Raman Spectroscopy. Joule 2019.

42 Yang, J.; Liu, H.; Martens, W. N.; Frost, R. L., Synthesis and characterization of cobalt hydroxide, cobalt oxyhydroxide, and cobalt oxide nanodiscs. The Journal of Physical Chemistry C 2010, 114 (1), 111-119.

43 Aurbach, D.; Markovsky, B.; Shechter, A.; Ein-Eli, Y.; Cohen, H., A comparative study of synthetic graphite and Li electrodes in electrolyte solutions based on ethylene carbonate-dimethyl carbonate mixtures. Journal of the Electrochemical Society 1996, 143 (12), 3809.

44 Yan, J.; Xia, B.-J.; Su, Y.-C.; Zhou, X.-Z.; Zhang, J.; Zhang, X.-G., Phenomenologically modeling the formation and evolution of the solid electrolyte interface on the graphite electrode for lithium-ion batteries. Electrochimica Acta 2008, 53 (24), 7069-7078.

45 Schulz, N.; Hausbrand, R.; Dimesso, L.; Jaegermann, W., XPS-surface analysis of SEI layers on Li-Ion cathodes: part I. Investigation of initial surface chemistry. Journal of The Electrochemical Society 2018, 165 (5), A819-A832.

46 Hou, T.; Yang, G.; Rajput, N. N.; Self, J.; Park, S.-W.; Nanda, J.; Persson, K. A., The influence of FEC on the solvation structure and reduction reaction of LiPF6/EC electrolytes and its implication for solid electrolyte interphase formation. Nano Energy 2019, 64, 103881.

47 Hantsche, H., High resolution XPS of organic polymers, the scienta ESCA300 database. By G. Beamson and D. Briggs, Wiley, Chichester 1992, 295 pp., hardcover,£ 65.00, ISBN 0-471-93592-1. Advanced Materials 1993, 5 (10), 778-778.

48 Wu, Q.; Shi, B.; Bareño, J.; Liu, Y.; Maroni, V. A.; Zhai, D.; Dees, D. W.; Lu, W., Investigations of Si thin films as anode of lithium-ion batteries. ACS applied materials & interfaces 2018, 10 (4), 3487-3494.

49 Yoon, T.; Chapman, N.; Seo, D. M.; Lucht, B. L., Lithium salt effects on silicon electrode performance and solid electrolyte interphase (SEI) structure, role of solution structure on SEI formation. Journal of The Electrochemical Society 2017, 164 (9), A2082-A2088.

50 Wood, K. N.; Teeter, G., XPS on Li-Battery-Related Compounds: Analysis of Inorganic SEI Phases and a Methodology for Charge Correction. ACS Appl. Energy Mater. 2018, 1 (9), 4493-4504.

51 Hasa, I.; Haregewoin, A. M.; Zhang, L.; Tsai, W.-Y.; Guo, J.; Veith, G. M.; Ross, P. N.; Kostecki, R., Electrochemical Reactivity and Passivation of Silicon Thin-Film Electrodes in Organic Carbonate Electrolytes. ACS Applied Materials & Interfaces 2020, 12 (36), 40879-40890.

52 Wu, M.; Xiao, X.; Vukmirovic, N.; Xun, S.; Das, P. K.; Song, X.; Olalde-Velasco, P.; Wang, D.; Weber, A. Z.; Wang, L.-W.; Battaglia, V. S.; Yang, W.; Liu, G., Toward an Ideal Polymer Binder Design for High-Capacity Battery Anodes. Journal of the American Chemical Society 2013, 135 (32), 12048-12056.

53 Wang, W.; Yi, E.; Fici, A. J.; Laine, R. M.; Kieffer, J., Lithium Ion Conducting Poly(ethylene oxide)-Based Solid Electrolytes Containing Active or Passive Ceramic Nanoparticles. The Journal of Physical Chemistry C 2017, 121 (5), 2563-2573.

54 Jiang, S.; Hu, B.; Sahore, R.; Liu, H.; Pach, G. F.; Carroll, G. M.; Zhang, L.; Zhao, B.; Neale, N. R.; Zhang, Z., Tailoring the Surface of Silicon Nanoparticles for Enhanced Chemical and Electrochemical Stability for Li-Ion Batteries. ACS Applied Energy Materials 2019, 2 (9), 6176-6183.

55 Jin, Y.; Kneusels, N.-J. H.; Marbella, L. E.; Castillo-Martínez, E.; Magusin, P. C. M. M.; Weatherup, R. S.; Jónsson, E.; Liu, T.; Paul, S.; Grey, C. P., Understanding Fluoroethylene Carbonate and Vinylene Carbonate Based Electrolytes for Si Anodes in Lithium Ion Batteries with NMR Spectroscopy. Journal of the American Chemical Society 2018, 140 (31), 9854-9867.

56 Han, B.; Liao, C.; Dogan, F.; Trask, S. E.; Lapidus, S. H.; Vaughey, J. T.; Key, B., Using Mixed Salt Electrolytes to Stabilize Silicon Anodes for Lithium-Ion Batteries via in Situ Formation of Li–M–Si Ternaries (M = Mg, Zn, Al, Ca). ACS Appl. Mater. Interfaces 2019, 11 (33), 29780-29790.